University of Alberta

Propagation and Breaking of Nonlinear Internal Gravity Waves

by

Hayley V. Dosser

A thesis submitted to the Faculty of Graduate Studies and Research
in partial fulfillment of the requirements for the degree of

Master of Science

Department of Physics

Spring 2010
Edmonton, Alberta

Examining Committee

Bruce R. Sutherland, Physics / Earth and Atmospheric Sciences

Gordon E. Swaters, Mathematical and Statistical Sciences

Richard D. Sydora, Physics

Ian Mann, Physics

Abstract

Internal gravity waves grow in amplitude as they propagate upwards in a non-Boussinesq fluid and weakly nonlinear effects develop due to interactions with an induced horizontal mean flow. In this work, a new derivation for this wave-induced mean flow is presented and nonlinear Schrödinger equations are derived describing the weakly nonlinear evolution of these waves in an anelastic gas and non-Boussinesq liquid. The results of these equations are compared with fully nonlinear numerical simulations. It is found that interactions with the wave-induced mean flow are the dominant mechanism for wave evolution. This causes modulational stability for hydrostatic waves, resulting in propagation above the overturning level predicted by linear theory for a non-Boussinesq liquid. Due to high-order dispersion terms in the Schrödinger equation for an anelastic gas, hydrostatic waves become unstable and break at lower levels. Non-hydrostatic waves are modulationally unstable, overturning at lower levels than predicted by linear theory.

Acknowledgements

First of all, I want to thank my mom, Patricia, for instilling in me a love of science, for believing in me when I couldn't believe in myself, and for always being there. She will never know how much of an influence she has on my life, nor how much I love her for it. I also want to thank my grandmother, who thinks scientists will end the world, yet still supports me in my efforts to prove her wrong, and my sister Alexandra, for the late night talks, the hot chocolate breaks that kept us both sane, and understanding when no one else could.

I wouldn't have made it this far without my partner Ryan, who fed me (and the cat) when I was busy, comforted me when I needed it most, and was my captive audience for practice talks he couldn't understand a word of. I know he will stand by me no matter what I choose to do or where we end up.

This research would not exist without my supervisor Bruce, who has guided me with humor and patience, convinced me to continue on the path to becoming an academic, travelled all over the place with a group of 7 students, and still not lost his mind. Well, not much anyway. I also want to thank my research group, in particular my cubicle-mates Heather and Kate, who made my time as a graduate student not only bearable but wonderful.

Finally, I would like to thank my committee members for their time, interest and valuable insight. The U of A is lucky to have such professors.

This research was supported by the Natural Sciences and Engineering Research Council of Canada (NSERC) and the Canadian Foundation for Climate and Atmospheric Sciences (CFCAS).

Table of Contents

List of Tables

List of Figures

Chapter 1

Introduction

1.1 Motivation

Vertically propagating internal gravity waves exist in stably stratified fluids, in which the effective density decreases continuously with height. Examples of such fluids include a liquid such as the ocean, where salinity and temperature vary, or a gas such as the atmosphere, where the effective density is determined by the temperature and thermodynamics of the fluid. For a fluid in which the density does not change significantly over the total depth, it is typical to apply the Boussinesq approximation. In this approximation, the background density is taken to be constant in the momentum equations, with the exception of the buoyancy term (Kundu, 1990). The approximation also requires incompressibility, which has the effect of filtering sound waves from the fluid. Typically, the Boussinesq approximation is used for the ocean, because the change in background density over its total depth is small.

For the atmosphere, waves propagating upward over a significant height experience a large background density decrease, so their evolution is influenced by non-Boussinesq processes. In particular, due to momentum conservation (Eliassen and Palm, 1961), small amplitude waves launched near the ground increase in amplitude as they propagate upwards, eventually reaching such large amplitudes that linear theory no longer adequately models their evolu-

tion. Thus nonlinear effects play an important role in the evolution of internal gravity waves in the atmosphere. In order to capture correctly the effect these waves have on the circulation of the atmosphere, it will eventually become necessary to incorporate their nonlinear dynamics into general circulation models. However, because internal gravity waves are typically too small in scale to be resolved in a global numerical model, their dynamics presently must be included through parameterization schemes that rely on observations and linear theory heuristics.

Internal gravity waves can propagate in both the vertical and the horizontal direction. In the atmosphere, the vertical propagation of these waves is usually of more concern, since they transport momentum upwards, then overturn and break, resulting in the deposition of their momentum into the environment. Generation mechanisms for internal gravity waves in the atmosphere include wind flow over mountain ranges, which launches topographic internal waves, and convective storms in the troposphere, which launch waves into the stratosphere. Internal gravity waves generated by these mechanisms generally take the form of vertically propagating quasi-monochromatic wavepackets.

Due to the decrease in background density with increasing height in the atmosphere, a small-amplitude internal gravity wave will grow to large amplitude as it propagates in order to conserve momentum (Bretherton, 1966). As the waves break and deposit their momentum at the breaking level, there is an energy cascade to ever-smaller scales eventually resulting in dissipation by molecular viscosity and heat diffusion (Hamilton, 1996). The deposition of momentum by breaking internal gravity waves is often referred to as gravity wave drag, which has the effect of accelerating local winds in the direction of the horizontal phase speed of the waves relative to the background wind (Hartmann, 2007).

Inclusion of the momentum source of breaking internal gravity waves in

general circulation models induces a steady meridional wind that acts to reduce the temperature gradient between the poles. It also produces stratospheric zonal jets and a wind reversal in the mesosphere which are closer to observations (McLandress, 1998). Accounting for these effects is important in determining the spread of chemicals such as ozone and pollutants that are carried by meridional winds.

One of the current challenges of internal gravity wave parameterization is to understand the processes that lead to so-called "wave saturation", which refers to waves reaching overturning amplitudes. Many schemes use the model proposed by Lindzen (1981) in which waves passing above a breaking level, the location of which is estimated using linear theory, generate turbulence that limits their amplitude growth as they continue to propagate vertically. The location of breaking levels is in reality determined by many factors, including the nonlinear effects of wave-wave interactions and interactions between waves and the mean flow they induce. The motivation behind this research is to determine the dominant nonlinear effects that impact wavepacket dynamics and breaking height. This will be done through the development of weakly nonlinear equations whose results will be compared with the results of fully nonlinear numerical simulations.

1.2 Background

Despite the importance of nonlinear effects upon the evolution and ultimately the breaking of waves, developing a weakly nonlinear theory for moderately large amplitude waves has been challenging because internal gravity plane waves provide an exact solution to the fully nonlinear equations of fluid motion. Recently, however, a new approach that examines wavepackets was successfully employed to predict the evolution of weakly nonlinear Boussinesq waves (Sutherland, 2006b). One purpose of this research is to extend these

results to non-Boussinesq waves and, together with fully nonlinear numerical simulations, test the range of validity of linear theory and explore the impact of nonlinear effects.

Most previous studies which considered the amplitude growth of vertically propagating internal gravity waves focused on wave interactions with an existing background mean flow. It was found that transient internal waves could modify this zonal mean flow, changing the breaking height of the waves, as demonstrated by Dunkerton (1981) through quasi-linear numerical simulations. As a large amplitude wave approached a critical level (defined as the location where the horizontal phase speed of a wave is equal to the speed of the background flow), its phase lines became tilted and its vertical group velocity decreased. Thus, waves interacting nonlinearly with the mean flow near a critical level caused the position of the critical level to change over time as the location of the mean flow descended. Numerical simulations by Fritts (1978) supported this observation.

Fully nonlinear simulations by Grimshaw (1975) displayed differences in the evolution of small and large amplitude Boussinesq internal waves due to interactions with a wind shear and Doppler-shifting of the waves by the mean flow. He observed that small amplitude wavepackets grew and narrowed prior to dissipating, while large amplitude wavepackets remained broad, peaked at a lower level and decayed more slowly.

Later studies confirmed that large amplitude wavepackets behaved qualitatively differently than the predictions of linear theory (Fritts and Dunkerton, 1984) due to nonlinear interactions with the mean flow near a critical level. These interactions resulted in the phase speed, vertical wavenumber and group velocity increasing at the leading edge of a wavepacket and decreasing at the trailing edge, which caused vertical spreading. This modified the wavepacket to such a degree that it could propagate beyond its original critical level.

Even in the absence of any background shear or mean flow created by wave breaking events, there can still be interactions between the waves and the transient horizontal mean flow created by the waves themselves. Within a wavepacket that is horizontally periodic and vertically localized, the wave components interact with each other in such a way that a horizontal mean flow is induced during propagation. This "wave-induced mean flow", which is present as soon as the waves are generated, is analogous to the Stokes Drift for surface waves. The Stokes Drift is a second-order amplitude effect that causes the mean Lagrangian velocity of a fluid parcel to be non-zero (Kundu, 1990).

Using Hamiltonian fluid mechanics, a form for the wave-induced mean flow of internal waves was determined by identifying the wave-induced mean flow as the pseudomomentum per unit mass (Scinocca and Shepherd, 1992). Just as Noether's theorem predicts momentum conservation in a classical system which is invariant to horizontal translations, so pseudomomentum is a conserved quantity for waves in a fluid system which is invariant to horizontal translations (McIntyre, 1981). This connection with the pseudomomentum resulted in an explicit formula for the wave-induced mean flow, given at leading order by

$$U(z,t) \equiv -\langle \xi\zeta \rangle \,. \tag{1.1}$$

Here ξ is the vertical displacement of the fluid caused by the waves, ζ is the spanwise component of the vorticity, and the average is taken over one horizontal wavelength. This form for the wave-induced mean flow is accurate for small amplitude waves, and has previously been shown to be a good approximation for Boussinesq waves of even moderately large amplitude (Sutherland, 1996).

The wave-induced mean flow for Boussinesq waves was previously derived using energy conservation relations. Bretherton (1969) used the polarization relations to relate the mean vertical flux of horizontal momentum per unit

mass to the mean wave energy density $\langle E \rangle$ by

$$\langle uw \rangle = \left(\frac{\langle E \rangle}{\omega - k\bar{U}} \right) k c_{gz}. \tag{1.2}$$

Here u and w are the horizontal and vertical components respectively of the fluctuation velocity, c_{gz} is the vertical group velocity of the wave, k is the horizontal wavenumber, and $\bar{U}(z)$ is the prescribed horizontal background velocity. The term in parentheses in equation (1.2) is $\langle \mathcal{A} \rangle$, the mean wave-action density (Gill, 1982).

Separately, Acheson (1976) derived an equation relating the wave energy density to the wave-induced mean flow:

$$U = \frac{\langle E \rangle}{\omega - k\bar{U}} k = \mathcal{A} k. \tag{1.3}$$

The derivation of this equation takes advantage of the conservation of wave action and a heuristic comparison of terms resulting from the polarization relations. In combination, equation (1.2) and (1.3) result in a succinct implicit formula for the wave-induced mean flow $U(z,t)$:

$$\langle uw \rangle = c_{gz} U(z,t). \tag{1.4}$$

Indeed, using the polarization relations for Boussinesq waves in a stationary ambient medium, one can confirm that (1.1) and (1.4) give identical expressions for U in terms of the wave amplitude. However, equations (1.1) and (1.4) are not necessarily valid for internal gravity waves in a non-Boussinesq fluid. In part, this thesis will develop a more intuitive method to derive a formula for the wave-induced mean flow based upon momentum rather than energy or wave action conservation laws.

Although the Stokes Drift does not significantly impact the evolution of surface waves, interactions between internal waves and their wave-induced mean flow have been shown to dominate the evolution of Boussinesq internal

gravity wavepackets for amplitudes below breaking (Sutherland (2006a); Akylas and Tabaei (2005)). The nature of the interaction has been referred to as "self-acceleration" (Fritts and Dunkerton, 1984). The wave-induced mean flow acts to Doppler-shift the frequency of the waves significantly from linear theory values if the waves are of moderately large amplitude. This effect can cause the waves to overturn and break (Sutherland, 2001) if the amplitude is so large that the wave-induced mean flow is greater than the horizontal group velocity of the waves.

The physics that dictates how weak nonlinearity affects internal gravity wavepackets is given by the nonlinear Schrödinger equation. This partial differential equation describes the spatial and temporal evolution of the amplitude envelope of moderately large amplitude waves. The linear Schrödinger equation that explicitly includes the effect of translation at the group velocity has the form

$$\partial_t A + c_{gz}\partial_z A = \imath\frac{1}{2}\omega_{mm}\partial_{zz}A, \tag{1.5}$$

in which A is the amplitude of the wavepacket envelope, m is the vertical wavenumber, $c_{gz} \equiv \omega_m$ is the vertical group velocity and $\omega_{mm} = \partial^2\omega/\partial m^2$ is a constant coefficient determined from the dispersion relation $\omega \equiv \omega(m, k)$. The linear equation captures only the vertical translation of the wavepacket at the group velocity and the effects of leading-order linear dispersion upon small amplitude waves. Nonlinearity is introduced by including the effects of self-acceleration and higher order nonlinear dispersion. Using our formula for the wave-induced mean flow of non-Boussinesq waves, we derive the corresponding nonlinear Schrödinger equation describing the evolution of non-Boussinesq internal gravity wavepackets.

The coefficients of the nonlinear Schrödinger equation allow us to assess the modulational stability of the waves (Whitham (1974); Phillips (1981)). Modulational stability and instability are weakly nonlinear effects occurring for

moderately large amplitude dispersive wavepackets. The amplitude envelope of modulationally unstable waves initially grows faster than expected from linear theory, whereas the amplitude envelope of modulationally stable waves decreases faster than predicted by linear dispersion. Thus in the latter case modulationally stable waves are anticipated to break at levels higher than those predicted by linear theory. Conversely, modulationally unstable waves are expected to break at lower levels than predicted by linear theory. It is possible for a modulationally unstable wavepacket to avoid breaking through the Fermi-Pasta-Ulam recurrence phenomenon (Fermi et al., 1974), in which a periodic transfer of energy among the wavenumber components is followed by a return to the initial state. This phenomenon has been captured by numerical solutions of the nonlinear Schrödinger equation for a deep water wave train experiencing the Benjamin-Feir instability (Lake et al. (1977); Benjamin and Feir (1967)). Through the inclusion of third order terms in our weakly nonlinear Schrödinger equation, we will show that higher order linear and nonlinear dispersion breaks the symmetry associated with Fermi-Pasta-Ulam recurrence.

Though not captured by the nonlinear Schrödinger equation, internal waves may also transfer energy to waves of shorter wavelength and higher wavenumber through parametric subharmonic instability (Klostermeyer (1991); Lombard and Riley (1996)). This instability results from an interaction between three waves, in which energy is transferred from the primary wave to two other secondary waves of fractional frequency (Gill, 1982). It can lead to wave steepening and overturning as energy cascades to smaller scales (Bouruet-Aubertot et al., 1995). However, because the time scale for this instability is much longer than that for weakly nonlinear modulations of a wavepacket (Sutherland, 2006a) it is anticipated that modulational instability will emerge as the primary mechanism determining the evolution of a wavepacket moving upward through a non-Boussinesq fluid. We confirm this hypothesis by comparing the

solutions of the weakly nonlinear equation with the results of fully nonlinear numerical simulations.

In §2 we derive the wave equations appropriate for a non-Boussinesq liquid and a non-Boussinesq gas, the latter of which is more commonly referred to as an anelastic gas. Considering a liquid as well as a gas is useful for the following reasons: modelling a liquid avoids the need to incorporate the thermodynamics of a gas while still retaining many of the features of non-Boussinesq wave evolution; the extension of the weakly nonlinear theory developed for Boussinesq fluids to non-Boussinesq liquids is more direct; and non-Boussinesq internal waves in a liquid can be examined in a laboratory setting using salt-stratified solutions, thus providing a valuable comparison between experiments and theory (Clark and Sutherland, 2009). In §3, the fully nonlinear numerical models for the non-Boussinesq liquid and the anelastic gas equations are described. This is followed in §4 by a comparison of the weakly and fully nonlinear dynamics of internal gravity waves in a non-Boussinesq liquid and an anelastic gas. Finally, in §5 we discuss the impact of these nonlinear dynamics on the breaking heights of the waves and we consider the discrepancies between the breaking levels given by the fully nonlinear simulations and the predictions of linear theory.[1]

[1]A version of chapters 2, 3, 4, and 5 regarding internal waves in a non-Boussinesq liquid has been submitted for publication, and is currently under review. Dosser, H. V. and Sutherland, B. R., "Weakly Nonlinear Non-Boussinesq Internal Gravity Wavepackets", 2009. Physica D: Nonlinear Phenomena. The work regarding waves in an anelastic gas is in preparation for submission to the Journal of the Atmospheric Sciences. In writing this thesis, the discussion of both papers has been combined to avoid repetition and to provide clarity in the comparison of results.

Chapter 2

Theory

2.1 Governing equations

This work considers the dynamics of internal gravity waves in both a non-Boussinesq liquid and an anelastic gas. In order to arrive at the governing equations for these waves, we begin with the fully nonlinear Euler equations for conservation of momentum:

$$\rho_T \frac{D\vec{u}_T}{Dt} = -\nabla P_T + \vec{g}\rho_T. \tag{2.1}$$

Here ρ_T is the total density and P_T is the total pressure. The subscript $_T$ denotes a 'total' field and does not indicate a partial derivative. The total velocity of a fluid parcel is given in terms of the total horizontal and vertical velocities respectively by $\vec{u}_T = (u_T, w_T)$. Restricting ourselves to two-dimensional Cartesian co-ordinates, the material derivative is $D/Dt = \partial_t + u_T\partial_x + w_T\partial_z$. Equation (2.1) states that the acceleration of a fluid parcel depends upon the pressure gradient and buoyancy forces that act on it. We have neglected Coriolis forces because our study focuses on waves with periods of a few hours or less.

In a fluid whose total density varies little over the domain height the equations are further simplified by making the Boussinesq approximation, in which the density is assumed to be constant except where it appears in the buoyancy term. However, for internal waves propagating in a non-Boussinesq fluid such

as the atmosphere, the density changes substantially with height. Thus on the left-hand side of (2.1) we assume that $\rho_T \approx \bar{\rho}(z)$; the influence of the density perturbations due to the waves upon the fluid's momentum is negligibly small compared to that of the background density. This leads to the fully nonlinear non-Boussinesq momentum equations for inviscid internal gravity waves:

$$\bar{\rho}\frac{D\vec{u_T}}{Dt} = -\nabla P - g\rho\hat{z}. \tag{2.2}$$

Here ρ_T and P_T have been written respectively as the sum of the background density and pressure, $\bar{\rho}(z)$ and $\bar{P}(z)$, and the fluctuation density and pressure, $\rho(\vec{x}, t)$ and $P(\vec{x}, t)$. We have invoked background hydrostatic balance, $d\bar{P}/dz = -\bar{\rho}g$, in which the gravitational term in the momentum conservation equation (2.2) is balanced by the background pressure gradient term (Vallis, 2006), so that only the fluctuation density and pressure appear on the right-hand side of (2.2).

The full evolution equations of the waves also include the laws for conservation of internal energy and mass. These differ for waves in a liquid and in a gas. For an incompressible liquid, neglecting diffusion of heat and salinity, we have

$$\nabla \cdot \vec{u_T} = 0, \tag{2.3}$$

$$\frac{D\rho_T}{Dt} = 0. \tag{2.4}$$

These, together with (2.2), are the wave equations for a non-Boussinesq liquid. They differ from the Boussinesq equations only in the appearance of $\bar{\rho}$, rather than a characteristic density ρ_0, multiplying the acceleration terms in (2.2).

Equation (2.3) has the effect of filtering sound waves in a liquid. It results from the need for self-consistency between the internal energy equation and the incompressibility condition for a liquid, both of which have the form of equation (2.4). It follows from the continuity equation in its general form

$$\frac{D\rho_T}{Dt} = \rho_T \nabla \cdot \vec{u_T} \tag{2.5}$$

that (2.3) is satisfied.

For an anelastic gas, internal energy conservation and, consequently, buoyancy forces are more conveniently cast in terms of potential temperature as opposed to density. The fully nonlinear equations for inviscid, two-dimensional internal gravity waves in an ideal anelastic gas are given by

$$\frac{D\vec{u_T}}{Dt} = -\nabla\frac{P}{\bar{\rho}} + \frac{g}{\bar{\theta}}\theta\hat{z}, \tag{2.6}$$

$$\nabla \cdot (\bar{\rho}\vec{u_T}) = 0, \tag{2.7}$$

$$\frac{D\theta_T}{Dt} = 0. \tag{2.8}$$

Here the total potential temperature is given by

$$\theta_T = T_T(P_0/P_T)^{\kappa}, \tag{2.9}$$

where T_T is the total temperature field, P_0 is a reference pressure, and $\kappa \simeq 2/7$. The potential temperature is written on the right-hand side of (2.6) as the sum of the background potential temperature, $\bar{\theta}(z)$, and the perturbation potential temperature, $\theta(\vec{x}, t)$. The potential temperature is defined to be the temperature that a parcel of air would have if brought adiabatically down to the reference level at which $P_T = P_0$ (Kundu, 1990).

The conservation of mass for an anelastic gas is given by equation (2.7). This is an approximation to the continuity equation (2.5), and has the same effect as (2.3) in that it filters sound waves from the equations of motion. An anelastic gas is sometimes described as compressible, however, this compression is caused by the passage of an internal wave, and not by sound waves.

Equations (2.6) - (2.8) represent only one of a number of versions of the so-called anelastic approximation, known as the Ogura-Phillips anelastic model. This model requires that the potential temperature stratification be sufficiently weak (Klein, 2008), accomplished through the choice of a sufficiently large

potential temperature scale height, H_θ, as compared with the density scale height, H_ρ.

In the derivation of the anelastic gas equations, an approximation is made to relate the background and perturbation densities to the potential temperature. Using the ideal gas law and the definition of potential temperature we have:

$$\frac{\rho_T}{\rho_0} = \frac{\theta_0}{\theta_T}\left(\frac{P_T}{P_0}\right)^{(1/\gamma)}. \tag{2.10}$$

Here $\gamma = 1/(1-\kappa) \simeq 7/5$, and $\theta_0 \equiv T_0$, the characteristic value of the temperature at the ground where $P_T = P_0$. If we assume that the perturbation density and potential temperature variations are small compared to the background, then θ can be related to ρ via

$$\theta \simeq \bar{\theta}\left(-\frac{\rho}{\bar{\rho}} + \frac{1}{\gamma}\frac{P}{\bar{P}}\right). \tag{2.11}$$

The complicated relationship between these fields means that the anelastic gas equations can not be collapsed to the equations for a non-Boussinesq liquid.

Furthermore, the background potential temperature, $\bar{\theta}(z)$, and the background density, $\bar{\rho}(z)$, cannot be specified independently. Once the $\bar{\theta}$ profile has been specified, the background density is (Nault and Sutherland, 2008):

$$\bar{\rho} = \frac{\rho_0 T_0}{\bar{\theta}}\left[1 - \Gamma_d \int^z \frac{1}{\bar{\theta}(z)} dz\right]^{\frac{1-\kappa}{\kappa}}. \tag{2.12}$$

Here ρ_0 is the density at the reference level, and $\kappa \simeq 2/7$. The adiabatic lapse rate, Γ_d, is the rate of temperature decrease with height of a dry parcel of air moving upwards in an adiabatic atmosphere.

Apart from the use of θ rather than ρ in the conservation of momentum and internal energy equations, (2.6) and (2.8), there are two main differences between the anelastic gas and the non-Boussinesq liquid equations. While both sets of equations filter sound waves, the anelastic equations allow for expansion and contraction of the gas due to changes in pressure, while the

non-Boussinesq liquid is incompressible. The anelastic gas equations (2.6) - (2.8) also differ from their counterparts for a non-Boussinesq liquid (2.2) - (2.4) because they involve both the background density and the background potential temperature, which are related by (2.12). The lack of gas thermodynamics in the non-Boussinesq liquid equations is advantageous in that it allows us to study a system involving only the background density while nonetheless capturing many key features of anelastic wave development.

2.2 Dispersion Relations

The behaviour of small amplitude internal gravity waves is described by the dispersion relation and the polarization relations. This is done here for both an anelastic gas and a non-Boussinesq liquid. We begin by linearizing the equations of motion for an anelastic gas (this is done in standard textbooks, for an example see Gill (1982)):

$$\frac{\partial \vec{u}_T}{\partial t} = -\nabla\left(\frac{P}{\bar{\rho}}\right) + \frac{g}{\bar{\theta}}\theta\hat{z}, \tag{2.13}$$

$$\nabla \cdot (\bar{\rho}\vec{u}_T) = 0, \tag{2.14}$$

$$\frac{\partial \theta}{\partial t} = -w_T \frac{d\bar{\theta}}{dz}. \tag{2.15}$$

The total horizontal and vertical velocity fields are related to the total mass-streamfunction, Ψ_T, by $u_T = -\frac{1}{\bar{\rho}}\frac{\partial \Psi_T}{\partial z}$ and $w_T = \frac{1}{\bar{\rho}}\frac{\partial \Psi_T}{\partial x}$. The total spanwise vorticity field, $\zeta_T \equiv \nabla \times \vec{u}_T$, is given in terms of the mass-streamfunction by

$$\zeta_T = \frac{1}{\bar{\rho}}\left[-\nabla^2\Psi_T + \frac{1}{\bar{\rho}}\frac{d\bar{\rho}}{dz}\frac{\partial \Psi_T}{\partial z}\right]. \tag{2.16}$$

We now recast (2.13) as a single equation for the total mass-streamfunction and fluctuation potential temperature:

$$\frac{1}{\bar{\rho}}\frac{\partial}{\partial t}\nabla^2\Psi_T = \frac{g}{\bar{\theta}}\frac{\partial \theta}{\partial x} + \frac{1}{\bar{\rho}^2}\frac{d\bar{\rho}}{dz}\frac{\partial^2 \Psi_T}{\partial t \partial z}. \tag{2.17}$$

Using (2.15) to eliminate θ gives

$$\frac{\partial^2}{\partial t^2}\nabla^2\Psi = -\frac{g}{H_\theta}\frac{\partial^2\Psi}{\partial x^2} - \frac{1}{H_\rho}\frac{\partial^3\Psi}{\partial t^2 \partial z}, \tag{2.18}$$

where H_ρ is the density scale height in the fluid, defined by

$$H_\rho \equiv -\left(\frac{1}{\bar{\rho}}\frac{d\bar{\rho}}{dz}\right)^{-1}, \tag{2.19}$$

and H_θ is the potential temperature scale height,

$$H_\theta \equiv \left(\frac{1}{\bar{\theta}}\frac{d\bar{\theta}}{dz}\right)^{-1}. \tag{2.20}$$

Since we are concerned only with the wave dynamics in a stationary ambient, we have neglected any background motion so that in (2.18) the fluctuation mass-streamfunction is equal to the total mass-streamfunction $\Psi = \Psi_T$.

We assume that the background potential temperature is increasing exponentially, $\bar{\theta}(z) = \theta_0 \exp(z/H_\theta)$, so that the stratification is uniform. This leads to a constant squared buoyancy frequency of $N^2 \equiv (g/\bar{\theta})d\bar{\theta}/dz = g/H_\theta$. The buoyancy frequency, also referred to as the Brunt-Väisälä frequency, represents the natural frequency of oscillation of a vertically displaced fluid parcel (Kundu, 1990). The definition of the buoyancy frequency implies that $H_\theta = H_{\theta_0}$, and based on equation (2.12) we will also set $H_\rho \approx H_{\rho_0}$. Thus (2.18) becomes

$$\frac{\partial^2}{\partial t^2}\nabla^2\Psi = -N^2\frac{\partial^2\Psi}{\partial x^2} - \frac{1}{H_\rho}\frac{\partial^3\Psi}{\partial t^2 \partial z}, \tag{2.21}$$

in which we now have constant coefficients on the right-hand side of the equation.

We assume a plane wave solution of the form

$$f = A_f \exp\Big[\imath(\tilde{k}x + \tilde{m}z - \omega t)\Big] + c.c., \tag{2.22}$$

in which f can represent any of the basic state fields, and *c.c.* denotes the complex conjugate. A_f describes the one quarter peak-to-peak amplitude and phase of the wave, and $\tilde{k}$ and $\tilde{m}$ are constants.

Defining Formula	Relationship to Ψ
Ψ	A_Ψ
$u = -\frac{1}{\bar{\rho}}\partial_z \Psi$	$A_u = -\frac{1}{\bar{\rho}}\left(\imath m - \frac{1}{2H_\rho}\right) A_\Psi$
$w = \frac{1}{\bar{\rho}}\partial_x \Psi$	$A_w = -\frac{1}{\bar{\rho}}\imath k A_\Psi$
$\zeta = -\frac{1}{\bar{\rho}}[\nabla^2 \Psi + \frac{1}{H_\rho}\partial_z \Psi]$	$A_\zeta = \frac{1}{\bar{\rho}} N^2 \frac{k^2}{\omega^2} A_\Psi$
$w = \frac{\partial \xi}{\partial t}$	$A_\xi = -\frac{1}{\bar{\rho}}\frac{k}{\omega} A_\Psi$
$\xi \approx -\theta \left(\frac{\partial \bar{\theta}}{dz}\right)^{-1}$	$A_\theta \approx \frac{1}{\bar{\rho}}\frac{\partial \bar{\theta}}{dz}\frac{k}{\omega} A_\Psi$
$\rho \sim \frac{\bar{\rho}}{\bar{\theta}}\theta$	$A_\rho \sim -\frac{1}{H_\theta}\frac{k}{\omega} A_\Psi$

Table 2.1: Polarization relations for small amplitude waves in an anelastic gas.

Substituting (2.22) into (2.21) with $f = \Psi$ we see that internal waves in an anelastic gas satisfy

$$\omega^2 = N^2 \frac{\tilde{k}^2}{\tilde{k}^2 + \tilde{m}^2 - \imath \frac{\tilde{m}}{H_\rho}}. \tag{2.23}$$

Since the background mean flow is assumed constant, we have that ω and $\tilde{k} = k$ must be real-valued. This implies that the imaginary part of $\tilde{m}^2 + \imath \frac{\tilde{m}}{H_\rho}$ must be zero. This condition requires that $\tilde{m}_i = \frac{1}{2H_\rho}$. Setting the real part of $\tilde{m}$ equal to the vertical wavenumber m, we conclude that the frequency of small amplitude anelastic internal gravity waves is given by the dispersion relation,

$$\omega = N \frac{k}{\left(k^2 + m^2 + \frac{1}{4H_\rho^2}\right)^{1/2}}. \tag{2.24}$$

in which k and m are the horizontal and vertical wavenumbers respectively. This corresponds to a plane wave whose mass-streamfunction has the form

$$\Psi = A_\Psi \exp\left[\imath(kx + mz - \omega t) - z/2H_\rho\right] + c.c. \tag{2.25}$$

The polarization relations of other fields are listed in Table 2.1. Although the mass-streamfunction is predicted to decrease in amplitude exponentially over an e-folding distance $2H_\rho$, most other wave fields are related to Ψ through a factor proportional to $1/\bar{\rho}$, given by (2.12), which increases exponentially

with height faster than the exponential decrease described by $\exp(-z/2H_\rho)$. Note that (2.25) combined with the polarization relations for u and w predict exponential growth of velocity fluctuations with height. This is referred to as anelastic growth.

We now repeat the above procedure for internal gravity waves in a non-Boussinesq liquid (this is done for the first time in this thesis). We first linearize the equations of motion (2.2) - (2.4) as follows:

$$\bar{\rho}\frac{\partial \vec{u_T}}{\partial t} = -\nabla P - g\rho\hat{z}, \tag{2.26}$$

$$\nabla \cdot \vec{u_T} = 0, \tag{2.27}$$

$$\frac{\partial \rho}{\partial t} = -w_T\frac{d\bar{\rho}}{dz}. \tag{2.28}$$

As a consequence of (2.27), the components of the total horizontal and vertical velocity fields are given in terms of a scalar function, the total streamfunction ψ_T, by $u_T = -\partial_z\psi_T$ and $w_T = \partial_x\psi_T$, respectively. This is different from the mass-streamfunction used in the anelastic case, as it does not include the background density. The total vorticity field corresponding to the streamfunction is $\zeta_T \equiv \partial_z u_T - \partial_x w_T = -\nabla^2\psi_T$. Thus, the linearized momentum conservation equations can be recast as one equation for the total streamfunction and fluctuation density

$$\frac{\partial^2}{\partial t^2}\nabla^2\psi_T = -\frac{g}{\bar{\rho}}\frac{\partial \rho}{\partial x} - \frac{1}{\bar{\rho}}\frac{d\bar{\rho}}{dz}\frac{\partial^2\psi_T}{\partial t\partial z}. \tag{2.29}$$

Using (2.28) to eliminate ρ leads to the equation

$$\frac{\partial^2}{\partial t^2}\nabla^2\psi = -\frac{g}{H_\rho}\frac{\partial^2\psi}{\partial x^2} + \frac{1}{H_\rho}\frac{\partial^3\psi}{\partial t^2\partial z}. \tag{2.30}$$

In (2.30) we have neglected any background motion independent of the waves, so that the fluctuation streamfunction is equal to the total streamfunction, $\psi = \psi_T$.

Defining Formula	Relationship to ψ
ψ	A_ψ
$u = -\partial_z \psi$	$A_u = -\left(\imath m + \frac{1}{2H_\rho}\right) A_\psi$
$w = \partial_x \psi$	$A_w = -\imath k A_\psi$
$\zeta = -\nabla^2 \psi$	$A_\zeta = \left(k^2 + m^2 - \frac{1}{4H_\rho^2} - \imath \frac{m}{H_\rho}\right) A_\psi$
$w = \frac{\partial \xi}{\partial t}$	$A_\xi = -\frac{k}{\omega} A_\psi$
$\xi \approx H_\rho \frac{\rho}{\bar{\rho}}$	$A_\rho \approx -\bar{\rho} \frac{k}{H_\rho \omega} A_\psi$

Table 2.2: Polarization relations for small amplitude waves in a non-Boussinesq liquid.

We assume the liquid is uniformly stratified so that $\bar{\rho} = \rho_0 \exp(-z/H_\rho)$. In contrast to the anelastic case, it is the background density that is changing exponentially, rather than the potential temperature. The squared buoyancy frequency, given for a non-Boussinesq liquid by $N^2 \equiv -(g/\bar{\rho}) d\bar{\rho}/dz = g/H_\rho$, is therefore constant. Substituting this form into (2.30) results in an equation that is identical to (2.21) for an anelastic gas, with Ψ replaced by ψ.

The frequency of small amplitude non-Boussinesq internal waves is therefore given by a dispersion relation identical to that for small amplitude internal waves in an anelastic gas; equation (2.24). The streamfunction of a non-Boussinesq plane wave has the form

$$\psi = A_\psi \exp\left[\imath(kx + mz - \omega t) + z/2H_\rho\right] + c.c. \tag{2.31}$$

This increases exponentially with height, in contrast to the behaviour of the mass-streamfunction for an anelastic gas (2.25). The polarization relations of other fields for a non-Boussinesq liquid are listed in Table 2.2.

2.3 Wave-induced mean flow

The form for the wave-induced mean flow of internal gravity waves in an anelastic gas was rigorously derived using Hamiltonian fluid dynamics (Scinocca and Shepherd, 1992), and is given by equation (1.1). It is possible to gain an un-

derstanding of the physical meaning the wave-induced mean flow in this form by using Stokes' Theorem, as described in Appendix A.

The wave-induced mean flow as given by equation (1.1) can be recast in terms of the mass-streamfunction amplitude, A_Ψ, via the polarization relations for anelastic internal gravity waves:

$$U = \frac{1}{2} N^2 \frac{k^3}{\omega^3} \frac{1}{\bar{\rho}^2} |A_\Psi|^2 \exp(-z/H_\rho). \tag{2.32}$$

Note that U increases with height as a direct consequence of momentum conservation, which requires $\bar{\rho}U$ to be constant with height. We can also express U in terms of the initial vertical displacement of the waves, A_ξ, as:

$$U = \frac{1}{2} N^2 \frac{k}{\omega} \frac{1}{\bar{\rho}^2} |A_\xi|^2 \exp(-z/H_\rho). \tag{2.33}$$

While (1.1) describes the wave-induced mean flow for Boussinesq waves and for anelastic waves in a gas, the corresponding form for non-Boussinesq waves in a liquid has not previously been determined. We will do so based on momentum conservation arguments.

This task is non-trivial because plane internal gravity waves are an exact solution to the fully nonlinear equations. To see this, consider the advective terms in the governing equations. If we evaluate the fluctuation quantities using the polarization relations we see that the advective operator becomes

$$\vec{u} \cdot \nabla \quad \rightarrow \quad u(\imath k) + w(\imath m + \frac{1}{2H_\rho}) \quad = \quad \imath k u + \imath m w + \frac{w}{2H_\rho}. \tag{2.34}$$

However, equation (2.3) gives $\imath k u + \imath m w + w/2H_\rho = 0$. Therefore, the nonlinear advective terms in the fully nonlinear equations evaluate to zero. As a consequence, the standard procedure first developed by Stokes to derive the formula for the drift associated with surface waves (Whitham, 1974) cannot be applied to internal waves.

Instead we develop a formula for the drift associated with internal waves based upon the evolution of wavepackets. Assuming the waves are horizontally

periodic but have localized structure in the vertical, we write a wavepacket in the form:

$$f = A_f(z,t)\exp\left[\imath(kx + mz - \omega t) + z/2H_\rho\right] + c.c., \tag{2.35}$$

where f can represent any of the basic state fields and $A_f(z,t)$ specifies the shape of the wavepacket envelope. Following the typical approach, detailed for example by Bretherton (1966), we require that our wavepacket experience slow enough amplitude modulation that the packet is quasi-monochromatic and propagates vertically at the group velocity, $c_{gz} = \partial\omega/\partial m$.

The total velocity field $\vec{u_T}(x,z,t)$ is separated into the mean horizontal flow induced by the waves, $U(z,t)$, and the fluctuation velocities (u,w). In order to derive an equation for U, we begin by writing the horizontal momentum equation from (2.2) in flux-form using (2.3):

$$\partial_t u_T = -\left[\partial_x(u_T u_T) + \partial_z(u_T w_T) + \frac{1}{\bar{\rho}}\partial_x P\right]. \tag{2.36}$$

To determine the wave-induced mean flow at leading order, we then extract terms independent of x on the right-hand side of (2.36). For example, for two fields f and g, each of the form (2.35), the x-independent part of the product fg is $(A_f(A_g)^\star + (A_f)^\star A_g)\exp(z/H_\rho)$, in which the star denotes the complex conjugate. This operation is equivalent to computing the horizontal average. Expanding $u_T = U + u$ and $w_T = w$, for which $\langle u\rangle = \langle w\rangle = 0$, and identifying the left-hand side of (2.36) as the time rate of change of the wave-induced mean flow gives

$$\partial_t U = -\partial_z \langle uw\rangle . \tag{2.37}$$

In order to implement perturbation theory, we shift into a reference frame moving at the vertical group speed of the wavepacket, c_{gz}, so that the new vertical co-ordinate is given by $Z \equiv \epsilon(z - c_{gz}t)$ and the new time co-ordinate is $T \equiv \epsilon^2 t$. Here $\epsilon \equiv 1/(k\sigma)$ is a non-dimensional measure of the vertical extent, σ, of the wavepacket amplitude envelope. Our time co-ordinate measures the

slow evolution of the wavepacket envelope due to linear dispersion. This scales as ϵ^2 according to the terms on the right-hand side of equation (1.5).

Thus to order ϵ we have $\partial_t U \approx -c_{gz}\partial_Z U$ and $\partial_z \langle uw \rangle \approx \partial_Z \langle uw \rangle$ in (2.37). Provided the wavepacket is so broad that $\epsilon \ll 1$, perturbation theory at first order leads to

$$c_{gz}\partial_Z U = \partial_Z \langle uw \rangle . \tag{2.38}$$

Integrating both sides with respect to Z leads to the final form for the wave-induced mean flow

$$U = \frac{1}{c_{gz}} \langle uw \rangle , \tag{2.39}$$

which is identical to (1.4), although that formula was derived heuristically from wave action conservation for plane waves. Equation (2.39) represents the wave-induced mean flow for a wavepacket in a Boussinesq fluid or a non-Boussinesq liquid. In the former case, the polarization relations can be used to show that (2.39) is equivalent to (1.1).

The derivation of (2.39) shows that the wave-induced mean flow of a wavepacket is essentially the result of momentum being transported upward at the vertical group velocity: $\bar{\rho} \langle uw \rangle = c_{gz}(\bar{\rho}U)$. That is, the vertical flux of horizontal momentum is equal to the transport of the momentum associated with the wave-induced mean flow moving upwards at the group velocity. This is analogous to the vertical flux of energy, which is well known to equal the transport of energy upwards at the vertical group velocity.

The wave-induced mean flow can be related to the vertical displacement amplitude of the wavepacket, A_ξ, at leading order through the use of polarization relations for non-Boussinesq internal gravity waves. Then (2.39) becomes

$$U = \frac{1}{2} N^2 \frac{k}{\omega} |A_\xi|^2 \exp\left(z/H_\rho\right) . \tag{2.40}$$

This is given in terms of the stationary co-ordinate z. The time evolution of U is given by shifting to the translating co-ordinate Z.

2.4 Anelastic Schrödinger equation

Now that the forms for the wave-induced mean flow in both a non-Boussinesq liquid and an anelastic gas have been determined, it is possible to derive the nonlinear Schrödinger equations describing the weakly nonlinear evolution of the waves. We will begin with the case of an anelastic gas. The derivation of the weakly nonlinear Schrödinger equation for internal gravity waves in an anelastic gas combines the vertical and horizontal conservation of momentum equations from (2.6) with the energy conservation equation (2.8) and the incompressibility condition (2.7). Note that in the development of the weakly nonlinear equations viscosity will be neglected. We assume an approximately constant density scale height, $H_\rho \approx H_{\rho_0}$, and a constant background buoyancy frequency, N, over the width of the wavepacket, as was done in the derivation of the dispersion relation.

The first step in the derivation is to take the cross-product of the momentum equation so that the pressure gradient terms are eliminated:

$$\begin{aligned} & \frac{\partial}{\partial z}\left[\frac{Du_T}{Dt} = -\frac{\partial}{\partial x}\left(\frac{P}{\bar{\rho}}\right)\right] \\ - \quad & \frac{\partial}{\partial x}\left[\frac{Dw_T}{Dt} = -\frac{\partial}{\partial z}\left(\frac{P}{\bar{\rho}}\right) + \frac{g}{\bar{\theta}}\theta\right] \end{aligned}$$

The resulting equation, once the derivatives of each term in the material derivative have been evaluated, becomes

$$\frac{D}{Dt}\left[\partial_z u_T - \partial_x w_T\right] = -\frac{g}{\bar{\theta}}\partial_x\theta - \left[\partial_x u_T + \partial_z w_T\right]\left[\partial_z u_T - \partial_x w_T\right],$$

in which partial derivatives have now been denoted by subscripts on ∂ for convenience. In order to simplify the last term on the right hand side, we use (2.7):

$$\nabla\cdot\left(\bar{\rho}\vec{u}_T\right) = \bar{\rho}\left(\partial_x u_T + \partial_z w_T\right) + \frac{d\bar{\rho}}{dz}w_T = 0.$$

Combining this with the definition of the vorticity, $\zeta_T \equiv \partial_z u_T - \partial_x w_T$, results in the following equation for the total vorticity and the perturbation potential

temperature fields:

$$\frac{D}{Dt}\zeta_T = -\frac{g}{\bar{\theta}}\frac{\partial\theta}{\partial x} - \frac{1}{H_\rho}w_T\zeta_T. \tag{2.41}$$

We replace ζ with the mass-streamfunction Ψ via (2.16) and (2.19), to give

$$\frac{D}{Dt}\left\{-\frac{1}{\bar{\rho}}\left[\nabla^2\Psi_T + \frac{1}{H_\rho}\frac{\partial\Psi_T}{\partial z}\right]\right\} = -\frac{g}{\bar{\theta}}\frac{\partial\theta}{\partial x} - \frac{w_T}{H_\rho}\left\{-\frac{1}{\bar{\rho}}\left[\nabla^2\Psi_T + \frac{1}{H_\rho}\frac{\partial\Psi_T}{\partial z}\right]\right\}.$$

In order to put this equation into a more tractable form, it is first necessary to expand the terms and then simplify. The primary steps are as follows: expand the material derivative, multiply out all the terms, and bring everything except the term involving the perturbation potential temperature onto the left-hand side of the equation. At this stage in the derivation, the following substitutions are made:

$$\begin{aligned}
\Psi_T(x,z,t) &= \Psi(x,z,t) + \bar{\Psi}(z,t), \\
u_T(x,z,t) &= u(x,z,t) + U(z,t) = -\frac{1}{\bar{\rho}}\frac{\partial\Psi}{\partial z} - \frac{1}{\bar{\rho}}\frac{\partial\bar{\Psi}}{\partial z}, \\
w_T(x,z,t) &= w(x,z,t) = \frac{1}{\bar{\rho}}\frac{\partial\Psi}{\partial x}.
\end{aligned}$$

The resulting equation will contain only the perturbation mass-streamfunction, Ψ, the wave-induced mean flow, $U = -\frac{1}{\bar{\rho}}\partial_z\bar{\Psi}$, the background density, $\bar{\rho}$, and the perturbation potential temperature, θ, as variables.

If we replace the acceleration due to gravity by $H_\theta N^2$, and simplify terms involving the background potential temperature using the definition of the potential temperature scale height (2.20), we have

$$\begin{aligned}
&\partial_{txx}\Psi + \partial_{tzz}\Psi + \frac{1}{H_\rho}\partial_{tz}\Psi + U\partial_{xxx}\Psi + U\partial_{xzz}\Psi + \\
&\frac{1}{H_\rho}U\partial_{xz}\Psi - \frac{1}{H_\rho}\partial_z U\partial_x\Psi - \partial_{zz}U\partial_x\Psi \\
= \;& N^2\bar{\rho}\left(\frac{d\bar{\theta}}{dz}\right)^{-1}\partial_x\theta.
\end{aligned} \tag{2.42}$$

We are looking for an equation that will capture the evolution of the waves due only to their interactions with the wave-induced mean flow. If the mass-streamfunction and potential temperature of the wavepackets are expressed

as

$$\begin{aligned}\Psi &= A_\Psi(z,t)\exp(\imath kx + \imath mz - \imath\omega t - z/2H_\rho) + c.c.,\\ \theta &= A_\theta(z,t)\exp(\imath kx + \imath mz - \imath\omega t - z/2H_\rho) + c.c.,\end{aligned}$$

then only the $\exp(\imath kx + \imath mz - \imath\omega t - z/2H_\rho)$ terms represent the wave-like behaviour we are trying to capture. Any other terms will be neglected.

Now we convert (2.42) into an equation for A_Ψ and A_θ, keeping in mind that the amplitude of the wavepacket can change with time, t, and height, z. Thus, derivatives with respect to x will introduce factors of $\imath k$, derivatives with respect to t will introduce factors of $[\partial_t - \imath\omega]$, and z-derivatives will introduce factors of $\left(\partial_z + \imath m - \frac{1}{2H_\rho}\right)$, in which the derivatives now act only on the envelope functions A_Ψ and A_θ. Following some simplification of terms, (2.42) becomes a differential equation for the evolution of the amplitude envelope:

$$\begin{aligned}\left\{\left(\partial_t - \imath\left[\omega - kU\right]\right)\left[-k^2 - m^2 - \frac{1}{4H_\rho^2} + \partial_{zz} + 2\imath m\partial_z\right] - \right.\\ \left.\imath k\left[\frac{1}{H_\rho}\partial_z U + \partial_{zz}U\right]\right\} A_\Psi = \imath k N^2 \bar{\rho}\left(\frac{d\bar{\theta}}{dz}\right)^{-1} A_\theta. \qquad (2.43)\end{aligned}$$

So far, we have combined three out of the four governing equations. If we apply a similar procedure to (2.8), we arrive at a second differential equation for the perturbation mass-streamfunction and potential temperature amplitude envelopes:

$$\left(\partial_t - \imath\left[\omega - kU\right]\right) A_\theta = -\imath k \frac{1}{\bar{\rho}}\frac{d\bar{\theta}}{dz} A_\Psi. \qquad (2.44)$$

We combine this equation with (2.43) to eliminate the potential temperature, by multiplying both the LHS and RHS of that equation by $(\partial_t - \imath\left[\omega - kU\right])$. This results in a single differential equation describing the evolution of A_Ψ:

$$\begin{aligned}&\left(\partial_t - \imath\left[\omega - kU\right]\right) \times\\ &\left\{\left(\partial_t - \imath\left[\omega - kU\right]\right)\left[\partial_{zz} + 2\imath m\partial_z - \kappa^2 - \tfrac{1}{4H_\rho^2}\right] - \imath k\left[\partial_{zz}U + \tfrac{1}{H_\rho}\partial_z U\right]\right\} A_\Psi\\ &= k^2 N^2 A_\Psi \qquad (2.45)\end{aligned}$$

in which $\kappa^2 \equiv k^2 + m^2$.

To arrive at the nonlinear Schrödinger equation, we use a perturbation expansion retaining terms up to third order. First we shift into a frame moving at the initial vertical group velocity of the wave. Our new vertical co-ordinate is given by $Z = \epsilon(z - c_{gz}t)$ so that $\partial_z = \epsilon\partial_Z$, and our new time co-ordinate is $T = \epsilon^2 t$ so that $\partial_t = \epsilon^2\partial_T - \epsilon c_{gz}\partial_Z$. Here ϵ is a small parameter, defined as $\epsilon \equiv 1/(k\sigma) \ll 1$, with σ being the vertical width of the wavepacket's amplitude envelope. Furthermore, for leading order dispersion to balance nonlinearity, we require that the maximum amplitude of the initial mass-streamfunction field be large enough such that $\beta \equiv \|A_{\Psi_0}\|(k^2/\rho_0 N^2)$ is of order ϵ. This also implies that the wave-induced mean flow U, which is proportional to the amplitude squared, will scale as ϵ^2. We apply this transformation to equation (2.45), multiply out the terms, and then group according to their order in ϵ. It is important to note that Z-derivatives act on U as well as on A_Ψ, meaning that the order of multiplication is crucial.

The resulting equation contains terms up to order ϵ^6. The order ϵ^0 terms reproduce the dispersion relation (2.24). Since we have shifted into a frame of reference moving at the vertical group velocity, the order ϵ^1 terms give $0 = 0$. The second result justifies our use of the polarization relations from linear theory in the derivation of (2.45). At order ϵ^2, the equation is

$$\left\{2\omega\left[\imath\partial_t - kU\right]\left[\kappa^2 + \frac{1}{4H_\rho^2}\right] + \omega^2\left[\frac{3m^2}{\kappa^2 + \frac{1}{4H_\rho^2}} - 1\right]\partial_{ZZ}\right\} A_\Psi = 0,$$

and at order ϵ^3 we have:

$$\left\{2\omega m\partial_T\partial_Z + 2\imath\omega mkU\partial_Z - \omega k\left[\imath m + \tfrac{1}{H_\rho}\right]\partial_Z U + \tfrac{2\imath\omega^2 m}{\kappa^2 + \frac{1}{4H_\rho^2}}\left[\tfrac{m^2}{\kappa^2 + \frac{1}{4H_\rho^2}} - 1\right]\partial_{ZZZ}\right\} A_\Psi = 0.$$

In order to combine these two equations, we expand our amplitude envelope function as a power series in ϵ so that $A_\Psi = A_0 + \epsilon^1 A_1 + \epsilon^2 A_2 + ...$, and then

add the order ϵ^2 equation to the order ϵ^3 equation. We once again extract the order ϵ^2 and ϵ^3 pieces, and use the ϵ^2 equation to eliminate the $\partial_T \partial_Z$ term in the ϵ^3 equation. Recasting the resulting equation in terms of A_Ψ and our original co-ordinates z and t gives the weakly nonlinear Schrödinger equation for waves in an anelastic gas:

$$\partial_t A_\Psi + c_{gz}\partial_z A_\Psi = \tag{2.46}$$
$$\imath\tfrac{1}{2}\omega_{mm}\partial_{zz}A_\Psi + \tfrac{1}{6}\omega_{mmm}\partial_{zzz}A_\Psi - \imath k U A_\Psi + \tfrac{1}{2}\tfrac{\omega^2}{N^2 k}\left(3m - \tfrac{\imath}{H_\rho}\right)(\partial_z U)\, A_\Psi.$$

The coefficients of the terms on the right-hand side are

$$\omega_{mm} = \tfrac{\partial^2\omega}{\partial m^2} = \tfrac{w}{\kappa^2 + \frac{1}{4H_\rho^2}}\left[\tfrac{3m^2}{\kappa^2+\frac{1}{4H_\rho^2}} - 1\right],$$
$$\omega_{mmm} = \tfrac{\partial^3\omega}{\partial m^3} = \tfrac{-3\omega m}{\left(\kappa^2+\frac{1}{4H_\rho^2}\right)^2}\left[\tfrac{5m^2}{\kappa^2+\frac{1}{4H_\rho^2}} - 3\right]. \tag{2.47}$$

The wave-induced mean flow, U, which is proportional to $|A_\Psi|^2$, is given by (2.32).

Comparing (2.46) to (1.5), we see it includes terms describing the translation of the wavepacket at the vertical group velocity (second term on the LHS) as well as second and third order linear dispersion terms (first and second terms on the RHS). Note that the 'leading-order' linear dispersion term is actually second order in ϵ. The second term on the right hand side of (2.46), which is third-order in ϵ, is necessary to capture the linear dispersion of waves moving close to the fastest vertical group velocity, for which $\omega_{mm} \approx 0$.

The nonlinear third term on the right hand side of (2.46) represents the Doppler shifting of the waves by the wave-induced mean flow. This is a type of nonlinear dispersion in which the extrinsic frequency of the waves, $\Omega = \omega - kU$, is modified by their interactions with the induced mean flow. The last term on the right hand side of (2.46) is also a third-order term accounting for nonlinear dispersion resulting from the shear associated with the wave-induced mean flow. This term captures effects unique to waves in an anelastic fluid. We

will show that including the third-order linear and nonlinear dispersion terms is necessary to capture the symmetry breaking observed for modulationally unstable waves.

With the inclusion of only the first three terms on the right-hand side of (2.46), in the limit $H_\rho \to \infty$, the equation becomes that derived for Boussinesq waves (Sutherland, 2006b). If we also neglect the third-order term, we are left with a special case of the formula derived by Akylas and Tabaei (2005).

2.5 Non-Boussinesq Schrödinger equation

We now turn our attention to the derivation of the corresponding weakly nonlinear Schrödinger equation for internal waves in a non-Boussinesq liquid. Our approach is a continuation of the procedure used to find the wave-induced mean flow, (2.39). Returning to the governing equations, we take the curl of the momentum conservation equations given by (2.2) and, using (2.3), get two coupled nonlinear equations for the total streamfunction and the fluctuation density:

$$\frac{D}{Dt}\nabla^2\psi_T = -\frac{g}{\bar{\rho}}\frac{\partial\rho}{\partial x} - \frac{1}{\bar{\rho}}\frac{d\bar{\rho}}{dz}\frac{D}{Dt}\partial_z\psi_T, \tag{2.48}$$

$$\frac{D\rho}{Dt} = -\frac{d\bar{\rho}}{dz}\frac{\partial\psi}{\partial x}. \tag{2.49}$$

In the case of uniform stratification, for which we have an exponentially decreasing background density profile, the vertical displacement of the waves, ξ, is related to the fluctuation density by

$$\xi = -H_\rho \ln\left[1 - \frac{\rho}{\bar{\rho}}\right] \approx H_\rho\frac{\rho}{\bar{\rho}}, \tag{2.50}$$

the approximation being valid if $|\rho/\bar{\rho}| \ll 1$. Using the polarization relations, we can also relate ξ to the streamfunction through $A_\xi = -(k/\omega)A_\psi$.

Our goal is to derive an approximate equation for the weakly nonlinear evolution of the wavepacket in terms of the vertical displacement amplitude

envelope $A_\xi(z,t)$. We will assume that initial weakly nonlinear effects result only from interactions between the waves and the wave-induced mean flow. Thus we write $\psi_T = \bar{\psi} + \psi$ with $U = -\partial_z \bar{\psi}$ and U given by equation (2.39). Following the approach of Sutherland (2006b), (2.48) and (2.35) are combined and the coefficients of the $\exp[\imath(kx + mz - \omega t) + z/2H_\rho]$ terms are extracted to give a differential equation for the streamfunction and vertical displacement amplitude envelopes, A_ψ and A_ξ:

$$\left\{ [\partial_t - \imath(\omega - kU)] \left[\partial_{zz} + 2\imath m \partial_z - \kappa^2 - \frac{1}{4H_\rho^2} \right] \right. \\ \left. -\imath k \left[\partial_{zz} U - \frac{1}{H_\rho} \partial_z U \right] \right\} A_\psi = -\imath k N^2 A_\xi. \tag{2.51}$$

Independently, (2.50) and (2.49) are combined with (2.35) to give a second equation for A_ψ and A_ξ:

$$[\partial_t - \imath(\omega - kU)] A_\xi = \imath k A_\psi, \tag{2.52}$$

in which we have once again extracted only the coefficients of the wave-like terms occurring in combination with $\exp[\imath(kx + mz - \omega t) + z/2H_\rho]$.

Equation (2.52) is used to eliminate A_ψ from (2.51), resulting in a single differential equation for the evolution of A_ξ:

$$\left\{ [\partial_t - \imath(\omega - kU)][\partial_{zz} + 2\imath m \partial_z - \kappa^2 - \tfrac{1}{4H_\rho^2}] - \imath k [\partial_{zz} U - \tfrac{1}{H_\rho} \partial_z U] \right\} \times \\ [\partial_t - \imath(\omega - kU)] A_\xi = k^2 N^2 A_\xi, \tag{2.53}$$

in which U is given by (2.39). This equation differs from the anelastic equation (2.45) in the sign of the $\partial_z U$ term, the location of the $[\partial_t - \imath(\omega - kU)]$ operator, and in the use of A_ξ rather than A_Ψ.

We transform into a frame of reference with vertical co-ordinate $Z \equiv \epsilon(z - c_{gz} t)$ and time co-ordinate $T \equiv \epsilon^2 t$ and we apply perturbation theory requiring that the vertical width of the wavepacket be sufficiently large such that $\epsilon \equiv 1/(k\sigma) \ll 1$. For leading order dispersion to balance nonlinearity we require

that the maximum vertical displacement A_{ξ_0} be large enough such that $\alpha \equiv \|A_{\xi_0}\|k$ is of order ϵ. Keeping terms up to third order in ϵ and recasting the result in terms of z and t gives the weakly nonlinear Schrödinger equation for A_ξ:

$$\partial_t A_\xi + c_{gz}\partial_z A_\xi = \tag{2.54}$$
$$\imath\tfrac{1}{2}\omega_{mm}\partial_{zz}A_\xi + \tfrac{1}{6}\omega_{mmm}\partial_{zzz}A_\xi - \imath k U A_\xi + \tfrac{1}{2}\tfrac{\omega^2}{N^2 k}\left(m + \tfrac{\imath}{H_\rho}\right)(\partial_z U)\, A_\xi.$$

Here the left-hand side explicitly includes the advective derivative describing the vertical translation of the wavepacket at the group velocity. The coefficients of the linear terms on the right-hand side are given by (2.47), as in the anelastic case. A comparison of this equation with its anelastic counterpart (2.46) reveals a surprising similarity. The only differences are the choice of A_ξ instead of A_Ψ, and the coefficient of the $(\partial_z U)\, A_\xi$ term. This similarity in the weakly nonlinear equations re-emphasizes the potential usefulness of the equations for a non-Boussinesq liquid as a proxy for the more complicated case of an anelastic gas.

Chapter 3

Numerics

In order to determine how accurately the nonlinear Schrödinger equations (2.46) and (2.54) capture the evolution of a two dimensional, vertically localized, horizontally periodic wavepacket, numerically integrated solutions of these equations will be compared with the results of fully nonlinear numerical simulations of wavepacket propagation in uniformly stratified fluid with no background shear save that due to the wave-induced mean flow.

3.1 Non-dimensionalization

We non-dimensionalize the equations used in both the weakly and the fully nonlinear numerical simulations so that the relative space and time scales are set by N and k. We choose the characteristic length scale to be $L = k^{-1}$ and the time scale to be $T = N^{-1}$, in which $N^2 = g/H_\theta$ for an anelastic gas and $N^2 = g/H_\rho$ for a non-Boussinesq liquid. The results given here will be normalized by these parameters or, where conceptually convenient, by the horizontal wavelength $\lambda_x = 2\pi/k$ and the buoyancy period $T_B = 2\pi/N$.

In the atmosphere, a typical value of H_θ is 100km and a typical value of H_ρ is 10km. With $g \approx 10\text{m/s}^2$, this gives $N \approx 0.01\text{s}^{-1}$ for an anelastic gas or $N \approx 0.03\text{s}^{-1}$ for a non-Boussinesq liquid. Internal waves in the atmosphere have a wide range of spatial scales, which depend on their generation mechanism.

m/k	ω/N	$c_{gz}\frac{k}{N}$	$\omega_{mm}\frac{k^2}{N}$	$\omega_{mmm}\frac{k^3}{N}$
-0.4	0.93	0.32	-0.470	-1.91
-0.7	0.82	0.38	-0.008	-1.05
-1.4	0.58	0.27	0.193	0.09

Table 3.1: Relevant parameters and coefficients of (2.46) & (2.54) for the anelastic gas and non-Boussinesq liquid simulations presented herein.

For the waves considered herein, typical values of the horizontal wavenumber range from $k = 0.1\text{km}^{-1}$ to 10km^{-1}, which correspond to characteristic length scales from $L = 10\text{km}$ to 0.1km.

The background potential temperature will be normalized by a constant characteristic value θ_0, and the background density by ρ_0. Typical atmospheric values are $\theta_0 \approx 300\text{K}$ and $\rho_0 \approx 1\text{kg/m}^3$. The perturbation potential temperature and density are normalized by H_θ/θ_0 and H_ρ/ρ_0 respectively, reflecting the relatively small scale of the perturbations fields compared to background variations.

The normalized parameters for the simulations examined in detail are provided in Table 3.1. The corresponding initial wavepacket amplitudes, α and β, as well as the initial and maximum values of the wave-induced mean flow, U_0 and U_{Max}, are given in Table 3.2. These values are used in the normalization of the wave-induced mean flow field for the figures presented in §4. In all cases the waves start with a relatively small amplitude and are allowed to propagate vertically upward. An initial exponential increase in amplitude as predicted by linear theory followed by the development of weakly nonlinear effects is anticipated.

We will begin by describing the numerical solution of the fully nonlinear anelastic equations in detail. The solution method for the non-Boussinesq simulations is similar, and the discrepancies between the two methods are detailed in section 3.3.

	Anelastic			*Non-Boussinesq*		
m/k	β	$U_0\frac{k}{N}$	$U_{\text{Max}}\frac{k}{N}$	α	$U_0\frac{k}{N}$	$U_{\text{Max}}\frac{k}{N}$
-0.4	0.001	0.00006	0.00029	0.03	0.00051	0.031
-0.7	0.001	0.00008	0.00072	0.03	0.00057	0.066
-1.4	0.001	0.00024	0.00076	0.03	0.00081	0.015
-0.4	0.015	0.020	0.15	0.07	0.0026	0.19
-0.7	0.015	0.023	0.21	0.07	0.0029	0.22
-1.4	0.015	0.032	0.11	0.07	0.0041	0.06

Table 3.2: Relevant initial wavepacket amplitudes and initial and maximum values of the wave-induced mean flow for the anelastic gas and the non-Boussinesq liquid simulations.

3.2 Fully Nonlinear Anelastic Code

The fully nonlinear anelastic code solves the coupled equations for spanwise vorticity and potential temperature with the effects of viscosity and thermal diffusion included to damp small-scale noise and ensure numerical stability. Explicitly, the vorticity equation is

$$\frac{D\zeta_T}{Dt} = -\frac{1}{H_\rho} w\zeta_T - \frac{g}{\bar{\theta}}\frac{\partial\theta}{\partial x} + \nu\nabla^2\zeta_T, \tag{3.1}$$

where ν is the kinematic viscosity, defined as the ratio of the viscous and the inertial forces. Cast in non-dimensional form, this becomes

$$\frac{D\zeta_T}{Dt} = -\frac{L}{H_\rho} w\zeta_T - \frac{1}{\bar{\theta}}\frac{\partial\theta}{\partial x} + \frac{1}{\text{Re}}\nabla^2\zeta_T. \tag{3.2}$$

Here the Reynolds number is defined as $\text{Re} \equiv \frac{\nu k^2}{N}$. The bulk Richardson number, which is the ratio of the buoyancy and the inertial forces (Kundu, 1990), has been set to $J = 1$.

The internal energy equation (2.8) is modified by the addition of the diffusion term $\kappa\nabla^2\theta$, in which κ is the thermal diffusivity. In non-dimensional form this is

$$\frac{D\theta}{Dt} = -w\frac{d\bar{\theta}}{dz} + \frac{1}{\text{RePr}}\nabla^2\theta, \tag{3.3}$$

in which the Prandtl number is given by $\text{Pr} \equiv \nu/\kappa$.

Both the Reynolds number and the Prandtl number are chosen to be sufficiently large that diffusion negligibly affects the wave evolution. To ensure this, Pr is set equal to 1 and Re is set to be 10000. No significant changes in the wave dynamics were found by decreasing the Reynolds number to 5000.

Generally the code is designed to allow for the specification of arbitrary background potential temperature profiles, $\bar{\theta}(z)$, and arbitrary background mean wind profiles, $\bar{U}(z)$. For the runs presented herein, however, we assume the gas is uniformly stratified so that $\bar{\theta} = \theta_0 \exp(z/H_\theta)$ and we assume the ambient flow is uniform so that $\bar{U}(z) = U_{00}$, in which U_{00} is a constant value, typically zero.

In the code, the background density profile, $\bar{\rho}(z)$, is calculated using the non-dimensional form of (2.12):

$$\bar{\rho} = \frac{1}{\bar{\theta}} \left[1 - \Gamma_d \int^z \frac{1}{\bar{\theta}(z)} dz \right]^{\frac{5}{2}}, \tag{3.4}$$

in which the non-dimensional adiabatic lapse rate is

$$\Gamma_d \equiv \frac{g}{c_p} \frac{H_\theta}{\theta_0}, \tag{3.5}$$

and c_p is the specific heat capacity at constant pressure. In the code, this indefinite integral is evaluated numerically at each vertical level. The constant of integration is implicitly determined by the choice of H_ρ and H_θ. Due to the presence of a $\frac{5}{2}$ power, we have the requirement on $\bar{\theta}(z)$ that

$$\Gamma_d \int^z \frac{1}{\bar{\theta}(z)} dz \ \leq 1.0 \tag{3.6}$$

This places a restriction on the choice of domain height for a given H_θ. For typical atmospheric values of $H_\theta = 1000k^{-1}$ and $\Gamma_d = 3.3$, with $k = 0.1\text{km}^{-1}$, an acceptable domain height is $z_{max} - z_{min} = 300k^{-1}$. This corresponds to about 30km, approximately the vertical extent of the stratosphere.

3.2.1 Discretization and Resolution

For both the anelastic gas and non-Boussinesq liquid, the simulations are spectral in the horizontal and use a second-order finite-difference scheme to perform vertical spatial derivatives. The upper and lower boundary conditions are free slip. However, the vertical domain is chosen to be large enough that the waves are of negligibly small amplitude at the boundaries over the duration of each simulation.

In the vertical the domain resolution is 1024 grid points, spanning $-150k^{-1} \leq z \leq 150k^{-1}$. In the horizontal, wavenumbers between 0 and $8k$ are resolved so that the equivalent horizontal resolution is $\lambda_x/8$ over a domain of length λ_x. The simulations were allowed to run from $t = 0$ with a timestep of $\Delta t = 0.025N^{-1}$. The timestep and the vertical resolution were determined to be sufficiently small using the Courant-Friedrichs-Levy (CFL) condition, which specifies that the timestep Δt must be small enough that the flow cannot advect a fluid parcel as far as one grid point, Δz, during time Δt. Doubling the resolution was found to have no significant qualitative or quantitative effect on the wave dynamics.

3.2.2 Initialization

The initial wavepacket is horizontally periodic but with a Gaussian amplitude envelope in the vertical, centered at $z = 0$, and with a normalized initial maximum amplitude of $\beta \equiv A_{\Psi_0}(k^2/\rho_0 N^2) = 0.015$ unless otherwise specified. We simulate wavepackets with vertical wavenumber, m, chosen to be either $-0.4k$, $-0.7k$ or $-1.4k$. This range of vertical wavenumbers encompasses nearly hydrostatic waves, for which $\omega \ll N$, as well as non-hydrostatic waves for which ω is moderately smaller than N. These limits correspond to large and small ratios of $|m/k|$, respectively. The vertical extent of the wavepacket is $\sigma = 10k^{-1}$, corresponding to the perturbation parameter $\epsilon = 0.1$. Doubling the vertical

extent of the wavepacket (hence, halving ϵ) did not have a significant qualitative effect on the dominant characteristics of the weakly nonlinear evolution of the wavepacket although, as expected from the Schrödinger equation, it did increase the time scale for the development of linear dispersion and nonlinear effects.

For the purposes of initialization, we assume that the wavepacket is of sufficiently small amplitude and sufficiently broad width such that it is quasi-monochromatic with the dispersion relation given by (2.24). We assume the following form for the normalized mass-streamfunction:

$$\Psi(x,z,0) = A_\Psi(z,0)\exp(\imath kx + \imath mz - z/2H_\theta) + c.c. \tag{3.7}$$

in which *c.c.* denotes the complex conjugate and $A_\Psi(z,0) = \beta\exp(-z^2/2\sigma^2)$ is the envelope at time $t = 0$.

The code is spectral in the horizontal, and so represents (3.7) in terms of the number of waves, n, in a horizontal domain of length L_x. Typically we only allow one horizontal wavelength to span L_x so that $kL_x = 1$. The mass-streamfunction is thus represented by

$$\Psi(n,z) = 2A_\Psi e^{(\imath mz - z/2H_\theta)}\delta(n - kL_x)$$

in which δ is the Kronecker-Delta function. The code returns a peak of height β at the dominant wavenumber k in Fourier space.

Given Ψ, the perturbation vorticity and potential temperature fields are initialized by way of equation (2.16) and the polarization relation for the potential temperature and mass-streamfunction: $A_{\theta_0} = \frac{\bar{\theta}}{\bar{\rho}}\frac{k}{H_\theta\omega}\beta$. We then compute the initial wave-induced mean flow using equation (2.32). The z-derivative of this flow is added to the initial background vorticity field. Subsequently, the wave-induced mean flow field $U(z,t)$ is determined by the time-development of the vorticity and mass-streamfunction fields. At any time, however, the in-

stantaneous value of the horizontally averaged horizontal flow can be compared with the wave-induced mean flow predicted by (2.32).

3.2.3 Advection and Advancement in Time

The details of the tri-diagonal matrix-inversion used by the code to calculate the mass-streamfunction field from the vorticity field are provided in Appendix B. Once we have acquired the correct values for the mass-streamfunction, the code computes the horizontal and vertical velocity fields and, from these, evaluates the advective terms in the material derivative. This is done using fast Fourier transforms to convert the horizontal spectral fields to real fields, which are then multiplied together and inverse transformed.

The equations are advanced in time using the 'leap-frog' method, in which the vorticity and the potential temperature fields are advanced in time by

$$\zeta_{t+1} = \zeta_t + \frac{D\zeta}{Dt}_{t+1/2} dt,$$

and

$$\theta_{t+1} = \theta_t + \frac{D\theta}{Dt}_{t+1/2} dt.$$

This approach is necessary because, as we see in the governing equations, $D\zeta/Dt$ will depend on the potential temperature field θ, and $D\theta/Dt$ will depend on the mass-streamfunction, which is calculated from the vorticity field ζ. For computational stability, the advection terms are calculated using fields at centered timesteps while the dissipation terms are calculated using fields at a half timestep earlier. Every 20 timesteps, there is an Euler backstep in which the fields from the current and from the previous timestep are averaged in order to minimize numerical "splitting" errors.

3.3 Fully Nonlinear Non-Boussinesq Code

The fully nonlinear non-Boussinesq numerical simulation solves the following non-dimensional coupled equations for the fluctuation density, $\rho(x,z,t)$, and the total 'mass-weighted' vorticity, $\eta_T(x,z,t) \equiv \nabla \times (\bar{\rho}\vec{u}_T)$:

$$\frac{D\eta_T}{Dt} = \frac{\partial \rho}{\partial x} + w\frac{L}{H_\rho}\frac{d\bar{\rho}}{dz}\zeta_T + wu_T\left(\frac{L}{H_\rho}\right)^2\frac{d^2\bar{\rho}}{dz^2} + \frac{1}{\mathrm{Re}}\nabla^2\zeta, \tag{3.8}$$

and

$$\frac{D\rho}{Dt} = -w\frac{d\bar{\rho}}{dz} + \frac{1}{\mathrm{RePr}}\nabla^2\rho, \tag{3.9}$$

where $\zeta_T = \nabla \times \vec{u}_T = -\nabla^2\psi_T$ is the spanwise vorticity field. Equation (3.8) is derived by taking the curl of equation (2.2), and casting the result in terms of η_T for numerical convenience. Explicitly in terms of ψ_T, the mass-weighted vorticity is

$$\eta_T = -\bar{\rho}\nabla^2\psi_T - \frac{d\bar{\rho}}{dz}\frac{\partial \psi_T}{\partial z}. \tag{3.10}$$

As with the anelastic equations, the Prandtl number is set to be $\mathrm{Pr} \equiv \nu/\kappa = 1$, the Reynolds number is set to be $\mathrm{Re} \equiv \frac{\nu k^2}{N} = 10000$, and the bulk Richardson number is $J = 1$.

The initial Gaussian wavepackets take the form of (2.35) with $A_\xi(z,0) = \alpha \exp(-z^2/2\sigma^2)$ in which the initial maximum vertical displacement amplitude is $\alpha \equiv A_{\xi_0}k = 0.07$ unless otherwise indicated. The initial wave-induced mean flow is calculated from (2.39). The vertical displacement field is given approximately in terms of ρ using (2.50), with the condition $|\rho/\bar{\rho}| \ll 1$ continually being verified numerically at each timestep during the code's operation.

Note that in the fully nonlinear anelastic code no such condition appears because the vertical displacement is related to the potential temperature rather than the density:

$$\theta \approx -\frac{d\bar{\theta}}{dz}\xi. \tag{3.11}$$

Given $H_\theta \gg H_\rho$, the background potential temperature varies much more slowly than the background density, so that equation (3.11) will be valid over the width of the wavepacket.

Chapter 4

Results

A wave is modulationally unstable (Whitham, 1974) if $\omega_{mm}\omega_2 < 0$, where ω_{mm} denotes the second derivative of frequency with respect to the vertical wavenumber, and ω_2 is the coefficient of the $-\imath|A|^2A$ term in the nonlinear Schrödinger equations. In both (2.46) and (2.54), this is

$$\omega_2 = \frac{kU}{|A|^2} = \frac{1}{2}N^2\frac{k^2}{\omega_0}. \tag{4.1}$$

Because $\omega_2 > 0$ for internal gravity waves, modulational stability is determined by the sign of ω_{mm}. This term is negative if $|m| < 2^{-1/2}\left(k^2 + \frac{1}{4H_\rho^2}\right)^{1/2}$, and is positive otherwise. The critical point between modulational stability and instability occurs for waves with fixed k moving at the fastest vertical group velocity. For the density scale heights considered here, for which $kH_\rho \gg 1$, this corresponds to $|m/k| \simeq 2^{-1/2} \approx 0.71$.

4.1 Fully Nonlinear Evolution: Anelastic Gas

We begin by considering the results from the fully nonlinear simulations of an internal gravity wavepacket in an anelastic gas, using parameters similar to those in the atmosphere. The domain size corresponds to a 30km height of the atmosphere, and the horizontal extent of the domain contains one horizontal wavelength of the wavepacket with $\lambda_x \approx 628$m. The density scale height is $H_\rho = 10\text{km} \approx 15.9\lambda_x$ and the potential temperature scale height

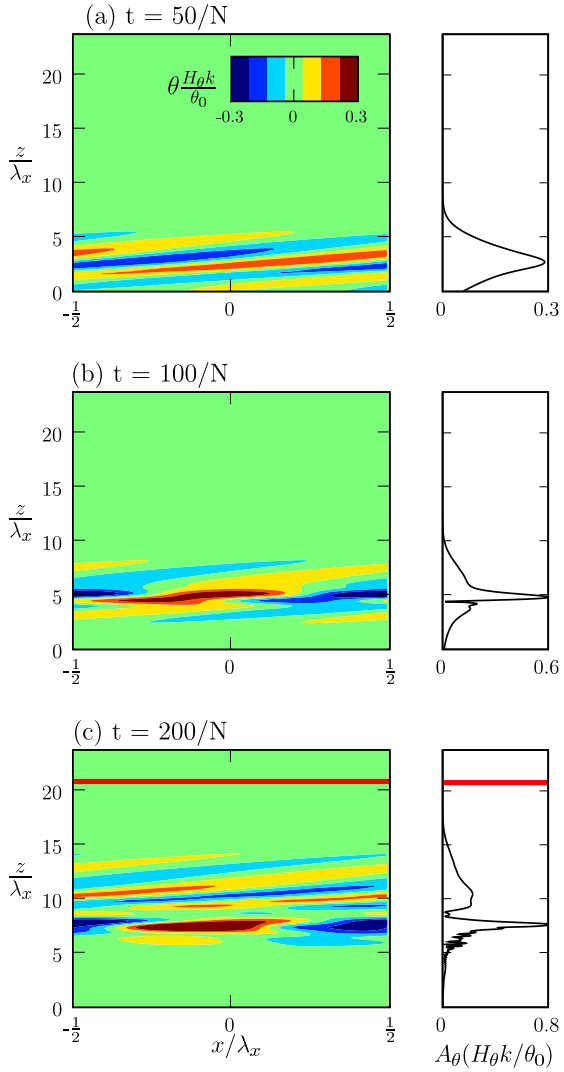

Figure 4.1: Left-hand panels show contour plots of the normalized potential temperature field, $\theta(x,z,t)/\frac{\theta_0}{H_\theta k}$, and right-hand panels show the corresponding normalized wavepacket amplitude envelope, $|A_\theta|\frac{H_\theta k}{\theta_0}$, from fully nonlinear simulations with $H_\rho = 15.9\lambda_x$, $H_\theta = 159\lambda_x$, $\beta = 0.015$ and $m = -0.4k$. The wavepacket evolution is shown for (a) $t = 50N^{-1}$, (b) $t = 100N^{-1}$, and (c) $t = 200N^{-1}$. The horizontal red line indicates the breaking level predicted by linear theory.

is $H_\theta = 100\text{km} \approx 159\lambda_x$. The initial maximum amplitude of the normalized mass-streamfunction of the wavepacket is $\beta = 0.015$, which corresponds to an initial maximum vertical displacement of about 13m, or roughly 2% of the horizontal wavelength. This amplitude is small enough that the wavepacket should obey linear theory at early times, following which the development of weakly nonlinear effects should be observed.

Figure 4.1 shows the evolution of a non-hydrostatic wavepacket, initially centered at $z = 0$, with a Gaussian envelope of width $\sigma = 10k^{-1}$ and a vertical wavenumber of $m = -0.4k$. The evolution is shown at early, late and very late times during the wavepacket's development. The left-hand panels show contour plots of the normalized potential temperature field, $\theta(x, z, t)(H_\theta k/\theta_0)$, which is related to the vertical displacement via $\theta \approx -(d\bar{\theta}/dz)\xi$, and the right-hand panels give the corresponding shape of the wavepacket envelope, $\|A_\theta\|(H_\theta k/\theta_0)$. The wavepacket evolution is shown for (a) $t = 50N^{-1}$, (b) $t = 100N^{-1}$, and (c) $t = 200N^{-1}$. The red horizontal line indicates the level at which linear theory predicts the wave should overturn, as detailed in Appendix C.

Figure 4.1a shows the wavepacket at $t = 50N^{-1}$, early on in its evolution. There is some evidence of weak nonlinearity in the narrowing of the amplitude envelope and in the increase in the maximum amplitude to $\|A_\theta\| = 0.30\theta_0/H_\theta k$, which is slightly larger than $\|A_\theta\| = 0.27\theta_0/H_\theta k$, the value predicted from linear theory when accounting only for anelastic growth.

In Figure 4.1b, we see the wavepacket at a later time, $t = 100N^{-1}$, when weakly nonlinear effects have significantly changed its shape. The amplitude envelope is narrower and more sharply peaked. The amplitude $\|A_\theta\| = 0.60\theta_0/H_\theta k$ is substantially larger than the linear theory prediction of $0.33\theta_0/H_\theta k$. This is consistent with the development of modulational instability. We also see that the wavepacket envelope has lost its vertical symmetry.

Figure 4.1c shows the wavepacket at $t = 200N^{-1}$, close to overturning. Due to the effect of modulational instability, the wavepacket has continued to narrow and the amplitude has increased to $\|A_\theta\| = 0.84\theta_0/H_\theta k$, over 50% larger than the linear theory prediction of $0.52\theta_0/H_\theta k$. Due to the weakly nonlinear dynamics of the wave, we see that it overturns at a much lower level than expected from linear theory. Wave breaking at $z = 8.0\lambda_x$ is 60% lower than the predicted breaking level of $20.8\lambda_x$.

Figure 4.2 shows the potential temperature field and corresponding amplitude envelope during the early, late and very late stages of the evolution of a wavepacket with $m = -0.7k$. Such a wavepacket is expected to be on the marginal boundary between modulational stability and instability. It corresponds to waves travelling at close to the fastest initial vertical group velocity $c_{gz} = 0.38Nk^{-1}$.

At early times, $t = 50N^{-1}$, shown in Figure 4.2a, the wavepacket is evolving as expected from linear theory. In Figure 4.2b, weakly nonlinear dynamics are apparent, with the wavepacket envelope dividing into two peaks. The amplitude is $\|A_\theta\| = 0.51\theta_0/H_\theta k$, about 20% larger than the linear theory prediction of $0.41\theta_0/H_\theta k$.

Figure 4.2c shows the wavepacket at $t = 200N^{-1}$, close to the point of wavebreaking, which occurs at a height of $z = 7.3\lambda_x$. Because it propagates at the fastest initial vertical group velocity, it overturns more quickly than wavepackets with other vertical wavenumbers. The amplitude envelope has divided into a series of individual peaks, with a maximum amplitude of $\|A_\theta\| = 0.70\theta_0/H_\theta k$, about 5% larger than the value predicted by linear theory, $0.67\theta_0/H_\theta k$. So we see that the amplitude is consistently larger than expected and varies due to the presence of multiple peaks. We also see that the wavepacket breaks far below the overturning level given by linear theory, which is indicated in the figure by the thick red line at $z = 19.4\lambda_x$. The relative increase in ampli-

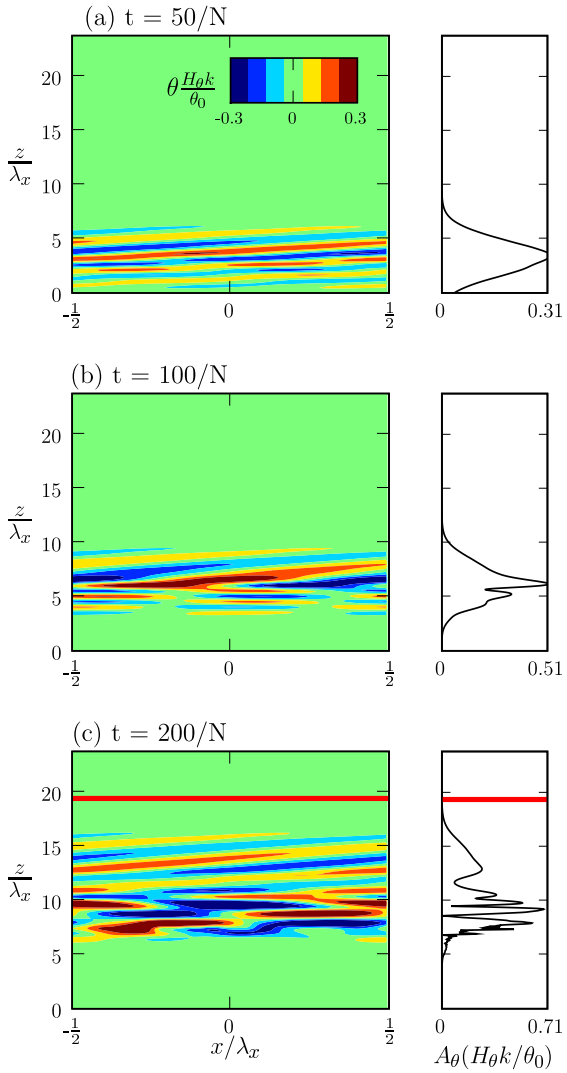

Figure 4.2: As in Figure 4.1 but with $m = -0.7k$. The value of β is 0.015. The wavepacket evolution is shown for (a) $t = 50N^{-1}$, (b) $t = 100N^{-1}$, and (c) $t = 200N^{-1}$. The breaking level predicted by linear theory is indicated by the red line, and is moderately lower in this simulation than for $m = -0.4k$.

tude suggests modulational instability. However, the development of multiple distinct peaks differs from the structure observed in the $m = -0.4k$ case.

Figure 4.3 shows the evolution of a more hydrostatic wavepacket with $m = -1.4k$. It is expected to be modulationally stable, and so one might expect propagation beyond the overturning level predicted by linear theory due to the slower rate of amplitude growth. What is observed is qualitatively different. At early times, shown in Figure 4.3a, the wavepacket envelope begins to broaden, while the amplitude has not changed from its initial value of $\|A_\theta\| = 0.35\theta_0/H_\theta k$. Linear theory predicts an increase in amplitude to $0.41\theta_0/H_\theta k$. This is characteristic of modulational stability. Figure 4.3b shows the wavepacket at a later time during its development at $t = 100N^{-1}$. The amplitude envelope has continued to broaden, but does so asymmetrically. The peak amplitude is around 20% lower than predicted by linear theory.

Linear theory predicts wave overturning at $z = 15.3\lambda_x$. Because this wavepacket is modulationally stable we might expect it to break above this level, but find that it breaks at $z = 9.6\lambda_x$, 37% lower. The reason for this low breaking level is the development of many distinct peaks in the wavepacket envelope as seen in Figure 4.3c, similar to what was observed for $m = -0.7k$. The amplitude of these peaks has grown rapidly, to a maximum value of $\|A_\theta\| = 0.79\theta_0/H_\theta k$, 25% larger than the amplitude predicted by linear theory.

4.1.1 Anelastic Gas: Wave-Induced Mean Flow Field

We now consider the evolution of the wave-induced mean flow associated with wavepackets of different initial amplitudes and vertical wavenumbers. The wave-induced mean flow field U is calculated from (2.32) at each time step. Because $U \propto \|A_\Psi\|^2$ the evolution of the wave-induced mean flow field also reflects the evolution of the wavepacket amplitude envelope.

As a control case, we first consider a wavepacket of very small amplitude,

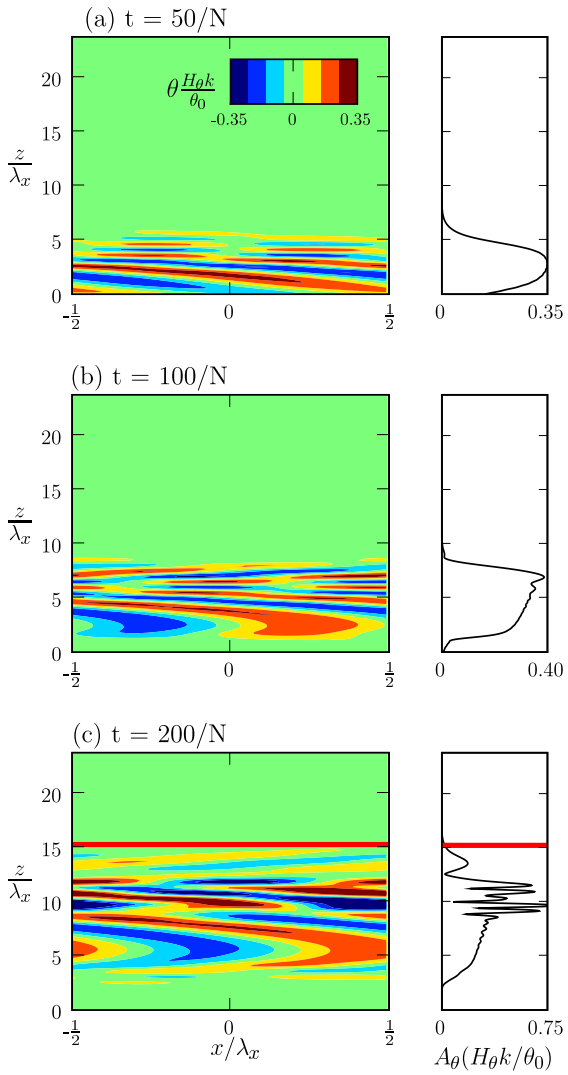

Figure 4.3: As in Figure 4.1, but with $m = -1.4k$. The wavepacket evolution is shown for (a) $t = 50N^{-1}$, (b) $t = 100N^{-1}$, and (c) $t = 200N^{-1}$. The breaking level predicted by linear theory is at $z \approx 15\lambda_x$.

$\beta = 0.001$, shown in Figure 4.4. Here $H_\theta = 159\lambda_x$ and $H_\rho = 15.9\lambda_x$. It is not expected that such a wave will exhibit weakly nonlinear effects until it has propagated a significant vertical distance and grown substantially in amplitude. As such, it provides a test as to whether or not the simulation correctly captures the evolution of a small-amplitude wavepacket as predicted by linear theory. The vertical wavenumbers considered are $m = -0.4k$, $m = -0.7k$, and $m = -1.4k$, which encompass non-hydrostatic and more hydrostatic waves. At early times, some small oscillations are visible in the time series. These are a result of the approximations used to initialize the wavepacket. They do not impact its evolution either qualitatively or quantitatively at later times.

The top row of plots, Figure 4.4a, b, and c, depicts contours of the normalized wave-induced mean flow field as the wavepacket propagates upward over time. Values for the normalization parameter U_{Max} are given in Table 3.2. It is clear that each wavepacket is experiencing exponential amplitude growth with height, as expected from linear theory.

The second row of plots, Figure 4.4d, e, and f, also show vertical time series of the wave-induced mean flow, however it is now given in a frame of reference moving upwards with the wavepacket at the initial value of the vertical group velocity, given in Table 3.1. The peak value of the wave-induced mean flow field remains at $Z = 0$ confirming that each wavepacket propagates at constant speed c_{gz}.

In the third row of plots, Figure 4.4g, h, and i, we have essentially removed the anelastic growth of the wave amplitude by multiplying $U(z,t)$ by the background density profile $\bar{\rho}(z)$. This result is then normalized by the maximum initial value of U at time $t = 0$, denoted U_0, and the vertical time series is plotted against Z to give: $\bar{\rho}(Z)U(Z,t)/\rho_0 U_0$.

For all three vertical wavenumbers shown in Figure 4.4, the relative amplitude remains nearly constant until at least $t = 150N^{-1}$, at which point

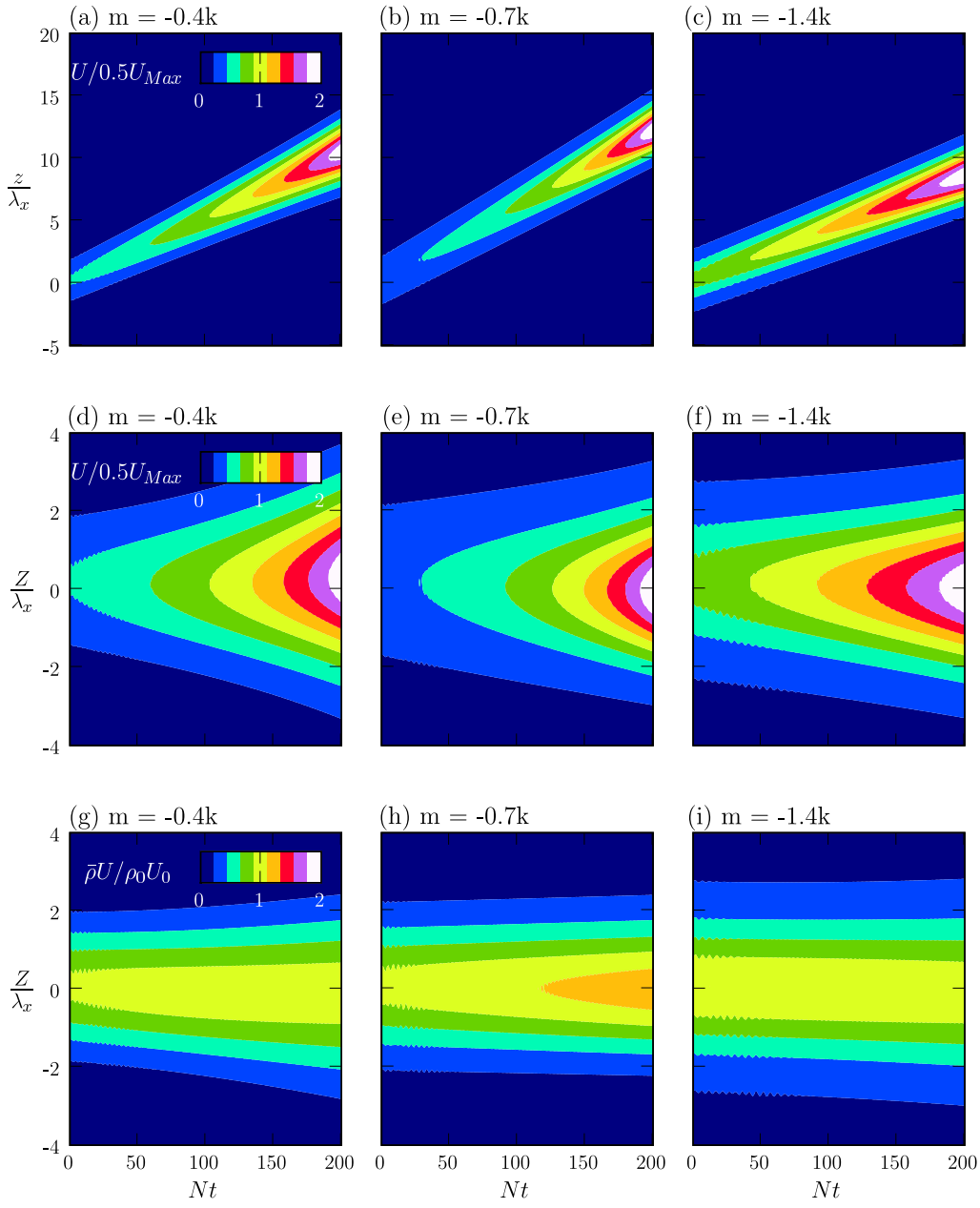

Figure 4.4: Time series of the normalized wave-induced mean flow field, from fully nonlinear simulations with $\beta = 0.001$ and $m = -0.4k$, $m = -0.7k$, or $m = -1.4k$. The top row, (a), (b), (c), gives the wave-induced mean flow normalized by half of its maximum value: $U(z,t)/0.5U_{\text{Max}}$. The second row, (d), (e), (f), shows the same thing, but in a frame of reference moving at the vertical group velocity of the wave so that $Z = z - c_{gz}t$, with Nt as the normalized time co-ordinate. The third row, (g), (h), (i), shows the wave-induced mean flow multiplied by the background density profile: $\bar{\rho}U/\rho_0U_0$.

there is a slight increase in the amplitude of the $m = -0.7k$ wavepacket. This occurs because it moves vertically most rapidly, resulting in more rapid amplitude growth, and thus an earlier onset of weakly nonlinear effects. Prior to this time, there is some slight broadening in the amplitude envelopes of the wavepackets, caused by linear dispersion.

We will now consider the wave-induced mean flow for wavepackets with parameters identical to those for the simulations shown in Figures 4.1, 4.2, and 4.3. Figure 4.5 shows vertical time series for three vertical wavenumbers; $m = -0.4k$, shown in the first column of plots, $m = -0.7k$, shown in the second column, and $m = -1.4k$, shown in the third column. Each row of plots contains the same fields as in Figure 4.4, but computed from simulations with a larger initial wavepacket amplitude.

The early evolution of each wavepacket obeys linear theory, as with the small amplitude case shown in Figure 4.4. However, weakly nonlinear dynamics develop quite rapidly after $t \approx 50N^{-1}$. For the non-hydrostatic wavepacket, $m = -0.4k$, the amplitude envelope narrows and the relative amplitude increases rapidly due to modulational instability. Also clearly visible is a decrease in the vertical group velocity of the wavepacket from $c_{gz} = 0.32Nk^{-1}$ to $c_{gz} = 0.24Nk^{-1}$ and the development of asymmetry in the vertical structure of its envelope. At later times, the relative amplitude decreases somewhat, and then increases again. This repeating pattern is consistent with the modulational instability of the wavepacket being accompanied by Fermi-Pasta-Ulam recurrence.

For the wavepacket with $m = -0.7k$, we observe a number of interesting features. In Figure 4.5h, the wavepacket broadens slightly before narrowing and increasing in relative amplitude. Thus it first demonstrates features of modulational stability but then rapidly becomes unstable. Its evolution is strongly asymmetric, with the development of a number of distinct peaks that

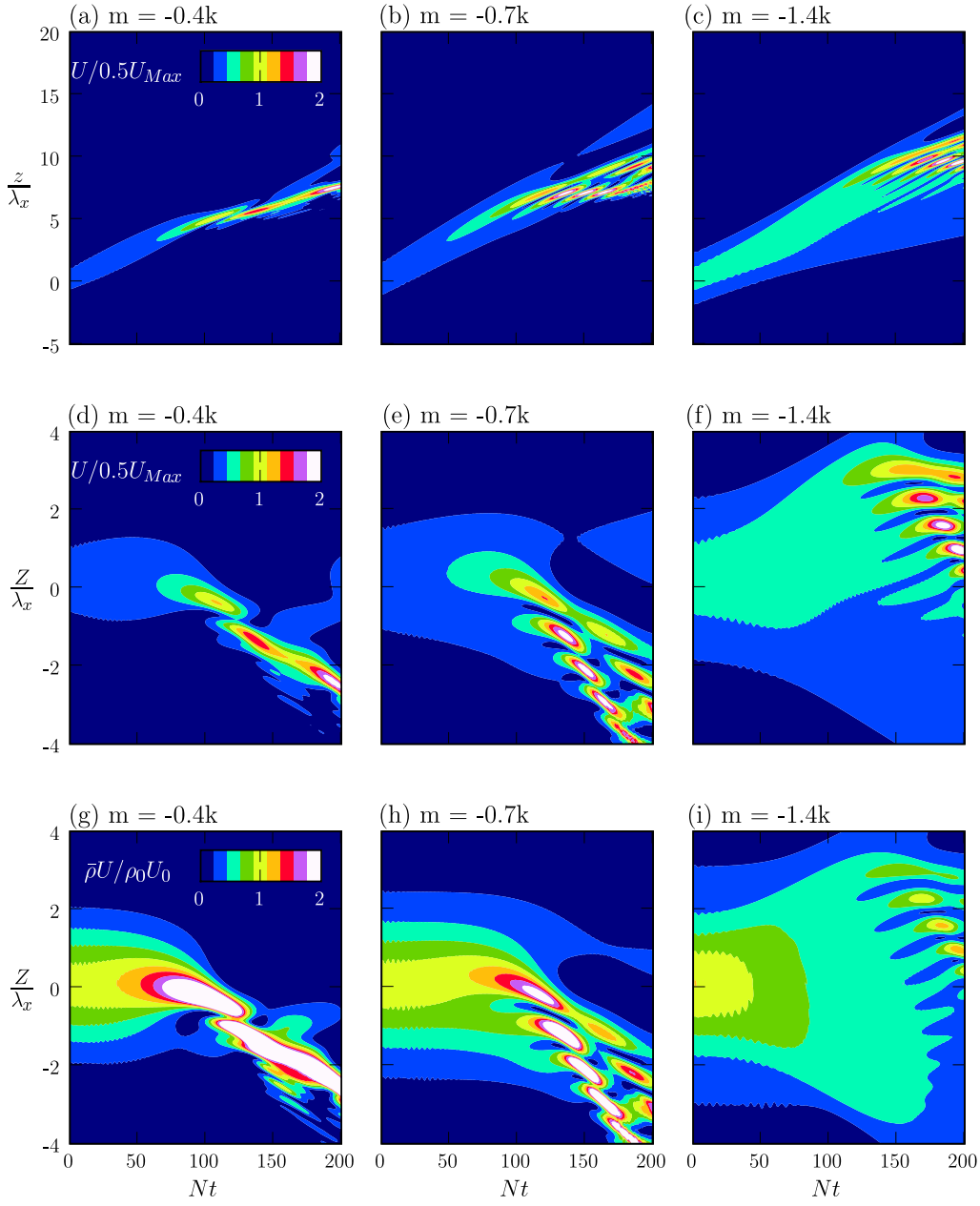

Figure 4.5: As in Figure 4.4, but with $\beta = 0.015$. U_{Max} is the maximum value of the wave-induced mean flow between $t = 0$ and $200N^{-1}$.

persist over many timesteps. The vertical group velocity of the peak with the highest amplitude is $c_{gz} = 0.29Nk^{-1}$, a decrease in velocity of almost 25%.

The evolution of the more hydrostatic wavepacket, $m = -1.4k$, shown in Figure 4.5i, is perhaps the most surprising. As weakly nonlinear dynamics begin to emerge, we observe the expected broadening and reduction in relative amplitude of the envelope due to modulational stability. However, at later times we see the development of a number of distinct peaks, similar to those seen in Figure 4.5h. These beautiful small-scale structures become so large in amplitude that they lead to wave-breaking at a much lower level than expected for a modulationally stable wavepacket. The beginnings of similar features were observed for Boussinesq wavepackets (Sutherland, 2006b) but were considered in that work to be evidence of parameteric subharmonic instability.

4.2 Weakly Nonlinear Evolution: Anelastic Gas

We now turn to the weakly nonlinear numerical simulations, which solve the anelastic Schrödinger equation (2.46). These are compared with the fully nonlinear results in Figure 4.6. The leftmost set of plots, Figure 4.6a, b, and c, are identical to Figure 4.5g, h, and i, for the fully nonlinear simulations. The integrated solutions of the weakly nonlinear equation are given in plots d, e, and f, on the right. The agreement between them is good at early times, both qualitatively and quantitatively. The non-hydrostatic wave shows the same narrowing and increase in amplitude characteristic of modulational instability, while the more hydrostatic wave broadens and the amplitude decreases due to modulational stability. The decreasing vertical group velocity is visible as well, as is the symmetry breaking for all three vertical wavenumbers. These dynamics are captured due to the inclusion of third order linear and nonlinear terms in the Schrödinger equation. They become significant when

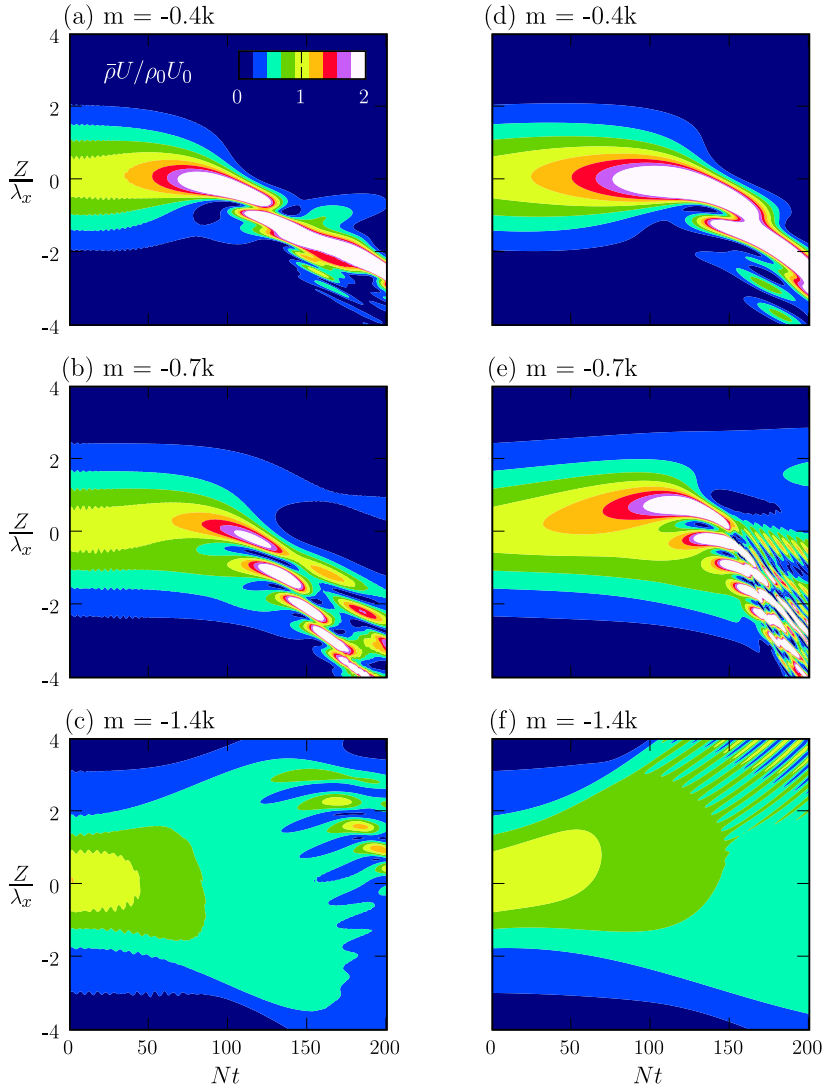

Figure 4.6: Contours of the normalized wave-induced mean flow field multiplied by the background density profile, $\bar{\rho}U/\rho_0 U_0$, with $\beta = 0.015$, $H_\rho = 15.9\lambda_x$, $H_\theta = 159\lambda_x$, and $m = -0.4k$, $m = -0.7k$, or $m = -1.4k$. The first column, (a), (b), (c), repeats the results of the fully nonlinear simulation from Figure 4.5(g), (h), and (i). The second column, (d), (e), (f), shows the same thing, but for solutions of the weakly nonlinear anelastic Schrödinger equation.

the wavepacket narrows and the amplitude increases such that the third and second order terms become comparable.

At late times, there is still good agreement for wavepackets with $m = -0.4k$ and $m = -0.7k$. However, the more hydrostatic wavepacket with $m = -1.4k$ separates unexpectedly into distinct peaks, which are only partially captured by the weakly nonlinear equation. While the Schrödinger equation does not accurately capture the width, location, or number of these peaks, the fact that it produces them at all indicates that they are not necessarily a result of parameteric subharmonic instability, which results from the wave-wave interactions that are filtered by the Schrödinger equation. At very late times during the development of the wavepackets, there are some other quantitative differences in the weakly nonlinear simulations, most notably that the amplitude of the wave-induced mean flow field is overly high. This is most evident for $m = -0.4k$ and $m = -0.7k$. However, the overall good agreement between the results of the fully and weakly nonlinear numerical simulations at early times indicates that the interaction of the wavepacket with the wave-induced mean flow is the primary mechanism for the initial development of weakly nonlinear effects, including modulational stability or instability.

4.2.1 Effect of Changing H_θ and H_ρ

In order to determine which parameters affect the stability of the wavepackets and thus influence the breaking heights, the evolution of wavepackets propagating in backgrounds with various values of H_ρ and H_θ were considered. Due to the definition of the background density profile, $\bar{\rho}(z)$, in terms of the background potential temperature field, $\bar{\theta}(z)$, as given by (2.12), it appears at first that the value of H_ρ should be dependent on the choice of H_θ. However, it is possible to specify both H_ρ and H_θ independently. Doing so sets the constant of integration in equation (2.12), which implicitly determines the values

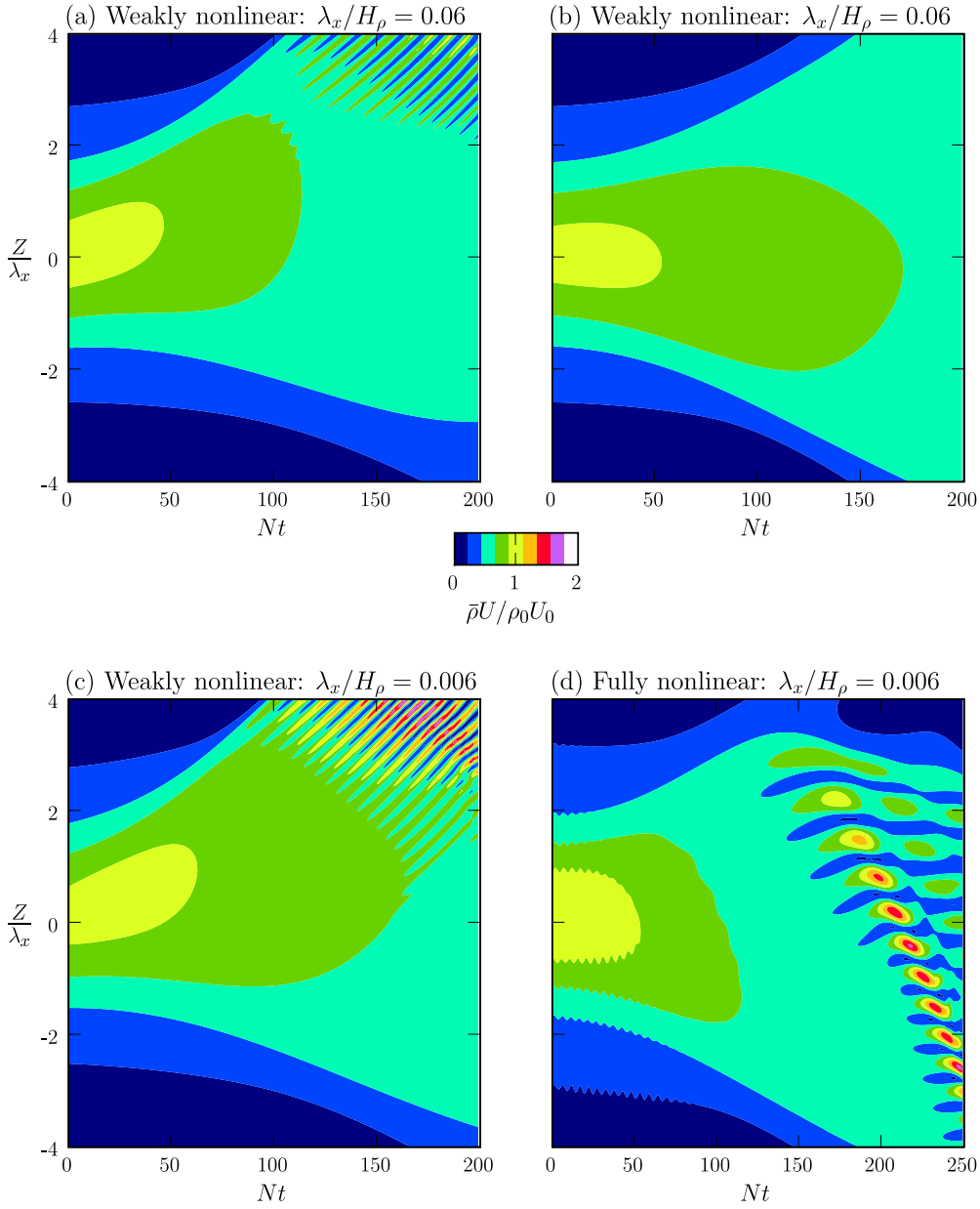

Figure 4.7: Anelastic fully and weakly nonlinear numerical simulations for the $\bar{\rho}U/\rho_0 U_0$ field of a wavepacket, with $\beta = 0.015$, $H_\theta = 159\lambda_x$ and $H_\rho = 15.9\lambda_x$ or $H_\rho = 159\lambda_x$, for vertical wavenumber $m = -1.4k$.

of the density and pressure at the reference level, ρ_0 and P_0. It is important to note that the approximation of $H_\rho(z)$ as a constant characteristic value, H_{ρ_0}, becomes less accurate as the ratio H_ρ/H_θ approaches a value of 1.0. In this thesis, the majority of the simulations use values for H_ρ and H_θ that are characteristic of the atmosphere, for which $H_\rho/H_\theta \approx 0.1$.

Changing the value of H_ρ did not significantly impact the wave dynamics nor did it substantially increase or decrease the timescale for the initial development of weakly nonlinear effects. While this may at first seem counterintuitive, it is most likely a result of the definition of $\bar{\rho}$ in terms of $\bar{\theta}$, as given by equation (2.12). For this reason, the background through which the wavepacket is travelling is more directly affected by the value of H_θ. However, H_ρ is seen to play a role in determining the relative amplitudes of the strongly nonlinear wavepackets at late times.

In order to illustrate more clearly what is causing the development of multiple distinct peaks in the late time evolution of anelastic wavepackets with $m = -1.4k$, Figure 4.7 shows results from the fully and the weakly nonlinear simulations. Here $\beta = 0.015$ and $H_\theta = 159\lambda_x$. In Figure 4.7a, we see the weakly nonlinear evolution of the hydrostatic wavepacket with $H_\rho = 15.9\lambda_x$. This replicates Figure 4.6f. In Figure 4.7b, we have removed the $(\partial_z U)A_\Psi$ term from the anelastic Schrödinger equation (2.46) whose coefficient is

$$\frac{1}{2}\frac{\omega^2}{N^2 k}\left(3m - \frac{\imath}{H_\rho}\right). \tag{4.2}$$

It is clear that the development of multiple distinct peaks has been sharply delayed. Thus we conclude that this weakly nonlinear effect results at least in part from third order nonlinear dispersion.

Figure 4.7c is identical to Figure 4.7a, except that H_ρ has been increased ten-fold to $159\lambda_x$, reducing the effect of the imaginary part of (4.2). As a result, the separation into peaks is more pronounced, with the peaks having

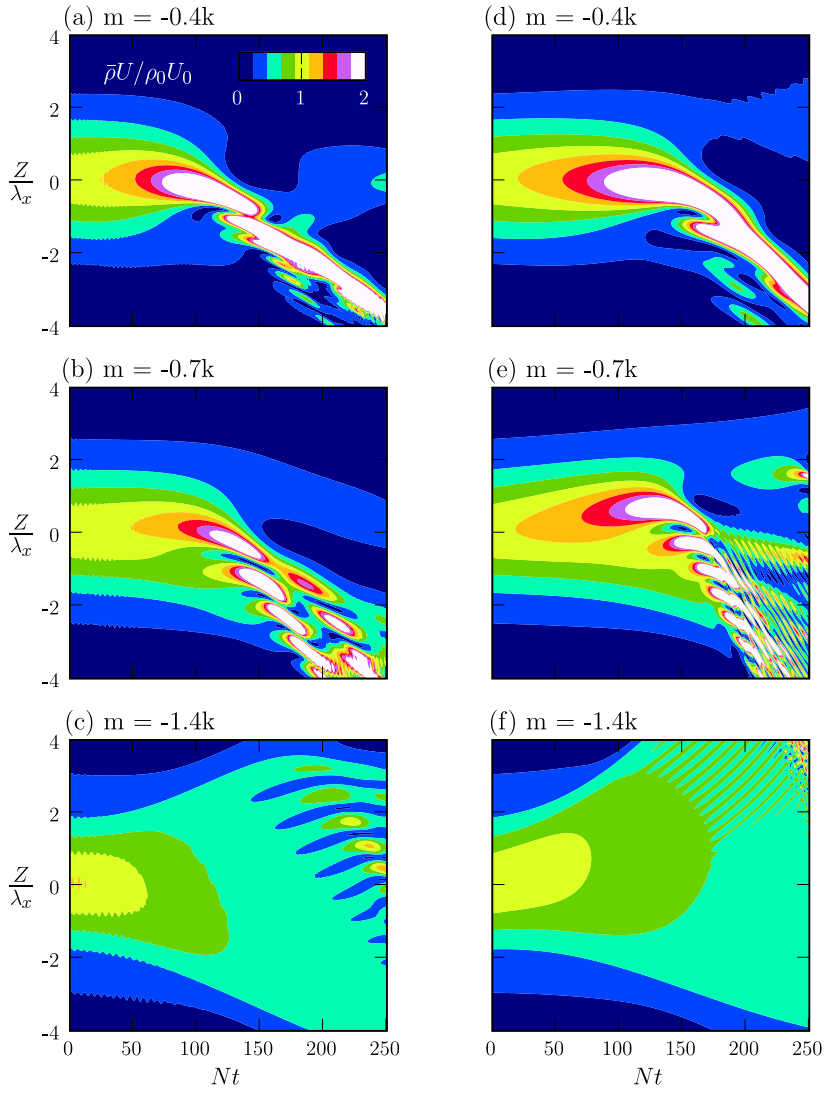

Figure 4.8: As in Fig. 4.6, but for potential temperature scale height $H_\theta = 318\lambda_x$. Wavenumbers shown are $m = -0.4k$, $m = -0.7k$, and $m = -1.4k$.

much larger amplitudes at late times. The corresponding plot from the fully nonlinear simulation with $H_\rho = 159\lambda_x$ is shown in Figure 4.7d. The amplitude of the peaks is comparable to the weakly nonlinear case, however the peaks themselves are qualitatively different from that case, and develop later during the wave evolution. It may be that the inclusion of fourth-order terms in the weakly nonlinear equation would capture this feature more accurately, however such an investigation is beyond the scope of this thesis. Despite the differences between the fully and weakly nonlinear simulations, we can conclude that the real part of the $(\partial_z U)A_\Psi$ term strongly affects the development of this weakly nonlinear feature for hydrostatic anelastic waves.

In Figure 4.8, the potential temperature scale height has been doubled from that used in Figure 4.6 to $H_\theta = 318\lambda_x$. All other parameters are unchanged. A larger value of the scale height is used since any value much below $H_\theta = 159\lambda_x$ is unphysical based on the criterion given by (3.6). Comparing the plots, we see that increasing H_θ increases the timescale for the onset of weakly nonlinear dynamics. Note that the time axis in this figure extends to $t = 250N^{-1}$, as compared to $t = 200N^{-1}$ in Figure 4.6. Other differences include a larger discrepancy between the maximum amplitudes predicted by the weakly nonlinear simulation at late times and the appearance of small scale structures in the weakly nonlinear plots after $t = 200N^{-1}$, most noticeably for $m = -0.7k$. The dominant features are otherwise similar to Figure 4.6.

4.3 Fully Nonlinear Non-Boussinesq Liquid

The results from the fully nonlinear numerical simulations of wavepackets in a non-Boussinesq liquid will be considered first. Figure 4.9 shows the evolution of the vertical displacement field of the waves at early, late, and very late times for a non-hydrostatic wavepacket with vertical wavenumber $m = -0.4k$. For each time, the left-hand panel contains a contour plot of the normalized

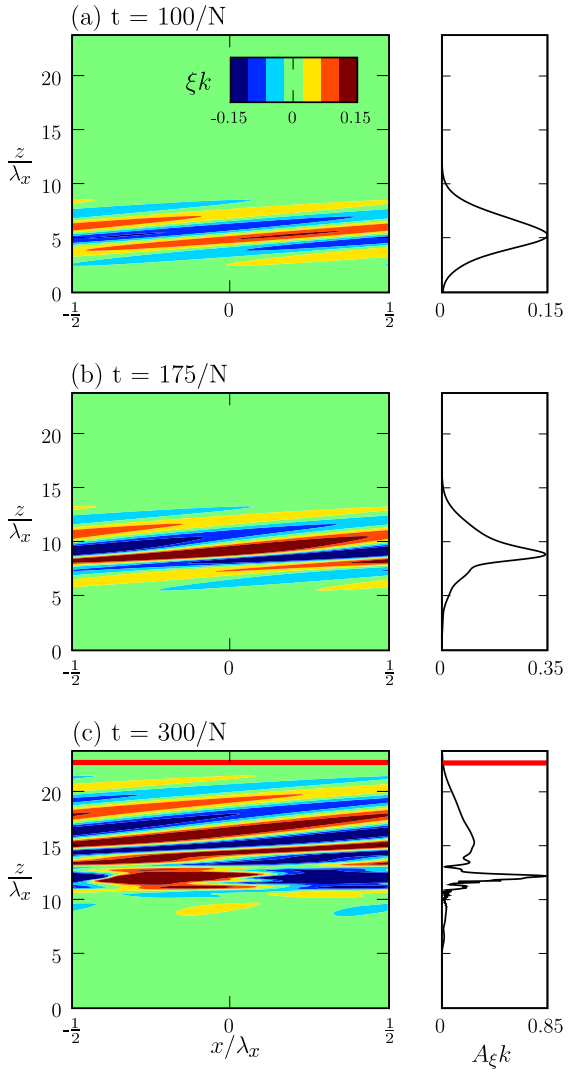

Figure 4.9: Left-hand panels show contour plots of the normalized vertical displacement field, $\xi(x, z, t)\, k$, and right-hand panels show the corresponding normalized wavepacket amplitude envelope, $|A_\xi|k$, from fully nonlinear simulations with $H_\rho = 3.2\lambda_x$, $\alpha = 0.07$ and $m = -0.4k$. The wavepacket evolution is shown for (a) $t = 100N^{-1}$, (b) $t = 175N^{-1}$, and (c) $t = 300N^{-1}$. The horizontal red line indicates the breaking level predicted by linear theory.

vertical displacement, ξk, and the right-hand panel shows the corresponding shape of the normalized vertical displacement amplitude envelope, $\|A_\xi\|k$. The packet is initially of small amplitude with $\alpha \equiv \|A_{\xi_0}\|k = 0.07$. The density scale height is $H_\rho = 3.2\lambda_x$.

Figure 4.9a shows the wavepacket at $t = 100N^{-1}$, before the onset of weakly nonlinear effects. The amplitude has increased as predicted by linear theory, growing exponentially with height to $\|A_\xi\| = 0.15k^{-1}$. In Figure 4.9b, we see the wavepacket during the onset of weakly nonlinear effects at $t = 175N^{-1}$. The wavepacket envelope has narrowed, become more sharply peaked and is no longer symmetrical. This is consistent with the wavepacket being modulationally unstable. The amplitude has increased to $\|A_\xi\| = 0.35k^{-1}$, substantially larger than the value predicted by linear theory, $0.28k^{-1}$.

Figure 4.9c shows the evolution of the wavepacket at very late times, $t = 300N^{-1}$, when the wave is beginning to overturn (the condition for overturning is given in Appendix C). Its maximum is now $\|A_\xi\| = 0.85k^{-1}$, about 10% larger than the value of $0.77k^{-1}$ predicted by linear theory. Due to these weakly nonlinear effects, the wavepacket begins to overturn at a lower height than predicted by linear theory, indicated in the figure by the thick red line at $z = 22.7\lambda_x$. Wave breaking actually occurs about 50% lower at $z = 11.4\lambda_x$.

Figure 4.10 is identical to Figure 4.9, except that it shows the vertical displacement field of a wavepacket on the marginal boundary between modulational stability and instability, with vertical wavenumber $m = -0.7k$. In Figure 4.10a, the amplitude of the envelope at $t = 100N^{-1}$ has increased as predicted by linear theory. In Figure 4.10b, weakly nonlinear effects have developed at $t = 175N^{-1}$: the amplitude envelope has narrowed and lost its vertical symmetry. However, the maximum amplitude shows an increase consistent with linear theory.

Figure 4.10c shows the wavepacket development at $t = 250N^{-1}$, which is

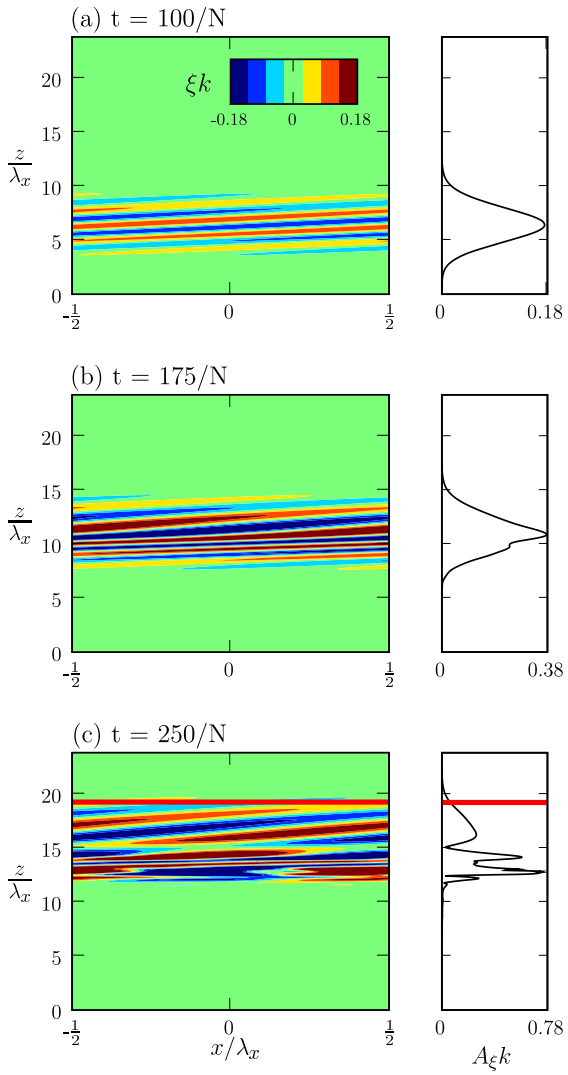

Figure 4.10: As in Fig. 4.9, but for $m = -0.7k$. Times shown are (a) $t = 100N^{-1}$, (b) $t = 175N^{-1}$, and (c) $t = 250N^{-1}$. The red line indicates the breaking level predicted by linear theory.

during wave breaking. Because this wavepacket propagates with the largest vertical group velocity, it reaches its breaking level most rapidly. The amplitude envelope has divided into several distinct peaks with a maximum of $\|A_\xi\| = 0.78k^{-1}$. This is close to the value given by linear theory, $\|A_\xi\| = 0.75k^{-1}$. The wavepacket first breaks at $z = 12.8\lambda_x$, much lower than the predicted height of $z = 19.2\lambda_x$ indicated by the red line. This is a decrease in breaking height of about 30%.

Figure 4.11 contains a more hydrostatic wavepacket with vertical wavenumber $m = -1.4k$, which is predicted to be modulationally stable. The wavepacket is shown at early times in Figure 4.11a, with $t = 100N^{-1}$. The amplitude of the wavepacket envelope is slightly lower than predicted by linear theory, with a value of $\|A_\xi\| = 0.13k^{-1}$ as compared to $0.14k^{-1}$. Figure 4.11b shows the modulationally stable wavepacket at a later time during its development, $t = 175N^{-1}$, at which point it has broadened significantly, and become slightly asymmetrical. The amplitude has increased to $\|A_\xi\| = 0.18k^{-1}$, which is much smaller than the value of $0.23k^{-1}$ predicted by linear theory.

Figure 4.11c shows the wavepacket at time $t = 325N^{-1}$. The wavepacket is not overturning. The maximum amplitude is $\|A_\xi\| = 0.46k^{-1}$, much smaller than the predicted value of $0.63k^{-1}$. In a fully nonlinear simulation with a larger vertical domain, wave breaking was seen to occur at a height of $z = 19.5\lambda_x$, almost 25% higher than the overturning level given by linear theory, $z = 14.8\lambda_x$. This increase in the height of the initial overturning event is the expected consequence of the modulational stability of the wavepacket. The amplitude envelope has lost its vertical symmetry with a large peak at the leading edge followed by several smaller peaks. This is similar to the distinct peaks observed for a wavepacket with $m = -1.4k$ in an anelastic gas, however the peaks do not increase significantly in amplitude prior to wave breaking.

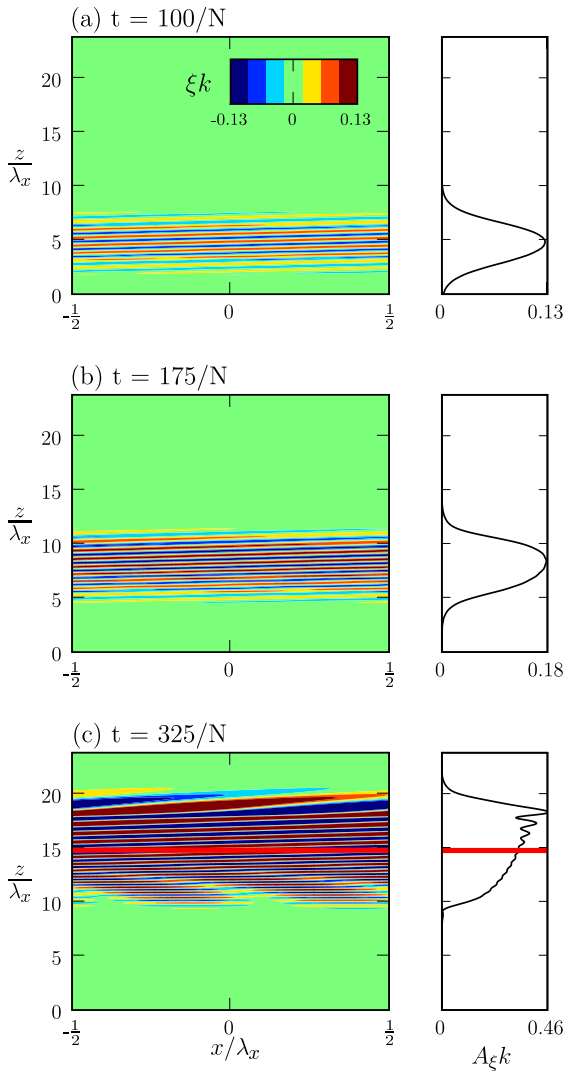

Figure 4.11: As in Fig. 4.9 and 4.10, but for $m = -1.4k$. Times shown are (a) $t = 100N^{-1}$, (b) $t = 175N^{-1}$, and (c) $t = 325N^{-1}$. The horizontal red line indicates the breaking level predicted by linear theory.

4.3.1 Non-Boussinesq Liquid: Wave-Induced Mean Flow

We now consider the wave-induced mean flow field from the fully nonlinear numerical simulations. We begin with a wavepacket of small initial amplitude, with $\alpha = 0.03$ and $H_\rho = 3.2\lambda_x$. The wave-induced mean flow is calculated from (2.39) at successive times. The wavepacket has been initialized with sufficiently small amplitude that we do not expect to see the development of weakly nonlinear effects until very late times in the wavepacket's evolution. Figure 4.12 shows time series of the normalized wave-induced mean flow field for vertical wavenumbers of $m = -0.4k$, $m = -0.7k$, and $m = -1.4k$. There are some small superimposed oscillations visible at early times that occur due to the approximations used to initialize the wavepacket but which have no effect upon the evolution of the wavepacket at later times.

The top row of three plots, Figure 4.12a, b, and c, gives the wave-induced mean flow normalized by half of its maximum value: $U(z,t)/0.5U_{\text{Max}}$. The exponential growth of the wavepacket amplitude with increasing height is clearly evident. In the second row, Figure 4.12d, e, and f, we have the same field, but shifted into a frame of reference moving at c_{gz}. Symmetry about $Z = 0$ confirms that the waves translate at the initial group velocity. The plots in the third row, Figure 4.12g, h, and i, show the wave-induced mean flow multiplied by the background density profile, $\bar{\rho}(Z)U(Z,t)/\rho_0 U_0$. Here U_0 is the maximum value of the wave-induced mean flow field at time $t = 0$. Multiplication by $\bar{\rho} \equiv \rho_0 \exp(-z/H_\rho)$ essentially removes the exponential growth associated with a non-Boussinesq wavepacket and serves to emphasize that the momentum associated with the wave-induced mean flow is conserved. The relative amplitude of each wavepacket remains constant, confirming exponential growth.

These wavepackets obey linear theory until at least $t \approx 100N^{-1}$, at which

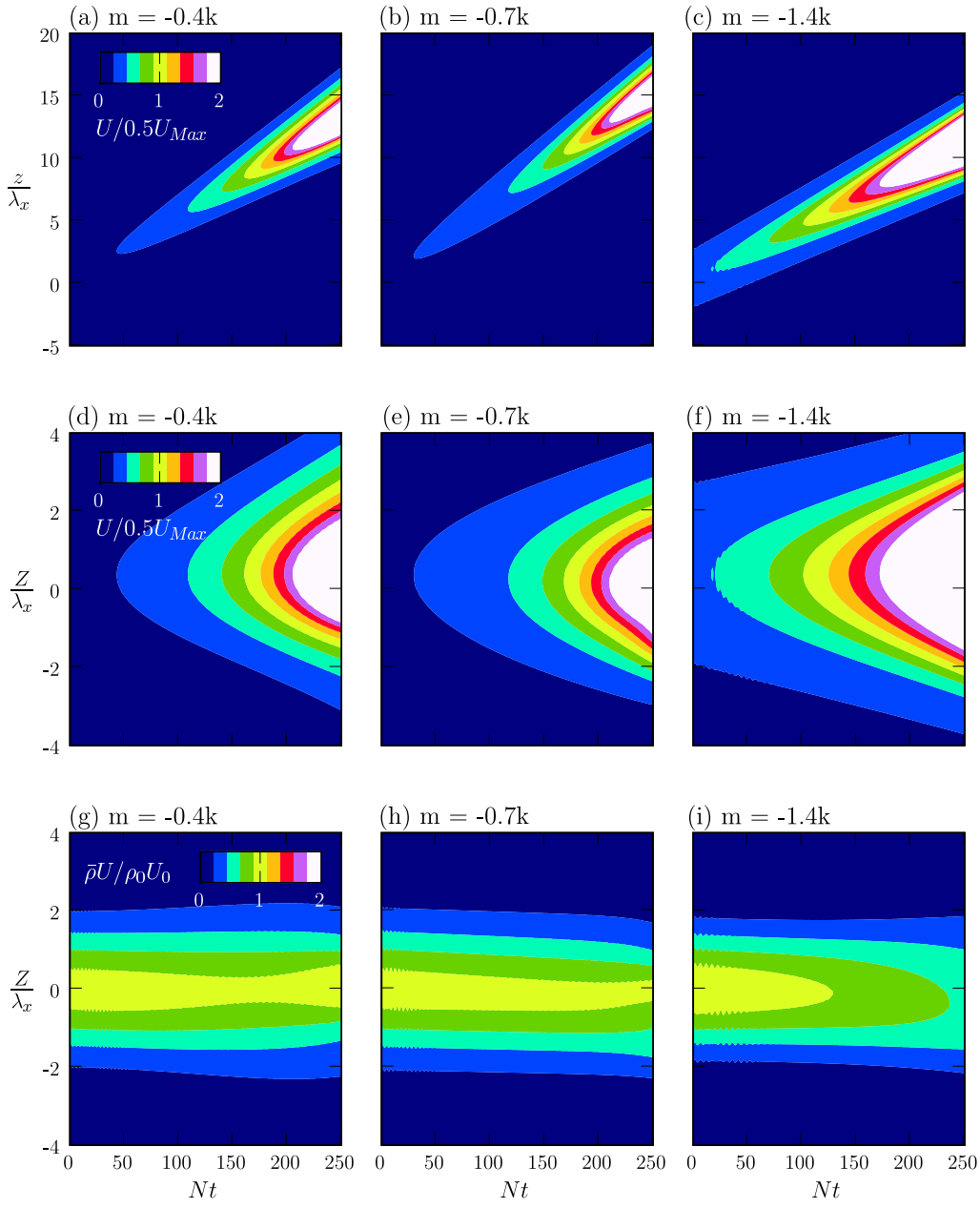

Figure 4.12: Time series of the normalized wave-induced mean flow field, from fully nonlinear simulations with $\alpha = 0.03$ and $m = -0.4k$, $m = -0.7k$, or $m = -1.4k$. The top row, (a), (b), (c), gives the wave-induced mean flow normalized by half of its maximum value: $U(z,t)/0.5U_{\text{Max}}$. The second row, (d), (e), (f), shows the same thing, but in a frame of reference moving at the vertical group velocity of the wave so that $Z = z - c_{gz}t$, with Nt as the normalized time co-ordinate. The third row, (g), (h), (i), shows the wave-induced mean flow multiplied by the background density profile: $\bar{\rho}(Z)U(Z,t)/\rho_0U_0$.

point weak nonlinearity becomes apparent. A slight decrease in the relative amplitude of the wavepacket is visible in all three plots as a result of linear dispersion. In Figure 4.12i, the relative amplitude decreases rapidly after $t = 100N^{-1}$, while Figure 4.12g shows a narrowing of the wavepacket at $t \approx 150N^{-1}$. Finally, in Figure 4.12h, there is some symmetry breaking evident after $t \approx 200N^{-1}$.

Figure 4.13 shows time series of the normalized wave-induced mean flow for a wavepacket initialized at amplitude $\alpha = 0.07$ and allowed to propagate upwards in a non-Boussinesq background with $H_\rho = 3.2\lambda_x$. The three columns of plots correspond to vertical wavenumbers of $m = -0.4k$, $-0.7k$ and $-1.4k$. The exponential increase in wave amplitude with height is immediately visible and dominates the wave evolution in Figure 4.13a, b, and c.

For each of the three wavenumbers presented, the evolution of the wavepacket shown in Figure 4.13 is qualitatively different. During the first part of each wavepacket's upward propagation, it moves at a near constant speed equal to the initial vertical group velocity and remains of small enough amplitude that it can be treated as being in the linear regime, as discussed for Figure 4.12. However, between times $t = 100N^{-1}$ and $150N^{-1}$ the influence of weakly nonlinear effects becomes apparent. For a non-hydrostatic wavepacket with vertical wavenumber of $m = -0.4k$, (Figure 4.13g), the envelope of the wave-induced mean flow field narrows while the relative amplitude increases significantly as a result of modulational instability. At late times, the vertical group velocity of the wave decreases from its initial value of $c_{gz} = 0.32Nk^{-1}$ to approximately $c_{gz} = 0.26Nk^{-1}$ and symmetry breaking is observed.

For a vertical wavenumber of $m = -1.4k$, (Figure 4.13i), the wave-induced mean flow profile broadens while the peak amplitude decreases due to dispersion. These weakly nonlinear effects were also seen to occur in Figure 4.11b and 4.11c, as a result of modulational stability. At late times, there is some

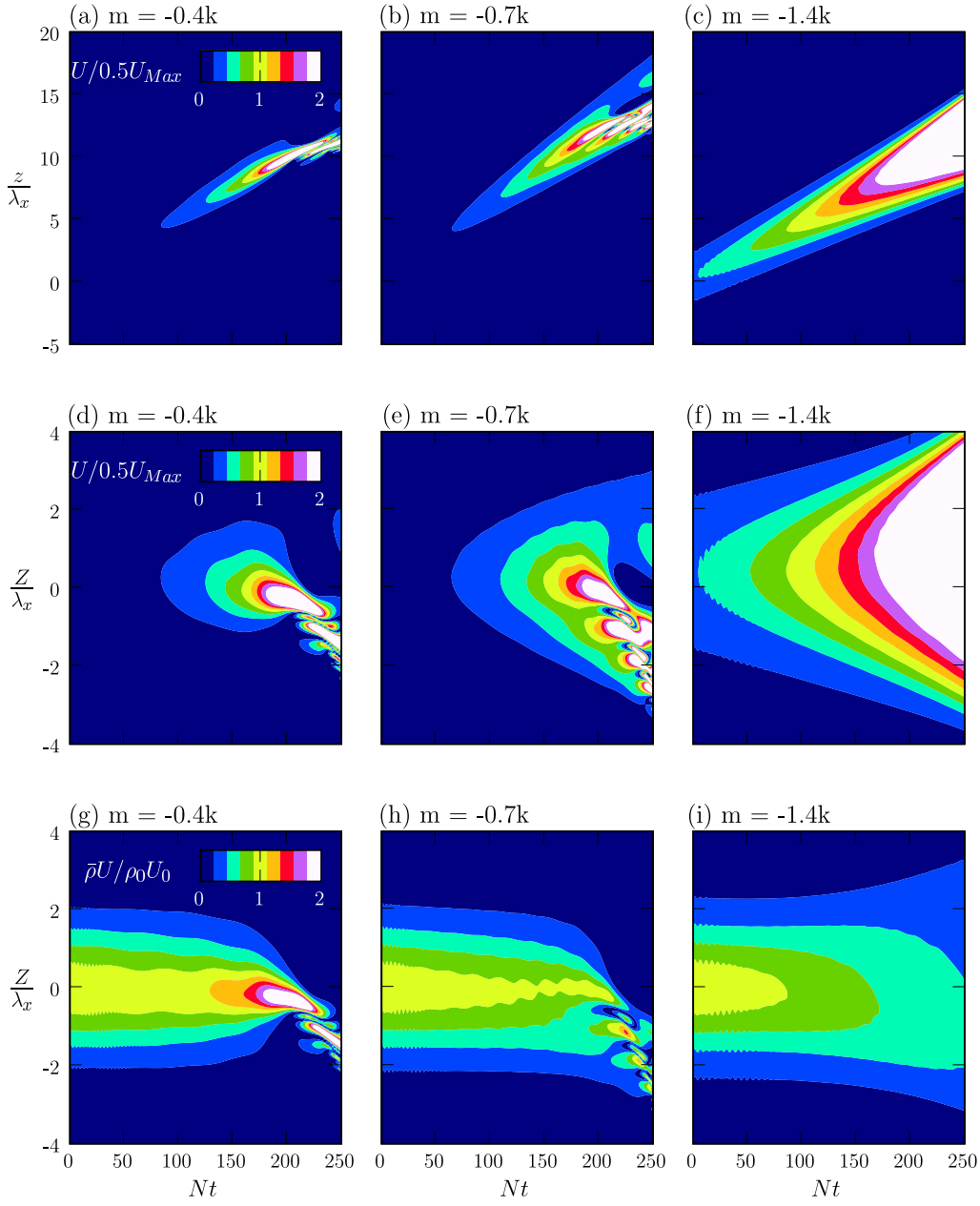

Figure 4.13: As in Figure 4.12, but with $\alpha = 0.07$. U_{Max} is the maximum value of the wave-induced mean flow between $t = 0$ and $250N^{-1}$.

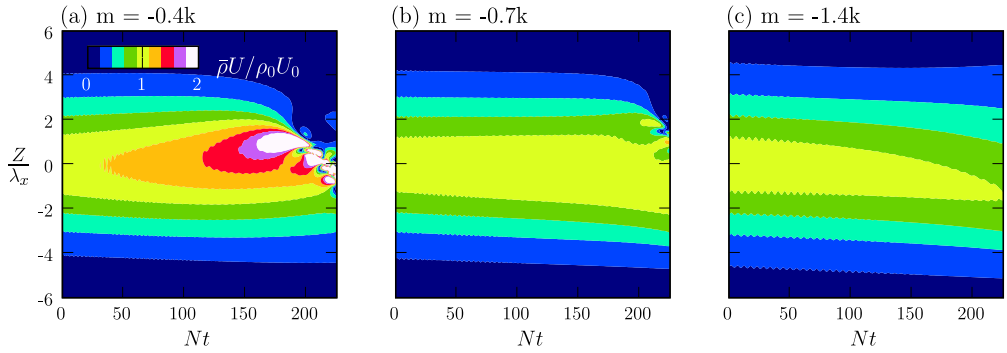

Figure 4.14: Results from fully nonlinear numerical simulations for the $\bar{\rho}U/\rho_0 U_0$ field of a wavepacket with $\sigma = 20k^{-1}$, $\alpha = 0.07$, and $H_\rho = 3.2\lambda_x$, for vertical wavenumbers $m = -0.4k$, $m = -0.7k$, and $m = -1.4k$.

slight symmetry breaking and little change in the group velocity. For a vertical wavenumber of $m = -0.7k$, Figure 4.13h shows the near-marginal case between modulational stability and instability. The wavepacket broadens slightly before narrowing and increasing in amplitude. At late times, the group velocity of the wavepacket decreases by an amount comparable with its initial vertical group velocity. Thus it demonstrates characteristics of both modulationally stable and unstable wavepackets.

4.3.2 Effect of Changing σ

Figure 4.14 shows the result of fully nonlinear simulations in which the width of the wavepacket has been doubled to $\sigma = 20k^{-1}$. The non-hydrostatic wavepacket displays modulational instability through a narrowed wavepacket envelope and increase in relative amplitude. The more hydrostatic wave is modulationally stable and shows a decrease in relative amplitude at late times, however it does not broaden significantly. As expected, increasing σ has lengthened the timescale for the development of weakly nonlinear effects. The same is true for the wavepacket of wavenumber $m = -0.7k$, which begins to show signs of symmetry breaking at $t = 200N^{-1}$. However, doubling the width of the wavepacket does not otherwise affect the weakly nonlinear dynamics.

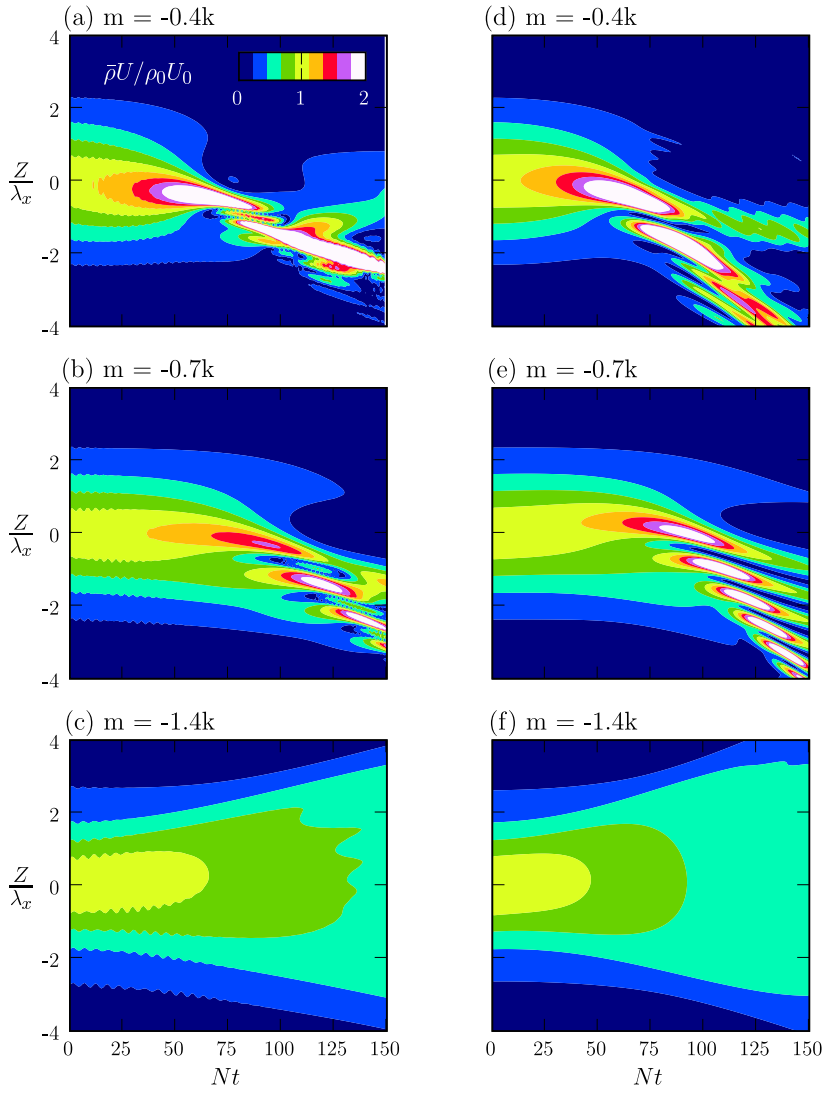

Figure 4.15: Comparison of fully nonlinear (left column) and weakly nonlinear (right column) numerical simulations for the $\bar{\rho}U/\rho_0 U_0 \approx U/U_0$ field of a wavepacket with $\alpha = 0.3$, and $H_\rho = 16\lambda_x$, for vertical wavenumbers $m = -0.4k$, $m = -0.7k$, and $m = -1.4k$. These are essentially large amplitude Boussinesq wavepackets.

4.4 Weakly Nonlinear Non-Boussinesq Liquid

While the evolution of non-Boussinesq wavepackets is qualitatively similar to that of large amplitude Boussinesq waves, it differs in some important and related respects. As a wavepacket propagates upwards through a non-Boussinesq fluid it grows in amplitude due to the decreasing background density, as demonstrated in Figure 4.12. This is not the case for waves initialized at small amplitude in a Boussinesq fluid, which decrease slightly in amplitude due to linear dispersion but remain otherwise unchanged. Thus, in order to observe the development of weakly nonlinear effects in a Boussinesq fluid, a wavepacket must be initially of large amplitude, an example of which is presented in Figure 4.15.

This figure considers wavepackets propagating in a fluid with a large density scale height $H_\rho = 16\lambda_x$, initialized at relatively large amplitude $\alpha = 0.3$. This mimics a Boussinesq fluid. Figure 4.15 reproduces the results of Sutherland (2006b) both qualitatively and quantitatively. Modulational stability and instability are clearly observable for the hydrostatic ($m = -1.4k$) and non-hydrostatic ($m = -0.4k$) wavepacket respectively, as is symmetry breaking due to the inclusion of third order linear and nonlinear terms in the Schrödinger equation. This confirms that both the fully and weakly nonlinear codes are functioning as expected, and emphasizes that the theory for non-Boussinesq waves in a liquid is equivalent to that for Boussinesq waves in the limit $H_\rho \to \infty$.

The results from integrating the solutions of the weakly nonlinear Schrödinger equation for a non-Boussinesq liquid are compared with the fully nonlinear results in Figure 4.16. As in Figure 4.13, $\alpha = 0.07$ and $H_\rho = 3.2\lambda_x$. Figure 4.16a, b, and c, repeat plots g, h, and i from Figure 4.13. Figure 4.16d, e, and f, show the solutions of the weakly nonlinear equation, which clearly captures the dominant qualitative and quantitative features of the weakly nonlinear

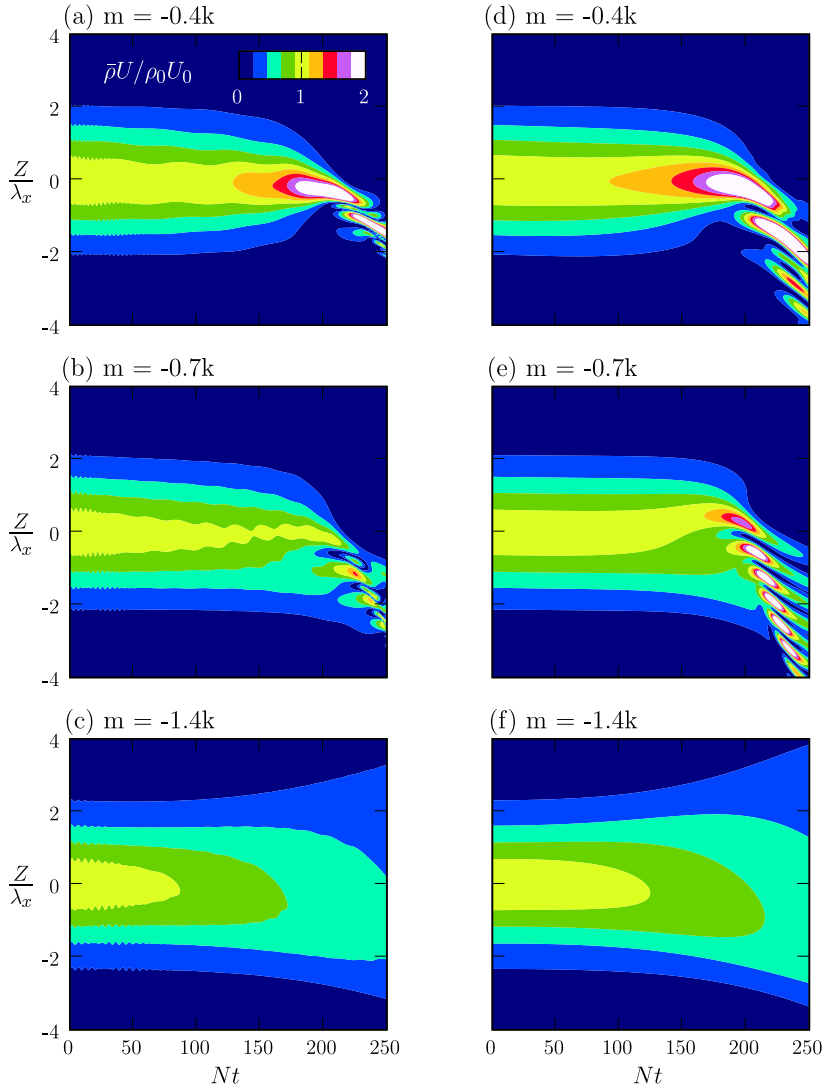

Figure 4.16: Contours of the normalized wave-induced mean flow field multiplied by the background density profile, $\bar{\rho}U/\rho_0 U_0$, with $\alpha = 0.07$, $H_\rho = 3.2\lambda_x$ and $m = -0.4k$, $m = -0.7k$, or $m = -1.4k$. The first column, (a), (b), (c), repeats the results of the fully nonlinear simulation from Figure 4.13(g), (h), and (i). The second column, (d), (e), (f), shows the same thing, but for solutions of the weakly nonlinear non-Boussinesq Schrödinger equation.

wavepacket evolution, for all three vertical wavenumbers. As with the fully nonlinear simulations, the non-hydrostatic wave (Figure 4.16d) narrows and increases in amplitude due to modulational instability. The more hydrostatic wave (Figure 4.16f) broadens and decreases in amplitude indicating that it is modulationally stable. The symmetry breaking and decrease in vertical group velocity is also captured. Due to the relatively small value of the density scale height, the fourth term in the weakly nonlinear equation, which captures effects unique to waves in a non-Boussinesq fluid, contributes non-negligibly to the nonlinear evolution of the wavepacket.

At very late times, discrepancies arise due to what was thought to be the appearance of parametric subharmonic instability in the fully nonlinear results. Such dynamics are not captured by the weakly nonlinear equation. However, based on the results for anelastic waves, these discrepancies are most likely the beginning of multiple distinct peaks caused at least in part by high-order dispersion. The non-Boussinesq wavepackets overturn prior to the full development of these features. Other discrepancies between the fully and weakly nonlinear simulations include the over-prediction of the wave-induced mean flow field by the weakly nonlinear equation at late times. These quantitative differences are visible for all three wavenumbers and are particularly clear in Figure 4.16e, which shows up to a 30% increase in amplitude over Figure 4.16b.

4.4.1 Effect of Changing H_ρ and α

Figure 4.17 compares the results of the fully and weakly nonlinear simulations for $\alpha = 0.07$ and $H_\rho = 1.6\lambda_x$. This 50% decrease in H_ρ compared to the value used for Figure 4.16 doubles the importance of the fourth term in the weakly nonlinear equation. Note that the time axis on this plot stops at $t = 150N^{-1}$, rather than $t = 250N^{-1}$ as in the previous figure. The onset of weakly nonlinear effects occurs between $t = 50N^{-1}$ and $t = 100N^{-1}$, slightly

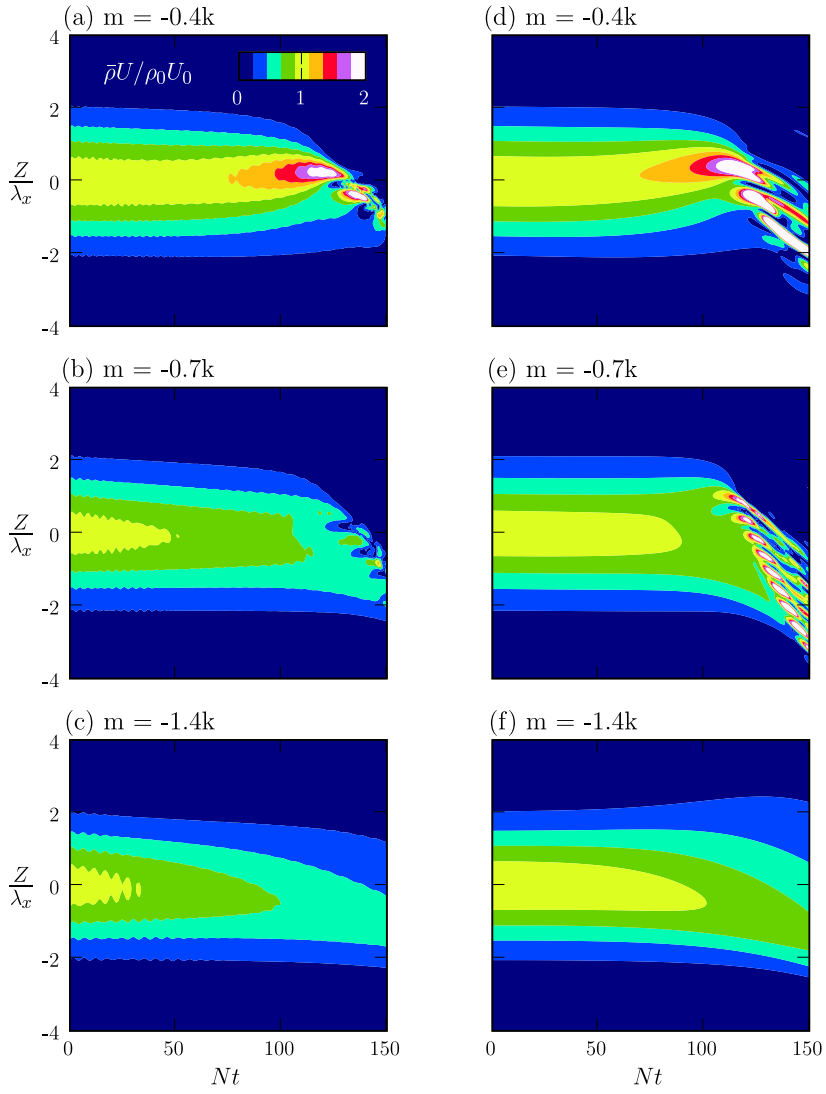

Figure 4.17: As in Fig. 4.16, but for density scale height $H_\rho = 1.6\lambda_x$. Wavenumbers shown are $m = -0.4k$, $m = -0.7k$, and $m = -1.4k$.

sooner than for $H_\rho = 3.2\lambda_x$. The subsequent weakly nonlinear evolution occurs on a more rapid timescale due to the enhanced amplitude growth associated with a smaller H_ρ. The appearance of modulational stability and instability is similar to Figure 4.16, and we see relatively good agreement between the fully and the weakly nonlinear simulations.

The largest discrepancy is the significant overestimation of the relative amplitudes in the weakly nonlinear case, visible in all three plots. We see increased symmetry breaking, particularly for $m = -0.4k$ and $m = -1.4k$. For $m = -0.7k$, we no longer observe the wavepacket narrowing and peaking prior to the onset of symmetry breaking, while the more hydrostatic wavepacket has broadened less rapidly. This is a result of the shorter timescale over which the weakly nonlinear effects caused by the third order terms in the Schrödinger equation develop.

In order to separate the effects of a decrease in density scale height from the effects of a larger initial wavepacket amplitude, Figure 4.18 compares the wave-induced mean flow from fully and weakly nonlinear simulations of waves with $\alpha = 0.2$ and $H_\rho = 3.2\lambda_x$. Note that the time axis on this plot ends at $t = 150N^{-1}$. In Figure 4.18 we see that the Schrödinger equation correctly estimating the relative amplitudes even at late times, an improvement over the $\alpha = 0.07$ case. We conclude that the weakly nonlinear equation is unable to capture nonlinear effects that cause a reduction in the relative wavepacket amplitude and that are more dominant in a more rapidly decreasing background density field. This is not surprising because the weakly nonlinear equation neglects wave-wave interactions. For physically reasonable values of the density scale height and initial wavepacket amplitude, however, this nonlinear effect plays a relatively minor role. Comparing Figure 4.18 to Figure 4.17 also reveals that a decrease in H_ρ causes decreased broadening of the $m = -1.4k$ wavepacket and inhibits the narrowing and peaking of

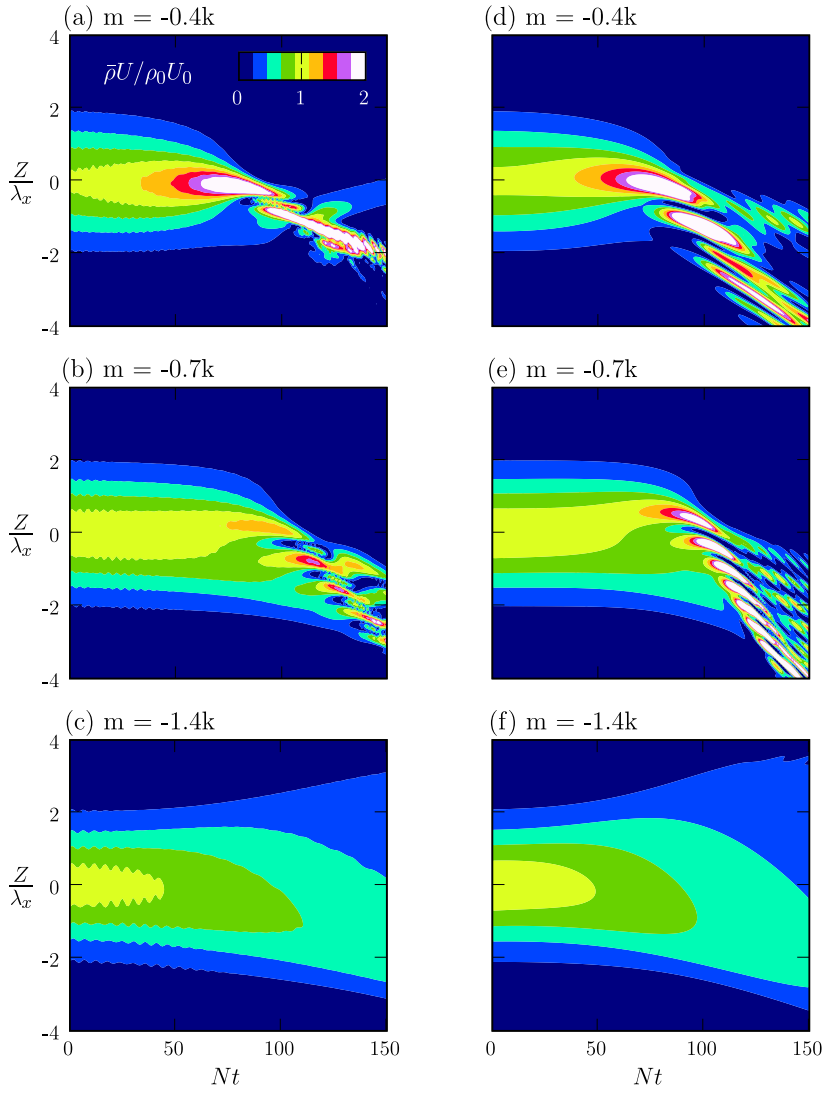

Figure 4.18: As in Fig. 4.16, but for initial wavepacket amplitude $\alpha = 0.2$. Wavenumbers shown are $m = -0.4k$, $m = -0.7k$, and $m = -1.4k$.

the $m = -0.7k$ wavepacket. The symmetry breaking for a wavepacket with $\alpha = 0.2$ differs from that for $\alpha = 0.07$ primarily for the $m = -0.4k$ case in which a second peak in the amplitude envelope develops at late times.

4.4.2 Linear to Weakly Nonlinear Dynamics

Figure 4.19 shows the wave-induced mean flow field in a stationary frame for waves with parameters identical to those used in Figure 4.12. The vertical propagation of the wavepackets at the initial group velocity is clearly visible at early times, during which the relative amplitude of the waves does not change. Unlike Figure 4.12, this figure's time-axis extends to $t = 375N^{-1}$, allowing the waves to propagate sufficiently high for exponential amplitude growth to result in weakly nonlinear developments. We observe the transition from linear dynamics to modulational stability or instability beginning at $t \approx 225N^{-1}$. This confirms that the Schrödinger equation for non-Boussinesq waves is able to capture both weakly nonlinear evolution and the transition of a wavepacket from the linear to the nonlinear regime.

The agreement between the results of the fully nonlinear simulations and the solutions of the weakly nonlinear Schrödinger equation demonstrates the importance of the wave-induced mean flow to wavepacket evolution. This analysis clearly indicates that interactions between the waves and the wave-induced mean flow are the principle mechanism for the development of the weakly nonlinear effects that determine the dynamics of the wavepacket at late times, including its modulational stability or instability. In fact, the weakly nonlinear equation is a reasonable approximation to the fully nonlinear simulation for a wide range of amplitudes and density scale heights, even at very late times, capturing many of the qualitative, if not the quantitative, dynamics of the waves.

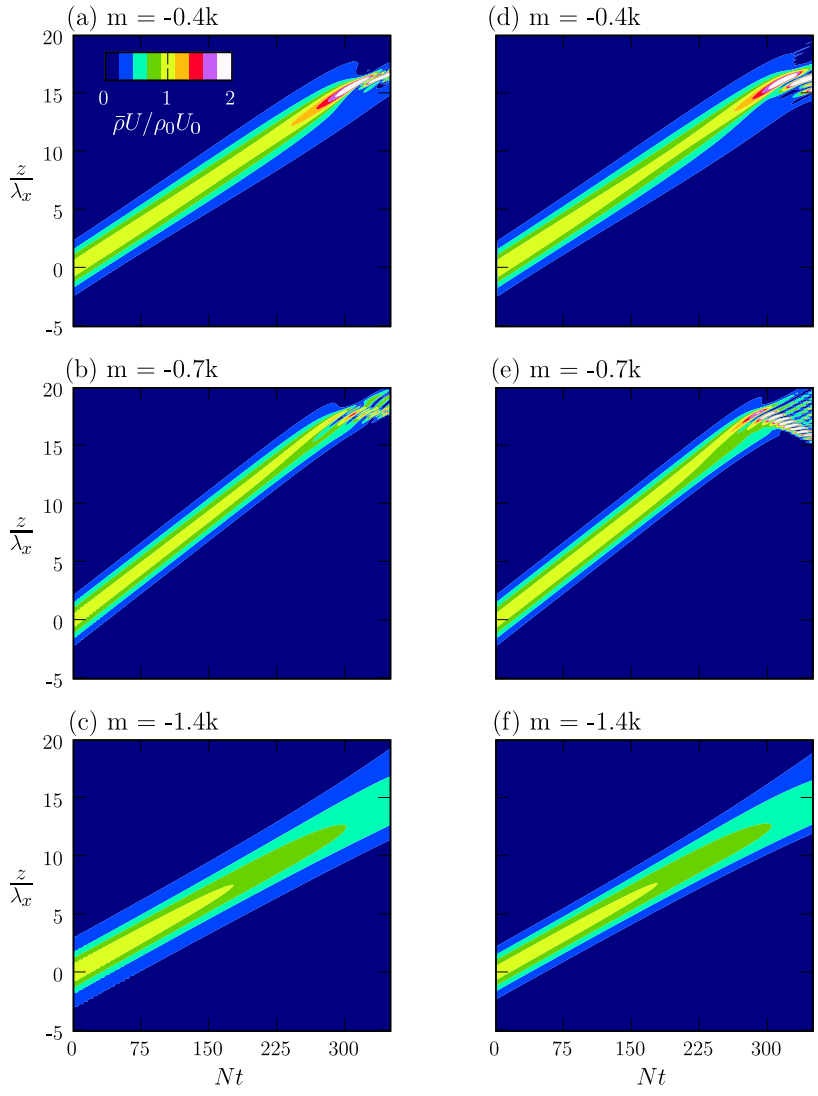

Figure 4.19: Time series of the normalized wave-induced mean flow field, from fully and weakly nonlinear simulations with $\alpha = 0.03$, $H_\rho = 3.2\lambda_x$ and $m = -0.4k$, $m = -0.7k$, or $m = -1.4k$. The plots show the wave-induced mean flow multiplied by the background density profile: $\bar{\rho}(z)U(z,t)/\rho_0 U_0$, where z is the stationary vertical co-ordinate.

4.5 Breaking Heights

In order to gain further insight into the influence of nonlinear effects on wave evolution at late times, fully nonlinear numerical simulations were performed in which the wavepackets were allowed to propagate vertically towards the overturning level predicted by linear theory. The conditions used to calculate the height of wave overturning in the fully nonlinear simulations, as well as the determination of the predicted overturning heights from linear theory, are detailed in Appendix C.

4.5.1 Wave Breaking: Anelastic Gas

Figure 4.20 presents the breaking heights calculated using linear theory, z_{B0}, compared with those determined from the fully nonlinear numerics, z_B. The value of H_θ is varied, while H_ρ is kept fixed at $15.9\lambda_x$. For wavepackets which are non-hydrostatic, with $m = -0.4k$, the breaking level is always significantly over-predicted by linear theory. In fact, for the highest values of λ_x/H_θ the breaking height from linear theory is over 5 times higher than the actual breaking level. These waves are most likely overturning so much lower than predicted due to the rapid amplitude increase associated with modulational instability. Waves of vertical wavenumber $m = -0.7k$ also break consistently lower than the predictions of linear theory.

More hydrostatic waves, which might be expected to propagate above the predicted levels from linear theory due to the relative amplitude decrease associated with modulational stability, are found to break consistently below the location given by linear theory. The closest agreement with linear theory is found at $\lambda_x/H_\theta = 0.001$, in other words for the most weakly stratified fluid. Investigation of a wider range of H_θ values was not undertaken since smaller values result in breaking immediately upon initialization.

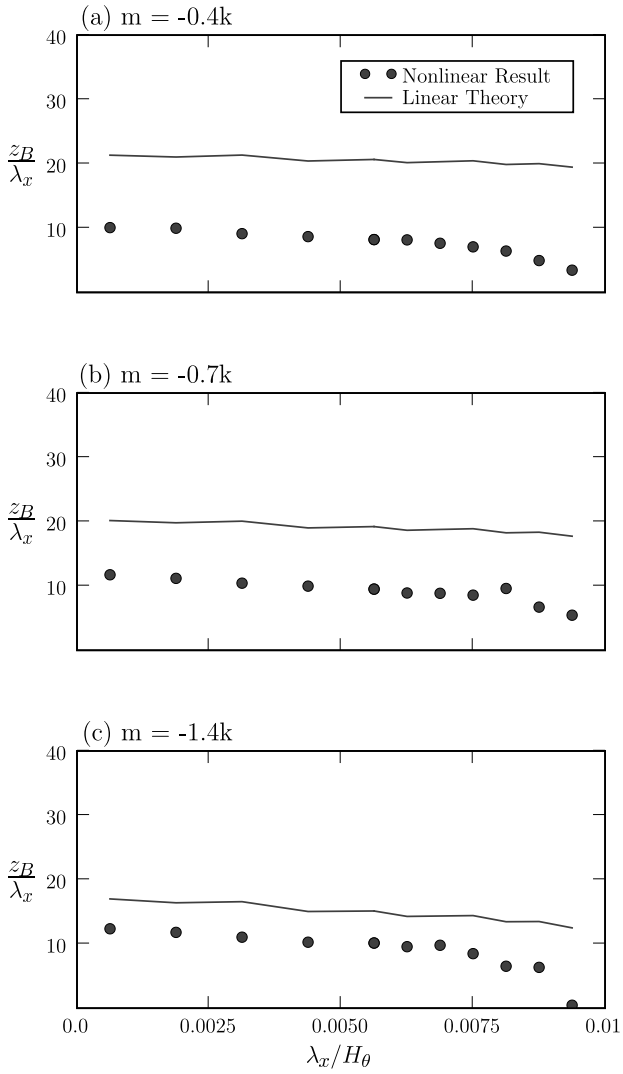

Figure 4.20: Results from anelastic fully nonlinear numerical simulations for the normalized breaking height z_B/λ_x of a wavepacket with $\beta = 0.015$, plotted against the horizontal wavelength normalized by the potential temperature scale height λ_x/H_θ. The vertical wavenumbers shown are $m = -0.4k$, $m = -0.7k$, and $m = -1.4k$. The solid lines are theoretical predictions from linear theory.

As expected, overturning occurs at lower levels for smaller values of H_θ, corresponding to a more rapid exponential increase in amplitude. For all three vertical wavenumbers, linear theory does a better job of predicting the breaking levels for less anelastic fluids with weaker temperature stratification. This is problematic for the prediction of internal gravity wave breaking in the atmosphere, which has a typical value of $\lambda_x/H_\theta = 0.006$ for the parameters considered in this analysis.

Figure 4.21 presents the breaking heights calculated using linear theory compared with those determined from the fully nonlinear numerics for varying values of H_ρ. Here H_θ is held constant at $159\lambda_x$. Smaller values of H_ρ were not considered, since both the linear theory and the nonlinear simulations converge to a constant value of z_{B0} and z_B in the limit $H_\rho \to 0$. There is very little variation in the breaking levels determined from the fully nonlinear numerics, confirming that H_ρ does not have a large impact on the breaking height of wavepackets with any of the three vertical wavenumbers considered.

Wavepackets which are non-hydrostatic, with $m = -0.4k$, experience a negligible change in breaking height as H_ρ is increased, and break consistently below the levels predicted using linear theory. Waves of vertical wavenumber $m = -0.7k$ also break lower than predicted by linear theory, with a slight increase in the nonlinear breaking height z_B for larger values of H_ρ. Linear theory predicts that the breaking height will decrease for larger H_ρ, which results in better agreement as the fluid becomes more Boussinesq. More hydrostatic waves, which in Figure 4.20 break consistently below the levels predicted by linear theory, are now seen to break above the predicted breaking height z_{B0} for very large values of H_ρ. In this limit, the nonlinear breaking heights increase slightly, while the predicted overturning levels based on linear theory become significantly lower. Such a situation corresponds to a fluid with either a very small potential temperature scale height or a very large density scale

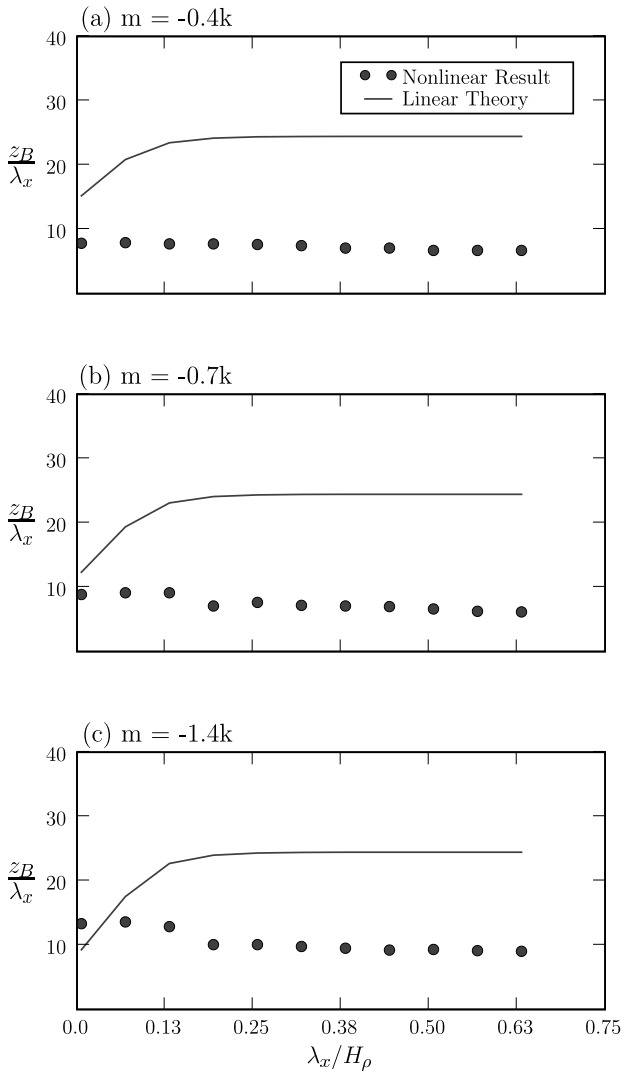

Figure 4.21: Results from anelastic fully nonlinear numerical simulations for the normalized breaking height z_B/λ_x of a wavepacket with $\beta = 0.015$, plotted against the horizontal wavelength normalized by the density scale height λ_x/H_ρ. The vertical wavenumbers shown are $m = -0.4k$, $m = -0.7k$, and $m = -1.4k$. The solid lines are theoretical predictions from linear theory.

height, so that $H_\rho \approx H_\theta$. This is not realistic for atmospheric stratifications.

4.5.2 Wave Breaking: Non-Boussinesq Liquid

Figure 4.22 compares the predicted breaking heights based on linear theory z_{B0} with the breaking heights determined from fully nonlinear numerical simulations z_B for $\alpha = 0.07$ and for a range of λ_x/H_ρ. The extension of these results to waves of other sufficiently small initial amplitudes is given in Appendix D.

For waves of wavenumber $m = -0.4k$, breaking occurs consistently below the levels predicted by linear theory. This is expected based on the rapid amplitude growth caused by modulational instability. Conversely, modulationally stable waves of wavenumber $m = -1.4k$, whose relative amplitude decreases, break well above the predicted levels from linear theory. Waves with vertical wavenumber $m = -0.7k$ break both above and below the heights predicted by linear theory, depending upon λ_x/H_ρ.

If we consider λ_x to be fixed, and allow H_ρ to vary, we see that for the range of density scale heights considered, agreement with linear theory improves for waves in increasingly non-Boussinesq fluids. There is some indication in Figure 4.22b that this trend may reverse as H_ρ becomes increasingly small. We were unable to confirm this using the numerical model, however, as the wavepackets became unstable and began to overturn almost immediately upon initialization. It is also clear from Figure 4.22 that waves in more Boussinesq fluids are able to propagate further before breaking, which is consistent with our expectations of decreased amplitude growth for larger density scale heights.

4.6 Anelastic/Non-Boussinesq Comparison

A direct comparison of internal gravity waves in an anelastic gas and a non-Boussinesq liquid is not really possible in the sense that the weakly and fully nonlinear anelastic gas equations do not collapse to the non-Boussinesq equa-

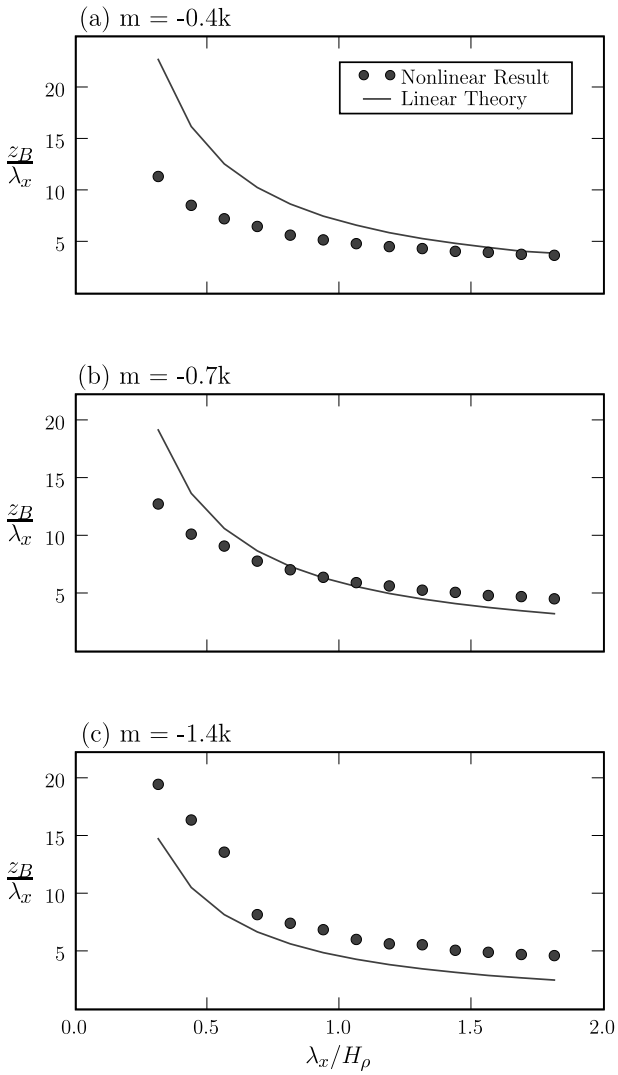

Figure 4.22: Results from non-Boussinesq fully nonlinear numerical simulations for the normalized breaking height z_B/λ_x of a wavepacket with $\alpha = 0.07$, plotted against the horizontal wavelength normalized by the density scale height λ_x/H_ρ. The vertical wavenumbers shown are $m = -0.4k$, $m = -0.7k$, and $m = -1.4k$. The solid lines are theoretical predictions from linear theory.

tions in the limit $H_\theta \to \infty$. Furthermore, while $\bar{\rho}$ in a uniformly stratified non-Boussinesq liquid is a decreasing exponential, $\bar{\rho} \equiv \rho_0 \exp(-z/H_\rho)$, it is given in terms of $\bar{\theta}$ in an anelastic gas. However, a general comparison can be made, as shown in Figure 4.23. In this figure, we see the non-Boussinesq wavepackets from Figure 4.16 (in the leftmost plots) compared with wavepackets in an anelastic gas for which the potential temperature scale height is so large as to be effectively approaching infinity. For both the non-Boussinesq and anelastic fluid $H_\rho = 3.2\lambda_x$, however the amplitudes of the wavepackets are not the same. Since we deal with a streamfunction in the non-Boussinesq liquid and a mass-streamfunction in the anelastic gas, it is difficult to compare amplitudes at all. In this figure, $\|A_\Psi\|$ is about half the value of $\|A_\psi\|$, chosen to create a similar initial value of the wave-induced mean flow field.

Qualitatively, there is a surprising amount of similarity between the two sets of plots. In both, we see the same characteristics of modulational stability or instability, development of asymmetry and decrease in c_{gz} at late times. The anelastic waves have larger maximum amplitude at late times, and the weakly nonlinear dynamics develop more rapidly. Non-hydrostatic wavepackets exhibit modulational instability and break below the levels predicted by linear theory, while modulational stability is observed for hydrostatic wavepackets. In the non-Boussinesq liquid, these wavepackets were observed to propagate well above the overturning levels predicted by linear theory. In the anelastic gas, however, they developed a distinctive pattern of multiple narrow, large-amplitude peaks at late times, which resulted in wave breaking below the predicted level. This feature is at least partially a result of the interactions between the waves and the wave-induced mean flow, and is captured to some degree by the third order $\partial_z U$ term in the anelastic Schrödinger equation. With the exception of this feature, the weakly nonlinear equation was found to be effective at capturing the wave dynamics in all cases over the

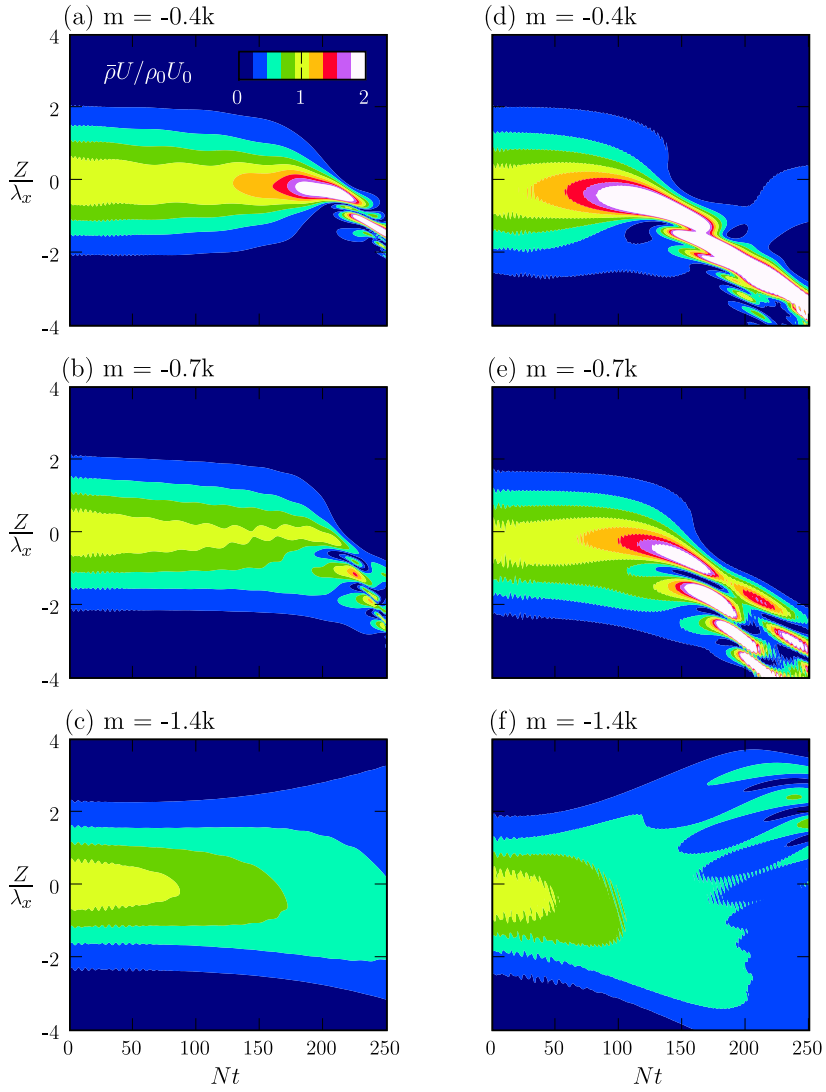

Figure 4.23: Comparison of anelastic and non-Boussinesq fully nonlinear numerical simulations for the $\bar{\rho}U/\rho_0 U_0$ field of a wavepacket, with $\beta = 0.015$, $\alpha = 0.07$, $H_\theta = 1.6 \times 10^7 \lambda_x$ and $H_\rho = 3.2\lambda_x$, for vertical wavenumbers $m = -0.4k$, $m = -0.7k$, and $m = -1.4k$.

course of each wavepacket's evolution. The biggest discrepancy in both the anelastic gas and the non-Boussinesq liquid is the moderate overestimation of the amplitude of the wave-induced mean flow field by the weakly nonlinear equation at very late times.

In terms of breaking height, it was found that the density scale height was the primary parameter, apart from the initial amplitude of the wave, that affected wave breaking in a non-Boussinesq liquid. In an anelastic gas, it was the potential temperature scale height, and not H_ρ, that was the most important parameter. This is a result of defining the background density in terms of $\bar{\theta}$. As seen in Figure 4.20, 4.21 and 4.22, the discrepancies between the heights at which linear theory predicts wave overturning and the locations of wave breaking given by the fully nonlinear simulation are larger for the anelastic gas than for the non-Boussinesq liquid.

We conclude that the study of non-Boussinesq waves in a liquid is a valid means to observe and analyze modulationally stable and unstable wavepackets, as well as the interaction of waves with the wave-induced mean flow. It allows us to determine, through comparison with the corresponding anelastic results, which dynamics are a consequence of the thermodynamics of the atmosphere. However, it cannot provide quantitative results that are applicable to the atmosphere, nor can it capture all the nonlinear dynamics that have an impact upon wave breaking heights.

Laboratory experiments involving a non-Boussinesq liquid are worthwhile, particularly since they are simpler to perform than a corresponding experimental study in an anelastic gas. In particular, if the primary focus is the exponential amplitude growth of a vertically propagating internal gravity wavepacket with height, then a non-Boussinesq liquid is an ideal proxy for an anelastic gas for a range of amplitudes and vertical wavenumbers.

Chapter 5

Discussion and Conclusion

In this thesis, I have determined the form for the wave-induced mean flow of internal gravity waves in a non-Boussinesq liquid, derived the weakly nonlinear Schrödinger equations for the evolution of wavepackets in both an anelastic gas and a non-Boussinesq liquid and described two fully nonlinear numerical simulations that I developed to model these waves. I have compared the results of the fully nonlinear numerical simulations to those from the weakly nonlinear equations for a variety of wavepacket parameters, and determined the impact of weakly nonlinear dynamics on wave breaking height. Finally, I have compared the breaking heights determined from the fully nonlinear simulations with the overturning heights I determined through the use of linear theory.

It has been shown that the dominant characteristics of the evolution of a horizontally periodic, vertically localized wavepacket are well captured in both the linear and nonlinear regimes by a weakly nonlinear Schrödinger equation describing only the interactions of the waves with the wave-induced mean flow. The Schrödinger equation is a reasonably good approximation even as the waves approach breaking amplitudes. This holds true for a wavepacket propagating in an anelastic gas and in a non-Boussinesq liquid. If $H_\rho k \gg 1$, waves of frequency $\omega > (2/3)^{1/2} N$ ($|m/k| < 2^{-1/2}$) are modulationally unstable, experiencing growth and narrowing of the amplitude envelope and

a decrease in vertical group velocity. This is more pronounced in an anelastic gas, for which weakly nonlinear dynamics develop more rapidly prior to wave overturning. In particular, there is a larger decrease in the vertical group velocity and a more rapid increase in the relative amplitude of the envelope. Symmetry breaking is also seen for waves of frequency $\omega \approx (2/3)^{1/2}N$, which propagate at the fastest vertical group velocity and represent the critical point between modulational stability and instability. Modulationally stable waves with $\omega < (2/3)^{1/2}N$ experience rapid broadening and a decreasing relative amplitude. At late times, the broadened amplitude envelope evolves to form a series of distinct peaks that persist and increase sharply in amplitude for modulationally stable waves in an anelastic gas.

In order to capture the observed symmetry breaking and decrease in vertical group velocity, it was necessary to include third order terms in the weakly nonlinear Schrödinger equations. At late times, it was seen that these equations, while still capturing many of the qualitative features of the wavepacket evolution, were unable to accurately predict some of the quantitative features of the waves. In particular, the maximum amplitude of the wave-induced mean flow field was too large when compared to the results of the fully nonlinear numerical simulations. Overall, it was found that the weakly nonlinear dynamics of internal gravity waves in both a non-Boussinesq liquid and an anelastic gas were primarily determined by the interaction of the waves with the wave-induced mean flow, with discrepancies appearing only at late times.

Non-hydrostatic waves in a non-Boussinesq liquid or an anelastic gas consistently break at lower levels than predicted by linear theory. Hydrostatic waves in a non-Boussinesq liquid break at heights greater than those predicted by linear theory, so that for a given density scale height H_ρ, the predicted breaking height will be inaccurate in most circumstances. As an illustration, consider hydrostatic internal waves having a horizontal wavelength on the order of 1km.

Figure 4.22 indicates that such waves will break at least 30% higher than expected from the predictions of linear theory. If the horizontal wavelength is closer to 10km, the wave will break on the order of $1\frac{1}{2}$ times higher than predicted by linear theory.

If hydrostatic waves in an anelastic gas are considered, however, Figure 4.20 indicates that breaking will occur at heights lower than those predicted by linear theory, for a range of potential temperature scale heights H_θ. As an example, consider a wave with horizontal wavelength of about 1km, which breaks roughly 50% lower than the predicted breaking height calculated using linear theory. This occurs in part due to third-order nonlinear dispersion resulting from the interaction of the waves with the wave-induced mean flow.

For realistic atmospheric parameters, with $H_\rho \approx 10$km and $H_\theta \approx 100$km, a hydrostatic wavepacket of wavelength $\lambda_x = 628$m and initial amplitude $A_\xi \approx 13$m launched near the ground might propagate to a height of about 6km (at mid depth in the troposphere) before breaking. A general circulation model using linear theory would predict a breaking height of around 10km, in the lower stratosphere, nearly twice as high. This analysis indicates that general circulation models that use linear theory to parameterize internal gravity wave breaking deposit momentum at inaccurate heights in the atmosphere.

In order to understand fully the implications of this analysis for internal gravity wave breaking in the atmosphere, much work remains to be done. In particular, it would be advantageous to perform fully nonlinear numerical simulations in which a changing background shear was included, or in which the stratification was non-uniform. Such studies would be better suited to replicating all the physical features present in the actual atmosphere, and are necessary before suggestions can be made on how to improve the parameterizations schemes used to model internal gravity waves in general circulation models of the atmosphere.

Bibliography

Acheson, D. J. (1976). On over-reflexion. *J. Fluid Mech. 77*, 433–472.

Akylas, T. R. and A. Tabaei (2005). Resonant self-acceleration and instability of non-linear internal gravity wavetrains, in: A. Litvak (Ed.). *Frontiers of Nonlinear Physics, Institute of Applied Physics*, 129–135.

Benjamin, T. B. and J. E. Feir (1967). The disintegration of wavetrains on deep water. *J. Fluid Mech. 27*, 417–430.

Bouruet-Aubertot, P., J. Sommeria, and C. Staquet (1995). Breaking of standing internal gravity waves through two-dimensional instabilities. *J. Fluid Mech. 285*, 265–301.

Bretherton, F. P. (1966). Gravity waves in shear. *Quart. J. Roy. Meteorol. Soc. 92*, 466–480.

Bretherton, F. P. (1969). On the mean motion induced by internal gravity waves. *J. Fluid Mech. 36*, 785–803.

Clark, H. A. and B. R. Sutherland (2009). Schlieren measurements of internal waves in non-boussinesq fluids. *Expts. in Fluids 47*, 183–193.

Conte, S. D. and C. deBoor (1972). *Elementary Numerical Analysis*. McGraw-Hill, New York.

Dunkerton, T. J. (1981). Wave transience in a compressible atmosphere. Part i: Transient internal wave, mean-flow interaction. *J. Atmos. Sci. 38*, 281–297.

Eliassen, A. and E. Palm (1961). On the transfer of energy in stationary mountain waves. *Geofys. Publ. 22*, 1–23.

Fermi, E., J. Pasta, and S. Ulam (1974). Studies of nonlinear problems I, Los Alamos Report LA 1940, 1955, in:. *A. C. Newell (Ed.), (reproduced) Nonlinear Wave Motion, Amer. Math. Soc., Providence, RI*.

Fritts, D. C. (1978). The nonlinear gravity wave - critical level interaction. *J. Atmos. Sci. 35*, 397–413.

Fritts, D. C. and T. J. Dunkerton (1984). A quasi-linear study of gravity-wave saturation and self-acceleration. *J. Atmos. Sci. 41*, 3272–3289.

Gill, A. E. (1982). *Atmosphere-Ocean Dynamics*. Academic Press, San Diego.

Grimshaw, R. H. J. (1975). Nonlinear internal gravity waves and their interaction with the mean wind. *J. Atmos. Sci. 32*, 1779–1793.

Hamilton, K. (1996). Comprehensive meteorological modelling of the middle atmosphere: a tutorial review. *J. Atmos. Terr. Phys. 58*, 1591–1627.

Hartmann, D. L. (2007). The atmospheric general circulation and its variability. *J. Meteorol. Soc. Japan 85B*, 123–143.

Klein, R. (2008). Asymptotics, structure, and integration of sound-proof atmospheric flow equations. *Theo. Comp. Fluid Dyn. 23*, 161–195.

Klostermeyer, J. (1991). Two- and three-dimensional parametric instabilities in finite amplitude internal gravity waves. *Geophys. Astrophys. Fluid Dyn, 64*, 1–25.

Kundu, P. K. (1990). *Fluid Mechanics*. Academic Press, San Diego.

Lake, B. M., H. C. Yuen, H. Rundgaldier, and W. E. Ferguson (1977). Nonlinear deep-water waves: Theory and experiment, Part 2, Evolution of a continuous wave train. *J. Fluid Mech. 83*, 49–74.

Lindzen, R. S. (1981). Turbulence and stress owing to gravity wave and tidal breakdown. *J. Geophys. Res. 85*, 9707–9714.

Lombard, P. N. and J. J. Riley (1996). On the breakdown into turbulence of propagating internal waves. *Dyn. Atmos. Oceans 23*, 345–355.

McIntyre, M. E. (1981). On the 'wave momentum' myth. *J. Fluid Mech. 106*, 331–347.

McLandress, C. (1998). On the importance of gravity waves in the middle atmosphere and their parameterizations in general circulation models. *J. Atmos. Solar-Terres. Phys. 60*(14), 1357–1383.

Nault, J. T. and B. R. Sutherland (2008). Beyond ray tracing for internal waves. I. small amplitude anelastic waves. *Phys. Fluids 20*.

Phillips, O. M. (1981). Wave interactions - the evolution of an idea. *J. Fluid Mech. 106*, 215–227.

Scinocca, J. F. and T. G. Shepherd (1992). Nonlinear wave-activity conservation laws and hamiltonian structure for the two-dimensional anelastic equations. *J. Atmos. Sci. 49*, 5–27.

Sutherland, B. R. (1996). Internal gravity wave radiation into weakly stratified fluid. *Phys. Fluids 8*, 430–441.

Sutherland, B. R. (2001). Finite-amplitude internal wavepacket dispersion and breaking. *J. Fluid Mech. 429*, 343–380.

Sutherland, B. R. (2006a). Internal wave instability: Wave-wave vs wave-induced mean flow interactions. *Phys. Fluids 18*, Art. No. 074107, doi:10.1063/1.2219102.

Sutherland, B. R. (2006b). Weakly nonlinear internal gravity wavepackets. *J. Fluid Mech. 569*, 249–258.

Vallis, G. K. (2006). *Atmospheric and Oceanic Fluid Dynamics*. Cambridge University Press.

Whitham, G. B. (1974). *Linear and Nonlinear Waves*. John Wiley and Sons, Inc., New York.

Appendix A

Wave-Induced Mean Flow

The following derivation uses Stokes' Theorem in a 2D vertical plane (also known as Green's Theorem) to arrive at the form for the wave-induced mean flow of internal gravity waves in an anelastic gas derived by Scinocca and Shepherd (1992) and given by equation (1.1). Consider

$$\iint_S (\nabla \times \vec{F}) \cdot \hat{n}\, dS = \oint_C \vec{F} \cdot d\vec{r}$$

in which S is an open surface and C is a closed curve around the surface. If we consider the velocity vector in two-dimensions, this becomes:

$$\iint_S (\nabla \times \vec{u}) \cdot \hat{y}\, dS = \oint_C \vec{u} \cdot d\vec{r} \tag{A.1}$$

in which the S is the area between upwardly displaced fluid and the original position of the fluid for the first half-period of wave oscillation, and C is a counter-clockwise curve around this area. Provided that the vertical displacement of the wave ξ is small enough that the vorticity does not vary over S, $\zeta \neq \zeta(z)$, equation (A.1) becomes

$$\begin{aligned} -\int \zeta \int_S dA &= \oint_C \vec{u} \cdot d\vec{r} \\ \Rightarrow -\int_0^{\lambda_x/2} \zeta(\xi) dx &= \frac{1}{2}\lambda_x \langle u \rangle \\ \Rightarrow -\langle \zeta \xi \rangle &\simeq U \end{aligned}$$

in which U is the wave-induced mean flow.

Appendix B

Fully Nonlinear Anelastic Model: Determination of Ψ

During the operation of the fully nonlinear anelastic model, a tri-diagonal matrix inversion is used to calculate the mass-streamfunction from the vorticity (2.16). Represented in terms of its horizontal spectral components, the horizontal discrete Fourier transform of the vorticity equation gives

$$\zeta_n(z,t) = \frac{1}{\bar{\rho}} e^{ik_n x} \left[k_n^2 - \partial_{zz} - \frac{1}{H_\rho}\partial_z \right] A_{\Psi n},$$

in which $k_n = nk$ is the horizontal wavenumber in question for which Ψ_n is being determined.

Using centered finite differences to approximate the vertical derivatives, we have:

$$\begin{aligned} \zeta_{nm}(t) &= \frac{n^2}{\bar{\rho}_m} A_{\Psi nm} - \frac{1}{\bar{\rho}_m} \left[\frac{A_{\Psi n(m+1)} - 2A_{\Psi nm} + A_{\Psi n(m-1)}}{(\Delta z)^2} \right] \\ &\quad - \frac{1}{\bar{\rho}_m H_{\rho m}} \left[\frac{A_{\Psi n(m+1)} - A_{\Psi n(m-1)}}{2\Delta z} \right]. \end{aligned} \tag{B.1}$$

This represents the vorticity amplitude with horizontal wavenumber k_n situated at $z = z_{min} + m\Delta z$. This can be expressed as $\zeta_{nm} = -\frac{1}{(\Delta z)^2}\mathbf{M}\Psi_{nm}$, where $\mathbf{M}$ is the coefficient matrix

$$\begin{bmatrix} 1 & 0 & 0 & 0 & \cdots & & \\ a_1 & b_1 & c_1 & 0 & \cdots & & \\ 0 & a_2 & b_2 & c_2 & \cdots & & \\ \vdots & \vdots & \vdots & \vdots & \ddots & & \\ & & & \cdots & a_{mm} & b_{mm} & c_{mm} \\ & & & \cdots & 0 & 0 & 1 \end{bmatrix}$$

and

$$\begin{aligned} a_m &= \frac{1}{\bar{\rho}_m} - \frac{\Delta z}{2\bar{\rho}_m H_{\rho m}}, \\ b_m &= -\frac{2}{\bar{\rho}_m} - \frac{(n\Delta z)^2}{\bar{\rho}_m}, \\ c_m &= \frac{1}{\bar{\rho}_m} + \frac{\Delta z}{2\bar{\rho}_m H_{\rho m}}. \end{aligned}$$

The code inverts this tridiagonal matrix using the Thomas algorithm (Conte and deBoor, 1972). The inversion proceeds as follows; in the forward elimination phase, we loop over the m index from 1 until mm, modifying the coefficients of the matrix and the ζ array to:

$$\begin{aligned} p &= \frac{a_m}{b_{m-1}}, \\ b_m &= b_m - pc_{m-1}, \\ \zeta_m &= \zeta_m - p\zeta_{m-1}. \end{aligned}$$

In the backward substitution phase, we loop over m from $m-1$ to 1, to determine our new values for the mass-streamfunction:

$$\begin{aligned} \Psi_{mm} &= \frac{\zeta_{mm}}{b_{mm}}, \\ \Psi_m &= \frac{\zeta_m - c_m \Psi_{m+1}}{b_m}. \end{aligned}$$

We get our final values for the mass-streamfunction by multiplying by $-(\Delta z)^2$. Lastly, the values of Ψ at the top and bottom of the domain are forced to zero, to reflect our choice of boundary condition.

The numerical simulation has free-slip boundary conditions in the vertical, which require no normal flow ($w = 0$) at the upper and lower boundaries. In terms of Ψ

$$\left.\frac{1}{\bar{\rho}}\frac{\partial \Psi}{\partial x}\right|_{z=z_{min},z_{max}} = 0.$$

Free-slip boundary conditions essentially ensure that there is no 'friction' between the fluid and the domain boundary. In order to ensure further that the boundaries have no effect on the wave dynamics, the domain size is chosen to be large enough that the wavepacket remains far from the boundaries over the duration of the entire simulation.

There is one subtle issue in the calculation of Ψ near the boundaries. If we simply force the mass-streamfunction to be zero at the top and bottom boundary, we will have a sharp jump from zero to whatever the value of Ψ is just off these boundaries. This will create problems when taking numerical derivatives, and must be corrected for. In order to do this, we first determine the formula for Ψ in terms of ζ near the boundaries. We assume that the wavepacket is not present in this region, so that $u_T = \bar{U}$ and $w_T = 0$. Then $\zeta_T = \partial_z \bar{U}$, and we add some small factor δ to account for any numerical noise: $\zeta_T = \partial_z \bar{U} + \delta$. The equation we want to solve for Ψ is thus

$$\frac{\partial^2 \Psi}{\partial z^2} - \frac{1}{\bar{\rho}}\frac{d\bar{\rho}}{dz}\frac{\partial \Psi}{\partial z} = -\bar{\rho}\frac{\partial \bar{U}}{\partial z} - \bar{\rho}\delta. \tag{B.2}$$

If we make the substitution $f = \partial_z \Psi$, we arrive at a simpler equation, which can be solved easily. The solution for the mass-streamfunction near the boundaries is

$$\Psi = -\int_{z_{min}}^{z_{max}} \bar{\rho}\bar{U}dz \; - \delta \int_{z_{min}}^{z_{max}} \bar{\rho}z dz \; + c_0 \int_{z_{min}}^{z_{max}} \bar{\rho} dz \; + c_1, \tag{B.3}$$

where c_0 and c_1 are unknown constants. The constant c_1 can be ignored, but we need to determine c_0 and δ. These constants must be zero if we want u_T

to be zero at the boundaries, so we need to subtract the corresponding terms from the mass-streamfunction at all heights in the domain. This will result in a smooth transition from Ψ in the interior to the zero value at the boundary.

As it turns out, c_0 and δ can be expressed in terms of derivatives of the mass-streamfunction as

$$\begin{aligned} c_0 &= \frac{1}{\bar{\rho}}\frac{\partial \Psi_{mm}}{\partial z} + \bar{U} + \delta z, \\ \delta &= -\frac{1}{\bar{\rho}}\frac{\partial^2 \Psi_{mm}}{\partial z^2} + \frac{1}{\bar{\rho}^2}\frac{d\bar{\rho}}{dz}\frac{\partial \Psi}{\partial z} - \frac{\partial \bar{U}}{\partial z}. \end{aligned}$$

The derivatives of Ψ are numerically evaluated near the upper boundary:

$$\begin{aligned} \frac{\partial \Psi_{mm}}{\partial z} &= \frac{1}{2\Delta z}\left(3\Psi_{mm} - 4\Psi_{mm-1} + \Psi_{mm-2}\right), \\ \frac{\partial^2 \Psi_{mm}}{\partial z^2} &= \frac{1}{(\Delta z)^2}\left(2\Psi_{mm} - 5\Psi_{mm-1} + 4\Psi_{mm-2} - \Psi_{mm-3}\right). \end{aligned}$$

Finally, the terms $c_0 \int \bar{\rho} dz$ and $-\delta \int \bar{\rho} z dz$ are subtracted from all values of the mass-streamfunction over the height of the domain.

Appendix C

Overturning Criterion and Linear Theory Predictions

The condition for an overturning wave in an anelastic gas is

$$\frac{\partial \theta}{\partial z} + \frac{d\bar{\theta}}{dz} < 0. \tag{C.1}$$

In the fully nonlinear numerical simulation, the left-hand side of this equation is calculated at each timestep, and the lowest height in the vertical at which wave overturning occurs is denoted by z_B for the breaking height of the wavepacket. The corresponding overturning level predicted through the use of linear theory is denoted by z_{B0}. It is assumed that wave breaking occurs at the overturning level.

For an internal gravity plane wave in an anelastic gas, the overturning height from linear theory is implicitly defined through

$$2\frac{k}{\omega}\frac{1}{\bar{\rho}}A_{\Psi_0}\exp(-z/2H_\rho)\max\left[m\ \sin\phi + \left(\frac{1}{H_\rho} - \frac{1}{H_\theta}\right)\cos\phi\right] > 1, \tag{C.2}$$

where $\bar{\rho}$ is given by (2.12), $\phi = kx + mz - \omega t$, and A_{Ψ_0} is the initial maximum amplitude of the mass-streamfunction field. It is not possible to solve this equation explicitly for z_{B0}, but it can be calculated numerically for each vertical wavenumber and value of H_θ and H_ρ. It is acceptable to assess the breaking height of wavepackets using the overturning condition for plane waves because

the width of the wavepackets considered was large enough that any correction to this formula would be negligible. Test cases (not shown) in which the width of the wavepackets was doubled demonstrated slightly increased breaking heights to those presented herein. However, the overall trends in relation to linear theory were not significantly affected.

The condition for wave overturning in a non-Boussinesq liquid is given by

$$\frac{\partial \rho}{\partial z} + \frac{d\bar{\rho}}{dz} > 0. \tag{C.3}$$

The left-hand side of this expression was calculated at each vertical level in the domain at each timestep. The lowest vertical level at which overturning occurred was denoted as the breaking height z_B. This height can be compared with the breaking height z_{B0} predicted by linear theory.

For an internal gravity plane wave in an exponentially decreasing non-Boussinesq background stratification this condition is given in terms of the initial maximum vertical displacement amplitude of the wave A_{ξ_0} by:

$$-A_{\xi_0} \exp\left[z/2H_\rho\right] \max\left[m\ \sin\phi + \frac{1}{2H_\rho}\cos\phi\right] > 1. \tag{C.4}$$

The predicted linear theory breaking height, z_{B0}, can be calculated from this expression for a given density scale height, H_ρ, and vertical wavenumber, m.

Appendix D

Breaking Heights & Amplitude

The non-Boussinesq liquid results presented in Figure 4.22 are for one particular wavepacket amplitude, $\alpha = 0.07$. It is possible to extend these results to any wavepacket of small initial amplitude, which in practice means α less than ~ 0.2. Assuming that at early times the wavepacket evolves linearly, growing only as a result of the exponential decrease in $\bar{\rho}(z)$, a new breaking height $z_{B^\star}$ can be predicted from the known data for z_B. For a wavepacket of amplitude $\alpha^\star$, the new breaking height is given approximately by

$$z_{B^\star} = z_B - 2H_\rho \ln\left(\frac{\alpha^\star}{\alpha}\right), \tag{D.1}$$

in which z_B is the breaking height determined from a fully nonlinear numerical simulation of a wave with initial amplitude α. For example, for a wavepacket with $\alpha^\star = 0.10$, $m = -1.4k$ and $\lambda_x/H_\rho = 0.3$, equation (D.1) predicts $z_{B^\star} = 17.2\lambda_x$. A nonlinear simulation gives $z_{B^\star} = 16.9\lambda_x$ while linear theory predicts $z_{B0^\star} = 12.5\lambda_x$. Thus, even approximating the breaking height from available nonlinear data represents a significant improvement over linear theory.

It is not possible to arrive at a similar approximation for waves in an anelastic gas, since the amplitude growth is related to the background density profile, (2.12), which is defined in terms of the potential temperature. Thus, an explicit formula for $z_{B^\star}$ cannot be derived, as was the case for the linear breaking height prediction in an anelastic gas, equation (C.2).